

THE SIMONS OBSERVATORY: SCIENCE GOALS AND FORECASTS

THE SIMONS OBSERVATORY COLLABORATION:¹ PETER ADE², JAMES AGUIRRE³, ZEESHAN AHMED^{4,5}, SIMONE AIOLA^{6,7}, AAMIR ALI⁸, DAVID ALONSO^{2,9}, MARCELO A. ALVAREZ^{8,10}, KAM ARNOLD¹¹, PETER ASHTON^{8,12,13}, JASON AUSTERMANN¹⁴, HUMNA AWAN¹⁵, CARLO BACCIGALUPI^{16,17}, TAYLOR BAILDON¹⁸, DARCY BARRON^{8,19}, NICK BATTAGLIA^{20,7}, RICHARD BATTYE²¹, ERIC BAXTER³, ANDREW BAZARKO⁶, JAMES A. BEALL¹⁴, RACHEL BEAN²⁰, DOMINIC BECK²², SHAWN BECKMAN⁸, BENJAMIN BERINGUE²³, FEDERICO BIANCHINI²⁴, STEVEN BOADA¹⁵, DAVID BOETTGER²⁵, J. RICHARD BOND²⁶, JULIAN BORRILL^{10,8}, MICHAEL L. BROWN²¹, SARAH MARIE BRUNO⁶, SEAN BRYAN²⁷, ERMINIA CALABRESE², VICTORIA CALAFUT²⁰, PAOLO CALISSE^{11,25}, JULIEN CARRON²⁸, ANTHONY CHALLINOR^{29,23,30}, GRACE CHESMORE¹⁸, YUJI CHINONE^{8,13}, JENS CHLUBA²¹, HSIAO-MEI SHERRY CHO^{4,5}, STEVE CHOI⁶, GABRIELE COPPI³, NICHOLAS F. COTHARD³¹, KEVIN COUGHLIN¹⁸, DEVIN CRICHTON³², KEVIN D. CROWLEY¹¹, KEVIN T. CROWLEY⁶, ARI CUKIERMAN^{4,33,8}, JOHN M. D'EWART⁵, ROLANDO DÜNNER²⁵, TIJMEN DE HAAN^{12,8}, MARK DEVLIN³, SIMON DICKER³, JOY DIDIER³⁴, MATT DOBBS³⁵, BRADLEY DOBER¹⁴, CODY J. DUELL³⁶, SHANNON DUFF¹⁴, ADRI DUIVENVOORDEN³⁷, JO DUNKLEY^{6,38}, JOHN DUSATKO⁵, JOSQUIN ERRARD²², GIULIO FABBIAN³⁹, STEPHEN FEENEY⁷, SIMONE FERRARO⁴⁰, PEDRO FLUXÀ²⁵, KATHERINE FREESE^{18,37}, JOSEF C. FRISCH⁴, ANDREI FROLOV⁴¹, GEORGE FULLER¹¹, BRITTANY FUZIA⁴², NICHOLAS GALITZKI¹¹, PATRICIA A. GALLARDO³⁶, JOSE TOMAS GALVEZ GHERSI⁴¹, JIANGSONG GAO¹⁴, ERIC GAWISER¹⁵, MARTINA GERBINO³⁷, VERA GLUSCEVIC^{43,6,44}, NEIL GOECKNER-WALD⁸, JOSEPH GOLEC¹⁸, SAM GORDON⁴⁵, MEGAN GRALLA⁴⁶, DANIEL GREEN¹¹, ARPI GRIGORIAN¹⁴, JOHN GROH⁸, CHRIS GROPPI⁴⁵, YILUN GUAN⁴⁷, JON E. GUDMUNDSSON³⁷, DONGWON HAN⁴⁸, PETER HARGRAVE², MASAYA HASEGAWA⁴⁹, MATTHEW HASSELFIELD^{50,51}, MAKOTO HATTORI⁵², VICTOR HAYNES²¹, MASASHI HAZUMI^{49,13}, YIZHOU HE⁵³, ERIN HEALY⁶, SHAWN W. HENDERSON^{4,5}, CARLOS HERVIAS-CAIMAPO²¹, CHARLES A. HILL^{8,12}, J. COLIN HILL^{7,43}, GENE HILTON¹⁴, MATT HILTON³², ADAM D. HINCKS^{54,26}, GARY HINSHAW⁵⁵, RENÉE HLOŽEK^{56,57}, SHIRLEY HO¹², SHUAY-PWU PATTY HO⁶, LOGAN HOWE¹¹, ZHIQI HUANG⁵⁸, JOHANNES HUBMAYR¹⁴, KEVIN HUFFENBERGER⁴², JOHN P. HUGHES¹⁵, ANNA IJJAS⁹, MARGARET IKAPE^{56,57}, KENT IRWIN^{4,33,5}, ANDREW H. JAFFE⁵⁹, BHUVNESH JAIN³, OLIVER JEONG⁸, DAISUKE KANEKO¹³, ETHAN D. KARPEL^{4,33}, NOBUHIKO KATAYAMA¹³, BRIAN KEATING¹¹, SARAH S. KERNASOVSKIY^{4,33}, REIJO KESKITALO^{10,8}, THEODORE KISNER^{10,8}, KENJI KIUCHI⁶⁰, JEFF KLEIN³, KENDA KNOWLES³², BRIAN KOOPMAN³⁶, ARTHUR KOSOWSKY⁴⁷, NICOLETTA KRACHMALNICOFF¹⁶, STEPHEN E. KUENSTNER^{4,33}, CHAO-LIN KUO^{4,33,5}, AKITO KUSAKA^{12,60}, JACOB LASHNER³⁴, ADRIAN LEE^{8,12}, EUNSEONG LEE²¹, DAVID LEON¹¹, JASON S.-Y. LEUNG^{56,57,26}, ANTONY LEWIS²⁸, YAQIONG LI⁶, ZACK LI³⁸, MICHELE LIMON³, ERIC LINDER^{12,8}, CARLOS LOPEZ-CARABALLO²⁵, THIBAUT LOUIS⁶¹, LINDSAY LOWRY¹¹, MARIUS LUNGU⁶, MATHÉW MADHAVACHERIL³⁸, DAISY MAK⁵⁹, FELIPE MALDONADO⁴², HAMDÍ MANI⁴⁵, BEN MATES¹⁴, FREDERICK MATSUDA¹³, LOÏC MAURIN²⁵, PHIL MAUSKOPF⁴⁵, ANDREW MAY²¹, NIALH MCCALLUM²¹, CHRIS MCKENNEY¹⁴, JEFF MCMAHON¹⁸, P. DANIEL MEERBURG^{29,23,30,62,63}, JOEL MEYERS^{26,64}, AMBER MILLER³⁴, MARK MIRMELSTEIN²⁸, KAVILAN MOODLEY³², MORITZ MUNCHMEYER⁶⁵, CHARLES MUNSON¹⁸, SIGURD NAESS⁷, FEDERICO NATI³, MARTIN NAVAROLI¹¹, LAURA NEWBURGH⁶⁶, HO NAM NGUYEN⁴⁸, MICHAEL NIEMACK³⁶, HARUKI NISHINO⁴⁹, JOHN ORLOWSKI-SCHERER³, LYMAN PAGE⁶, BRUCE PARTRIDGE⁶⁷, JULIEN PELOTON^{61,28}, FRANCESCA PERROTTA¹⁶, LUCIO PICCIRILLO²¹, GIAMPAOLO PISANO², DAVIDE POLETTI¹⁶, ROBERTO PUDDU²⁵, GIUSEPPE PUGLISI^{4,33}, CHRIS RAUM⁸, CHRISTIAN L. REICHAARDT²⁴, MATHIEU REMAZEILLES²¹, YOEL REPHAELI⁶⁸, DOMINIK RIECHERS²⁰, FELIPE ROJAS²⁵, ANIRBAN ROY¹⁶, SHARON SADEH⁶⁸, YUKI SAKURAI¹³, MARIA SALATINO²², MAYURI SATHYANARAYANA RAO^{8,12}, EMMANUEL SCHAAN¹², MARCEL SCHMITTFULL⁴³, NEELIMA SEHGAL⁴⁸, JOSEPH SEIBERT¹¹, UROS SELJAK^{8,12}, BLAKE SHERWIN^{29,23}, MEIR SHIMON⁶⁸, CARLOS SIERRA¹⁸, JONATHAN SIEVERS³², PRECIOUS SIKHOSANA³², MAXIMILIANO SILVA-FEATHER¹¹, SARA M. SIMON¹⁸, ADRIAN SINCLAIR⁴⁵, PRAWEEN SIRTANASAK¹¹, KENDRICK SMITH⁶⁵, STEPHEN R. SMITH⁵, DAVID SPERGL^{7,38}, SUZANNE T. STAGGS⁶, GEORGE STEIN^{26,56}, JASON R. STEVENS³⁶, RADEK STOMPOR²², ARITOKI SUZUKI¹², OSAMU TAJIMA⁶⁹, SATORU TAKAKURA¹³, GRANT TEPLY¹¹, DANIEL B. THOMAS²¹, BEN THORNE^{38,9}, ROBERT THORNTON⁷⁰, HY TRAC⁵³, CALVIN TSAI¹¹, CAROLE TUCKER², JOEL ULLOM¹⁴, SUNNY VAGNOZZI³⁷, ALEXANDER VAN ENGELEN²⁶, JEFF VAN LANEN¹⁴, DANIEL D. VAN WINKLE⁵, EVE M. VAVAGIAKIS³⁶, CLARA VERGÈS²², MICHAEL VISSERS¹⁴, KASEY WAGONER⁶, SAMANTHA WALKER¹⁴, JON WARD³, BEN WESTBROOK⁸, NATHAN WHITEHORN⁷¹, JASON WILLIAMS³⁴, JOEL WILLIAMS²¹, EDWARD J. WOLLACK⁷², ZHILEI XU³, BYEONGHEE YU⁸, CYNTHIA YU^{4,33}, FERNANDO ZAGO⁴⁷, HEZI ZHANG⁴⁷ AND NINGFENG ZHU³

¹ Correspondence address: so.tac@simonsobservatory.org

² School of Physics and Astronomy, Cardiff University, The Parade, Cardiff, CF24 3AA, UK

³ Department of Physics and Astronomy, University of Pennsylvania, 209 South 33rd Street, Philadelphia, PA, USA 19104

⁴ Kavli Institute for Particle Astrophysics and Cosmology, Menlo Park, CA 94025

⁵ SLAC National Accelerator Laboratory, Menlo Park, CA 94025

⁶ Joseph Henry Laboratories of Physics, Jadwin Hall, Princeton University, Princeton, NJ, USA 08544

⁷ Center for Computational Astrophysics, Flatiron Institute, 162 5th Avenue, New York, NY 10010, USA

⁸ Department of Physics, University of California, Berkeley, CA, USA 94720

⁹ University of Oxford, Denys Wilkinson Building, Keble Road, Oxford OX1 3RH, UK

¹⁰ Computational Cosmology Center, Lawrence Berkeley National Laboratory, Berkeley, CA 94720, USA

¹¹ Department of Physics, University of California San Diego, CA, 92093 USA

¹² Physics Division, Lawrence Berkeley National Laboratory, Berkeley, CA 94720, USA

¹³ Kavli Institute for The Physics and Mathematics of The Universe (WPI), The University of Tokyo, Kashiwa, 277- 8583, Japan

¹⁴ NIST Quantum Sensors Group, 325 Broadway Mailcode 687.08, Boulder, CO, USA 80305

¹⁵ Department of Physics and Astronomy, Rutgers, The State University of New Jersey, Piscataway, NJ USA 08854-8019

¹⁶ International School for Advanced Studies (SISSA), Via Bonomea 265, 34136, Trieste, Italy

¹⁷ INFN, Sezione di Trieste, Padriciano, 99, 34149 Trieste, Italy

¹⁸ Department of Physics, University of Michigan, Ann Arbor, USA 48103

¹⁹ Department of Physics and Astronomy, University of New Mexico, Albuquerque, NM 87131, USA

²⁰ Department of Astronomy, Cornell University, Ithaca, NY, USA 14853

²¹ Jodrell Bank Centre for Astrophysics, School of Physics and Astronomy, University of Manchester, Manchester, UK

- ²² AstroParticule et Cosmologie, Univ Paris Diderot, CNRS/IN2P3, CEA/Irfu, Obs de Paris, Sorbonne Paris Cité, France
- ²³ DAMTP, Centre for Mathematical Sciences, University of Cambridge, Wilberforce Road, Cambridge CB3 0WA, UK
- ²⁴ School of Physics, University of Melbourne, Parkville, VIC 3010, Australia
- ²⁵ Instituto de Astrofísica and Centro de Astro-Ingeniería, Facultad de Física, Pontificia Universidad Católica de Chile, Av. Vicuña Mackenna 4860, 7820436 Macul, Santiago, Chile
- ²⁶ Canadian Institute for Theoretical Astrophysics, University of Toronto, 60 St. George St., Toronto, ON M5S 3H8, Canada
- ²⁷ School of Electrical, Computer, and Energy Engineering, Arizona State University, Tempe, AZ USA
- ²⁸ Department of Physics & Astronomy, University of Sussex, Brighton BN1 9QH, UK
- ²⁹ Kavli Institute for Cosmology Cambridge, Madingley Road, Cambridge CB3 0HA, UK
- ³⁰ Institute of Astronomy, Madingley Road, Cambridge CB3 0HA, UK
- ³¹ Department of Applied and Engineering Physics, Cornell University, Ithaca, NY, USA 14853
- ³² Astrophysics and Cosmology Research Unit, School of Mathematics, Statistics and Computer Science, University of KwaZulu-Natal, Durban 4041, South Africa
- ³³ Department of Physics, Stanford University, Stanford, CA 94305
- ³⁴ University of Southern California. Department of Physics and Astronomy, 825 Bloom Walk ACB 439, Los Angeles, CA 90089-0484
- ³⁵ Physics Department, McGill University, Montreal, QC H3A 0G4, Canada
- ³⁶ Department of Physics, Cornell University, Ithaca, NY, USA 14853
- ³⁷ The Oskar Klein Centre for Cosmoparticle Physics, Department of Physics, Stockholm University, AlbaNova, SE-106 91 Stockholm, Sweden
- ³⁸ Department of Astrophysical Sciences, Peyton Hall, Princeton University, Princeton, NJ, USA 08544
- ³⁹ Institut d'Astrophysique Spatiale, CNRS (UMR 8617), Univ. Paris-Sud, Université Paris-Saclay, Bât. 121, 91405 Orsay, France.
- ⁴⁰ Berkeley Center for Cosmological Physics, University of California, Berkeley, CA 94720, USA
- ⁴¹ Simon Fraser University, 8888 University Dr, Burnaby, BC V5A 1S6, Canada
- ⁴² Department of Physics, Florida State University, Tallahassee FL, USA 32306
- ⁴³ Institute for Advanced Study, 1 Einstein Dr, Princeton, NJ 08540
- ⁴⁴ Department of Physics, University of Florida, Gainesville, Florida 32611, USA
- ⁴⁵ School of Earth and Space Exploration, Arizona State University, Tempe, AZ, USA 85287
- ⁴⁶ University of Arizona, 933 N Cherry Ave, Tucson, AZ 85719
- ⁴⁷ Department of Physics and Astronomy, University of Pittsburgh, Pittsburgh, PA, USA 15260
- ⁴⁸ Physics and Astronomy Department, Stony Brook University, Stony Brook, NY USA 11794
- ⁴⁹ High Energy Accelerator Research Organization (KEK), Tsukuba, Ibaraki 305-0801, Japan
- ⁵⁰ Department of Astronomy and Astrophysics, The Pennsylvania State University, University Park, PA 16802
- ⁵¹ Institute for Gravitation and the Cosmos, The Pennsylvania State University, University Park, PA 16802
- ⁵² Astronomical Institute, Graduate School of Science, Tohoku University, Sendai, 980-8578, Japan
- ⁵³ McWilliams Center for Cosmology, Department of Physics, Carnegie Mellon University, 5000 Forbes Avenue, Pittsburgh, PA 15213, USA
- ⁵⁴ Department of Physics, University of Rome "La Sapienza", Piazzale Aldo Moro 5, I-00185 Rome, Italy
- ⁵⁵ Department of Physics and Astronomy, University of British Columbia, Vancouver, BC, Canada V6T 1Z1
- ⁵⁶ Department of Astronomy and Astrophysics, University of Toronto, 50 St. George St., Toronto, ON M5S 3H4, Canada
- ⁵⁷ Dunlap Institute for Astronomy and Astrophysics, University of Toronto, 50 St. George St., Toronto, ON M5S 3H4, Canada
- ⁵⁸ School of Physics and Astronomy, Sun Yat-Sen University, 135 Xingang Xi Road, Guangzhou, China
- ⁵⁹ Imperial College London, Blackett Laboratory, SW7 2AZ UK
- ⁶⁰ Department of Physics, University of Tokyo, Tokyo 113-0033, Japan
- ⁶¹ Laboratoire de l'Accélérateur Linéaire, Univ. Paris-Sud, CNRS/IN2P3, Université Paris-Saclay, Orsay, France
- ⁶² Van Swinderen Institute for Particle Physics and Gravity, University of Groningen, Nijenborgh 4, 9747 AG Groningen, The Netherlands
- ⁶³ Kapteyn Astronomical Institute, University of Groningen, P.O. Box 800, 9700 AV Groningen, The Netherlands
- ⁶⁴ Dedman College of Humanities and Sciences, Department of Physics, Southern Methodist University, 3215 Daniel Ave. Dallas, Texas 75275-0175
- ⁶⁵ Perimeter Institute 31 Caroline Street North, Waterloo, Ontario, Canada, N2L 2Y5
- ⁶⁶ Department of Physics, Yale University, New Haven, CT 06520, USA
- ⁶⁷ Department of Physics and Astronomy, Haverford College, Haverford, PA, USA 19041
- ⁶⁸ Raymond and Beverly Sackler School of Physics and Astronomy, Tel Aviv University, P.O. Box 39040, Tel Aviv 6997801, Israel
- ⁶⁹ Department of Physics, Faculty of Science, Kyoto University, Kyoto 606, Japan
- ⁷⁰ Department of Physics and Engineering, 720 S. Church St., West Chester, PA 19383
- ⁷¹ Department of Physics and Astronomy, University of California Los Angeles, 475 Portola Plaza, Los Angeles, CA 9009 and
- ⁷² NASA/Goddard Space Flight Center, Greenbelt, MD, USA 20771

ABSTRACT

The Simons Observatory (SO) is a new cosmic microwave background experiment being built on Cerro Toco in Chile, due to begin observations in the early 2020s. We describe the scientific goals of the experiment, motivate the design, and forecast its performance. SO will measure the temperature and polarization anisotropy of the cosmic microwave background in six frequency bands centered at: 27, 39, 93, 145, 225 and 280 GHz. The initial configuration of SO will have three small-aperture 0.5-m telescopes and one large-aperture 6-m telescope, with a total of 60,000 cryogenic bolometers. Our key science goals are to characterize the primordial perturbations, measure the number of relativistic species and the mass of neutrinos, test for deviations from a cosmological constant, improve our understanding of galaxy evolution, and constrain the duration of reionization. The small aperture telescopes will target the largest angular scales observable from Chile, mapping $\approx 10\%$ of the sky to a white noise level of $2 \mu\text{K-arcmin}$ in combined 93 and 145 GHz bands, to measure the primordial tensor-to-scalar ratio, r , at a target level of $\sigma(r) = 0.003$. The large aperture telescope will map $\approx 40\%$ of the sky at arcminute angular resolution to an expected white noise level of $6 \mu\text{K-arcmin}$ in combined 93 and 145 GHz bands, overlapping with the majority of the Large Synoptic Survey Telescope sky region and partially with the Dark Energy Spectroscopic Instrument. With up to an

order of magnitude lower polarization noise than maps from the *Planck* satellite, the high-resolution sky maps will constrain cosmological parameters derived from the damping tail, gravitational lensing of the microwave background, the primordial bispectrum, and the thermal and kinematic Sunyaev–Zel’dovich effects, and will aid in delensing the large-angle polarization signal to measure the tensor-to-scalar ratio. The survey will also provide a legacy catalog of 16,000 galaxy clusters and more than 20,000 extragalactic sources^a.

Contents		
1. Introduction	3	5.5. Impact of foregrounds on lensing 36
2. Forecasting methods	5	6. Primordial bispectrum 37
2.1. Instrument summary	5	7. Sunyaev–Zel’dovich effects 38
2.2. Noise model	5	7.1. Cosmology from tSZ cluster counts 38
2.3. Sky coverage	7	7.1.1. Neutrino mass and dark energy 40
2.4. Foreground model	8	7.1.2. Amplitude of structure: $\sigma_8(z)$ 40
2.4.1. Extragalactic intensity	8	7.2. Neutrino mass from tSZ power spectrum 40
2.4.2. Extragalactic source polarization	9	7.3. Feedback efficiency and non-thermal pressure support 42
2.4.3. Galactic intensity	9	7.4. Growth of structure from kSZ 42
2.4.4. Galactic polarization	9	7.5. Primordial non-Gaussianity from kSZ 43
2.5. Foreground cleaning for the LAT	10	7.6. Epoch of Reionization from kSZ 44
2.5.1. Component separation method	10	8. Extragalactic sources 45
2.5.2. Post-component-separation noise	11	8.1. Active Galactic Nuclei 45
2.5.3. Optimization	11	8.2. Dusty star-forming galaxies 45
2.6. Parameter estimation and external data	11	8.3. Transient sources 46
3. Large-scale B -modes	14	9. Forecast summary and conclusions 46
3.1. Motivation	14	9.1. Key science targets 46
3.2. Measuring B -modes	14	9.2. Legacy catalogs 49
3.3. Forecasting tools	15	9.3. Conclusions 49
3.4. Forecast constraints	16	References 51
3.4.1. Impact of large-area scanning strategy	16	
3.4.2. Fiducial forecasts for r	17	
3.4.3. Departures from the fiducial case	18	
3.5. Limitations of current forecasts	20	
4. Small-scale damping tail	21	
4.1. Forecasts for N_{eff}	21	
4.1.1. Survey requirements	22	
4.1.2. Testing foreground contamination	23	
4.1.3. Impact of point source and atmospheric noise	24	
4.1.4. Beam requirements	25	
4.2. Primordial scalar power	26	
4.3. The Hubble constant	26	
4.4. Additional high- ℓ science	27	
4.4.1. Neutrino mass	27	
4.4.2. Big bang nucleosynthesis	27	
4.4.3. Dark Matter nature and interactions	28	
5. Gravitational lensing	30	
5.1. Delensing efficiency	30	
5.2. Neutrino mass and lensing spectra	31	
5.3. Cross-correlations	32	
5.3.1. Growth of structure: $\sigma_8(z)$	32	
5.3.2. Local primordial non-Gaussianity	33	
5.3.3. Shear bias validation	34	
5.3.4. Lensing ratios: curvature	34	
5.4. Halo lensing: mass calibration	35	

^a A supplement describing author contributions to this paper can be found at <https://simonsobservatory.org/publications.php>

1. INTRODUCTION

Fifteen years have passed between the first release of full-sky microwave maps from the *WMAP* satellite (Bennett et al. 2003), and the final legacy maps from the *Planck* satellite (Planck Collaboration 2018a). During that time, ground-based observations of the cosmic microwave background (CMB) anisotropies have made enormous strides. Maps from these experiments over hundreds of square degrees of the sky currently surpass all balloon and satellite experiments in sensitivity (BICEP2 and Keck Array Collaborations 2016; Louis et al. 2017; Henning et al. 2018; POLARBEAR Collaboration 2014a, 2017), and have set new standards for the mitigation of systematic errors. A rich legacy of scientific discovery has followed.

The rapid progress of ground-based measurements in the last decade has been driven by the development of arrays of superconducting transition-edge sensor (TES) bolometers coupled to multiplexed readout electronics (Henderson et al. 2016; Posada et al. 2016; Suzuki et al. 2016; Hui et al. 2016). The current generation of detector arrays simultaneously measure linear polarization at multiple frequency bands in each focal-plane pixel. Two other innovations have also been essential: optical designs with minimal optical distortions and sizeable focal planes; and sophisticated computational techniques for extracting small sky signals in the presence of far larger atmosphere signals and noise sources.

Ground-based experiments have targeted a range of an-

gular scales. High-resolution experiments such as the Atacama Cosmology Telescope (ACT) and South Pole Telescope (SPT) have arcminute resolution, sufficient to measure not only the power spectrum of primary perturbations, but also secondary perturbations including gravitational lensing and the thermal and kinematic Sunyaev–Zel’dovich (SZ) effects. The low-resolution Background Imaging of Cosmic Extragalactic Polarization experiment and successors (BICEP, BICEP2, Keck Array) have pursued the polarization signal from primordial gravitational waves, which should be most prominent at scales of several degrees. The mid-resolution experiment Simons Array (SA), the successor to POLARBEAR, aims to probe both primordial gravitational waves and gravitational lensing.

Over the past decade, ground-based experimental efforts have made the first-ever detections of the power spectrum of gravitational lensing of the microwave background in both temperature (Das et al. 2011; van Engelen et al. 2012) and polarization (Hanson et al. 2013; POLARBEAR Collaboration 2014b,c; Story et al. 2015; Sherwin et al. 2017), lensing by galaxy clusters (Madhavacheril et al. 2015; Baxter et al. 2015), the kinematic Sunyaev–Zel’dovich effect (Hand et al. 2012), and the thermal Sunyaev–Zel’dovich effect associated with radio galaxies (Gralla et al. 2014). They have compiled catalogs of SZ-selected galaxy clusters (Bleem et al. 2015; Hilton et al. 2018) comparable in size to that extracted from the full-sky maps made by *Planck* (Planck Collaboration 2016m), including many of the most extreme-mass and highest redshift clusters known (e.g., Menanteau et al. 2012), demonstrated quasar feedback from the thermal Sunyaev–Zel’dovich effect (Crichton et al. 2016), and found numerous lensed high-redshift dusty galaxies (Vieira et al. 2010). Cosmological parameter constraints from ground-based primary temperature and polarization power spectra are close, both in central values and uncertainties, to the definitive ones produced by *Planck* (Planck Collaboration 2018d). The *Planck* full-sky maps provide important information at the largest angular scales and in frequency bands which are inaccessible from the ground (Planck Collaboration 2018a).

This scientific legacy is remarkable, but more is yet to come (see, e.g., Abazajian et al. (2016) for a detailed overview). Measurements of gravitational lensing will steadily improve with increasing sensitivity of temperature and polarization maps, coupled with control over systematic effects, leading to improved large-scale structure characterization, dark matter and dark energy constraints, and neutrino mass limits. The thermal and kinematic SZ effects will become more powerful probes of both structure formation and astrophysical processes in galaxies and galaxy clusters. Measurements of the polarization power spectrum to cosmic variance limits down to arcminute angular scales will provide a nearly-independent determination of cosmological parameters (Galli et al. 2014; Calabrese et al. 2017), and hence provide important consistency checks (Addison et al. 2016; Planck Collaboration 2017). The polarization signature of a primordial gravitational wave signal still beckons.

The Simons Observatory (SO) is a project designed to target these goals. We are a collaboration of over 200 scientists from around 40 institutions, constituted in 2016. The collaboration is building a Large Aperture

Telescope (LAT) with a 6-meter primary mirror similar in size to ACT, and three 0.5-meter refracting Small Aperture Telescopes (SATs) similar in size to BICEP3. New optical designs (Niemack 2016; Parshley et al. 2018) will provide much larger focal planes for the LAT than current experiments. We initially plan to deploy a total of 60,000 detectors, approximately evenly split between the LAT and the set of SATs. Each detector pixel will be sensitive to two orthogonal linear polarizations and two frequency bands (Henderson et al. 2016; Posada et al. 2016). This number of detectors represents an order of magnitude increase over the size of current microwave detector arrays, and is more total detectors than have been deployed by all previous microwave background experiments combined.

SO will be located in the Atacama Desert at an altitude of 5,200 meters in Chile’s Parque Astronómico. It will share the same site on Cerro Toco as ACT, Simons Array, and the Cosmology Large Angular Scale Surveyor (CLASS¹), overlooking the Atacama Large Millimeter Array (ALMA²) on the Chajnantor Plateau. The site is also one of those planned for the future CMB-S4 experiment (Abazajian et al. 2016). Nearly two decades of observations from this site inform the project. SO will cover a sky region which overlaps many astronomical surveys at other wavelengths; particularly important will be the Large Synoptic Survey Telescope (LSST³), as well as the Dark Energy Survey (DES⁴), the Dark Energy Spectroscopic Instrument (DESI⁵), and the *Euclid* satellite⁶. A full description of the experiment design will be presented in a companion paper.

This paper presents a baseline model for the SO instrument performance, including detector noise, frequency bands, and angular resolution. We also present a set of simple but realistic assumptions for atmospheric and galactic foreground emission. We translate these assumptions into anticipated properties of temperature and polarization maps, given nominal sky survey coverage and duration of observation. We then summarize the constraints on various cosmological signals that can be obtained from such maps. The results of this process have served as the basis for optimizing experimental design choices, particularly aperture sizes and angular resolutions, division of detectors between large and small aperture telescopes, the range of frequency bands, and the division of detectors between frequency bands.

In Sec. 2 we give specifications for the Simons Observatory instruments, and our baseline assumptions for the atmosphere and for foreground sources of microwave emission. We then describe science goals, design considerations and forecasts for each major science probe: *B*-mode polarization at large angular scales (Sec. 3), the damping tail of the power spectra at small angular scales (Sec. 4), gravitational lensing (Sec. 5), probes of non-Gaussian perturbation statistics, particularly the primordial bispectrum (Sec. 6), the thermal and kinematic SZ effects (Sec. 7), and extragalactic sources (Sec. 8). We

¹ <http://sites.krieger.jhu.edu/class/>

² <http://www.almaobservatory.org/en/home/>

³ <https://www.lsst.org/>

⁴ <https://www.darkenergysurvey.org/>

⁵ <https://www.desi.lbl.gov/>

⁶ <http://sci.esa.int/euclid/>

conclude in Sec. 9 with a summary of the forecasts and a discussion of the practical challenges of these measurements.

All science forecasts in this paper assume the standard Λ CDM cosmological model with parameters given by the temperature best-fit *Planck* values (Planck Collaboration 2016e) and an optical depth to reionization of 0.06 (Planck Collaboration 2016o), as fully specified in Sec. 2.6. However, the standard cosmology is now so well constrained that our analyses are essentially independent of assumed values of the cosmological parameters if they are consistent with current data.

2. FORECASTING METHODS

Here we summarize common assumptions for all science projections, including our instrument model (Sec. 2.1), atmospheric noise model (Sec. 2.2), sky coverage (Sec. 2.3), foreground emission model (Sec. 2.4), foreground cleaning for the Large Aperture Telescope (Sec. 2.5), choice of cosmological parameters, and assumptions about external datasets (Sec. 2.6). Details specific to the analysis of individual statistics are described in Secs. 3–8. In particular, the substantially different approach taken for large-scale B -modes is described in Sec. 3.

2.1. Instrument summary

SO will consist of one 6-m Large Aperture Telescope (LAT) and three 0.5-m Small Aperture Telescopes (SATs). Early in the SO design process we concluded that both large and small telescopes were needed, consistent with Abazajian et al. (2016), to optimally measure the CMB anisotropy from few-degree scales down to arcminute scales. The large telescope provides high angular resolution; the small telescopes have a larger field of view and are better able to control atmospheric contamination in order to measure larger angular scales.

The LAT receiver will have 30,000 TES bolometric detectors distributed among seven optics tubes that span six frequency bands from 27 to 280 GHz. Each LAT tube will contain three arrays, each on a 150 mm detector wafer, each measuring two frequency bands and in two linear polarizations. One ‘low-frequency’ (LF) tube will make measurements in two bands centered at 27 and 39 GHz, four ‘mid-frequency’ (MF) tubes will have bands centered at 93 and 145 GHz, and two ‘high-frequency’ (HF) tubes will have bands at 225 and 280 GHz. These seven tubes will fill half of the LAT receiver’s focal plane. The LAT will attain arcminute angular resolution, as shown in Table 1. The field of view of each LAT optics tube will be approximately 1.3° in diameter, and the total field of view will be approximately 7.8° in diameter.

The three SATs, each with a single optics tube, will together also contain 30,000 detectors. The SAT optics tubes will each house seven arrays, and will each have a continuously rotating half-wave plate to modulate the large-scale atmospheric signal. Two SATs will observe at 93 and 145 GHz (MF) and one will measure at 225 and 280 GHz (HF); an additional low-frequency optics tube at 27 and 39 GHz will be deployed in one of the MF SATs for a single year of observations. The SATs will have 0.5° angular resolution at 93 GHz. Further details can be found in the companion instrument paper (Simons Observatory Collaboration in prep.).

2.2. Noise model

We consider two cases for the SO performance: a nominal ‘baseline’ level which requires only a modest amount of technical development over currently deployed experiments, and a more aggressive ‘goal’ level. We assume a 5-year survey with 20% of the total observing time used for science analysis, consistent with the realized performance after accounting for data quality cuts of both the POLARBEAR and ACT experiments. For the LAT, we additionally increase the noise levels to mimic the effects of discarding 15% of the maps at the edges, where the noise properties are expected to be non-uniform. This is consistent with the sky cuts applied in, e.g., Louis et al. (2017). The expected white noise levels are shown in Table 1. These are computed from the estimated detector array noise-equivalent temperatures (NETs), which include the impact of imperfect detector yield, for the given survey areas and effective observing time. The detector NETs and details of this calculation are in the companion paper (Simons Observatory Collaboration in prep.).

These noise levels are expected to be appropriate for small angular scales, but large angular scales are contaminated by $1/f$ noise at low frequencies in the detector time stream, which arises primarily from the atmosphere and electronic noise. We model the overall expected SO noise spectrum in each telescope and band to have the form

$$N_\ell = N_{\text{red}} \left(\frac{\ell}{\ell_{\text{knee}}} \right)^{\alpha_{\text{knee}}} + N_{\text{white}}, \quad (1)$$

where N_{white} is the white noise component and N_{red} , ℓ_{knee} , and α_{knee} describe the contribution from $1/f$ noise. We adopt values for these parameters using data from previous and on-going ground-based CMB experiments. We do not model the $1/f$ noise for the SATs in temperature: we do not anticipate using the SAT temperature measurements for scientific analysis, as the CMB signal is already well measured by *WMAP* and *Planck* on these scales.

SAT polarization: In this case we normalize the model such that $N_{\text{red}} = N_{\text{white}}$. At a reference frequency of 93 GHz, we find that a noise model with $\ell_{\text{knee}} \approx 50$ and α_{knee} in the range of -3.0 to -2.4 describes the uncertainty on the B -mode power spectrum, C_ℓ^{BB} , achieved by QUIET (QUIET Collaboration 2011, 2012), BICEP2 and Keck Array (BICEP2 and Keck Array Collaborations 2016), and ABS (Kusaka et al. 2018) as shown in Fig. 1. QUIET and ABS were both near the SO site in Chile, and used fast polarization modulation techniques, while BICEP2 and Keck Array are at the South Pole. This ℓ_{knee} accounts for both the $1/f$ noise and the loss of modes due to filtering, and is also consistent with data taken by POLARBEAR in Chile with a continuously rotating half-wave plate (Takakura et al. 2017). We adopt $\ell_{\text{knee}} = 50$ for a pessimistic case and $\ell_{\text{knee}} = 25$ for an optimistic case. Here we assume a scan speed twice as fast as that adopted by ABS and QUIET. We scale the $1/f$ noise to each of the SO bands by evaluating the deviation of the brightness temperature due to expected changes in Precipitable Water Vapor (PWV) level using the AM model (Paine 2018) and the Atmospheric Transmission at Microwaves

Table 1
Properties of the planned SO surveys^a.

Freq. [GHz]	SATs ($f_{\text{sky}} = 0.1$)			LAT ($f_{\text{sky}} = 0.4$)		
	FWHM (')	Noise (baseline) [$\mu\text{K-arcmin}$]	Noise (goal) [$\mu\text{K-arcmin}$]	FWHM (')	Noise (baseline) [$\mu\text{K-arcmin}$]	Noise (goal) [$\mu\text{K-arcmin}$]
27	91	35	25	7.4	71	52
39	63	21	17	5.1	36	27
93	30	2.6	1.9	2.2	8.0	5.8
145	17	3.3	2.1	1.4	10	6.3
225	11	6.3	4.2	1.0	22	15
280	9	16	10	0.9	54	37

^a The detector passbands are being optimized (see [Simons Observatory Collaboration in prep.](#)) and are subject to variations in fabrication. For these reasons we expect the SO band centers to differ slightly from the frequencies presented here. ‘Noise’ columns give anticipated white noise levels for temperature, with polarization noise $\sqrt{2}$ higher as both Q and U Stokes parameters are measured. Noise levels are quoted as appropriate for a homogeneous hits map.

Table 2

Band-dependent parameters for the large-angular-scale noise model described in Eq. 1. Parameters that do not vary with frequency are in the text.

Freq. [GHz]	SAT Polarization			LAT Temperature
	$\ell_{\text{knee}}^{\text{a}}$	$\ell_{\text{knee}}^{\text{b}}$	α_{knee}	$N_{\text{red}} [\mu\text{K}^2\text{s}]$
27	30	15	-2.4	100
39	30	15	-2.4	39
93	50	25	-2.5	230
145	50	25	-3.0	1,500
225	70	35	-3.0	17,000
280	100	40	-3.0	31,000

^a Pessimistic case. ^b Optimistic case.

(ATM) code ([Pardo et al. 2001](#)). The parameters we adopt for each band are given in Table 2. In forecasting parameters derived from the SATs, we consider these pessimistic and optimistic $1/f$ cases in combination with the SO baseline and goal white noise levels.

LAT polarization: Again we fix $N_{\text{red}} = N_{\text{white}}$. We find that $\ell_{\text{knee}} = 700$ and $\alpha_{\text{knee}} = -1.4$ approximates the ℓ -dependence of the uncertainties on the polarization power spectrum achieved by ACTPol ([Louis et al. 2017](#)) in Chile at 150 GHz, and is consistent with data from POLARBEAR without a continuously rotating half-wave plate ([POLARBEAR Collaboration 2014a, 2017](#)). We use these parameters at all frequencies, although in practice we expect the emission to be frequency-dependent. Upcoming data from ACTPol and POLARBEAR will inform a future refinement to this model.

LAT temperature: The intensity noise is primarily due to brightness variation in the atmosphere. We model the intensity noise by first measuring the contamination in time-ordered-data (TODs) and sky maps from ACTPol’s 90 and 145 GHz bands, assuming that the SO detector passbands will be similar to those of ACTPol. We then extrapolate this result to the full set of LAT bands, and account for the LAT’s large field of view.

To characterize the intensity noise, we fix $\ell_{\text{knee}} = 1000$. Using data from ACTPol ([Louis et al. 2017](#)), we estimate a noise parameter $N_{\text{red}} = 1800 \mu\text{K}^2\text{s}$ at 90 GHz and $N_{\text{red}} = 12000 \mu\text{K}^2\text{s}$ at 145 GHz, with $\alpha_{\text{knee}} = -3.5$ in both cases. The dominant contribution to atmospheric contamination at 90 and 145 GHz is due to PWV. We use the 145 GHz noise power measured by ACTPol to fix the overall scaling of the contamination. To extrapolate to

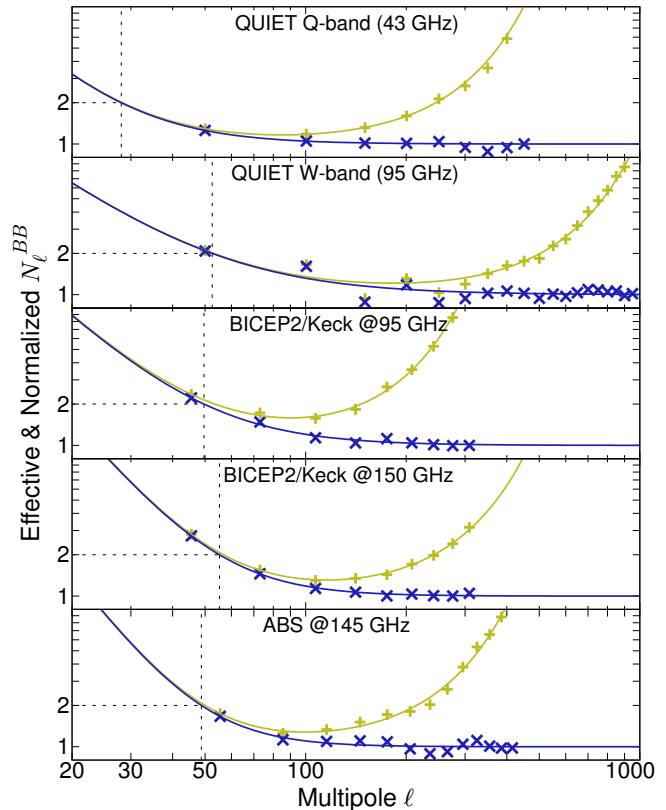


Figure 1. The normalized uncertainties on the C_{ℓ}^{BB} power spectrum achieved by QUIET ([QUIET Collaboration 2011, 2012](#)), BICEP2 and Keck Array ([BICEP2 and Keck Array Collaborations 2016](#)), and ABS ([Kusaka et al. 2018](#)). The yellow data points are $\Delta C_{\ell}^{BB} / \sqrt{2 / [(2\ell + 1) \Delta \ell]} \propto N_{\ell}^{BB}$; the blue points have the beam divided out and are normalized to unity at high ℓ . Solid lines show the modeled curves with Eq. 1. Dashed horizontal lines indicate the location of ℓ_{knee} and are at $\ell \approx 50$ or below.

other frequency bands, the brightness temperature variance due to changes in PWV level is computed for each of the SO bands using the ATM code.

Atmospheric noise has strong spatial correlations and thus does not scale simply with the number of detectors. We account for the increased field of view of the SO LAT relative to ACTPol using the following arguments. First, each optics tube is assumed to provide an independent realization of the atmospheric noise, for angular scales smaller than the separation between the optics tubes. The distance between optics tubes corresponds to $\ell \approx 50$,

well below the effective knee scale in the central frequencies. Since the ACTPol noise spectra are based on measurements for arrays of diameter $\approx 0.1^\circ$, we thus divide the extrapolated ACTPol noise power by the number of SO optics tubes carrying a given band (one for LF, four for MF, and two for HF). Second, each optics tube covers 3 to 4 times the sky area of an ACTPol array; we reduce the noise power by an additional factor of 2 to account for this. The N_{red} factors we adopt are given in Table 2⁷. Because the same water vapor provides the $1/f$ noise at all frequencies, contamination of the two bands within a single optics tube is assumed to be highly correlated and we assign it a correlation coefficient of 0.9.

Figure 2 shows the instrumental and atmospheric noise power spectra for the SO LAT and SAT frequency channels, in temperature and polarization for the LAT, and polarization for the SATs. Correlated $1/f$ noise between channels in the same optics tube (due to the atmosphere) is not shown for clarity, but is included in all calculations in this paper according to the prescription described above.

2.3. Sky coverage

The SATs will primarily be used to constrain the tensor-to-scalar ratio through measuring large-scale B -modes. The LAT will be used to measure the small-scale temperature and polarization power spectra, the lensing of the CMB, the primordial bispectrum, the SZ effects, and to detect extragalactic sources. The LAT’s measurement of CMB lensing may also be used to delens the large-scale B -mode signal measured by the SATs. Our nominal plan for sky coverage is to observe $\approx 40\%$ of the sky with the LAT, and $\approx 10\%$ with the SATs. As we show in this paper, we find this to be the optimal configuration to achieve our science goals given the observing location in Chile and the anticipated noise levels of SO. We do not plan to conduct a dedicated ‘delensing’ survey with the LAT.

Key elements of our SO design study involved assessing the area that can realistically be observed from Chile with the SATs, and determining the optimal area to be surveyed by the LAT. The anticipated SAT coverage, motivated in Stevens et al. (2018), is indicated in Fig. 3 in Equatorial coordinates, and is shown in more detail in Sec. 3. The coverage is non-uniform, represents an effective sky fraction of $\approx 10\text{-}20\%$ accounting for the non-uniform weighting, and has the majority of weight in the Southern sky. This coverage arises from the wide field of view of the SATs, the desire to avoid regions of high Galactic emission, and the need to observe at a limited range of elevations from to achieve lower atmospheric loading. The exact coverage will be refined in future studies, but the sky area is unlikely to change significantly.

The LAT is anticipated to cover the 40% of sky that optimally overlaps with LSST, avoids the brightest part of the Galaxy, and optimally overlaps with DESI given the sky overlap possible from Chile. In our design study we considered 10%, 20%, and 40% sky fractions for the

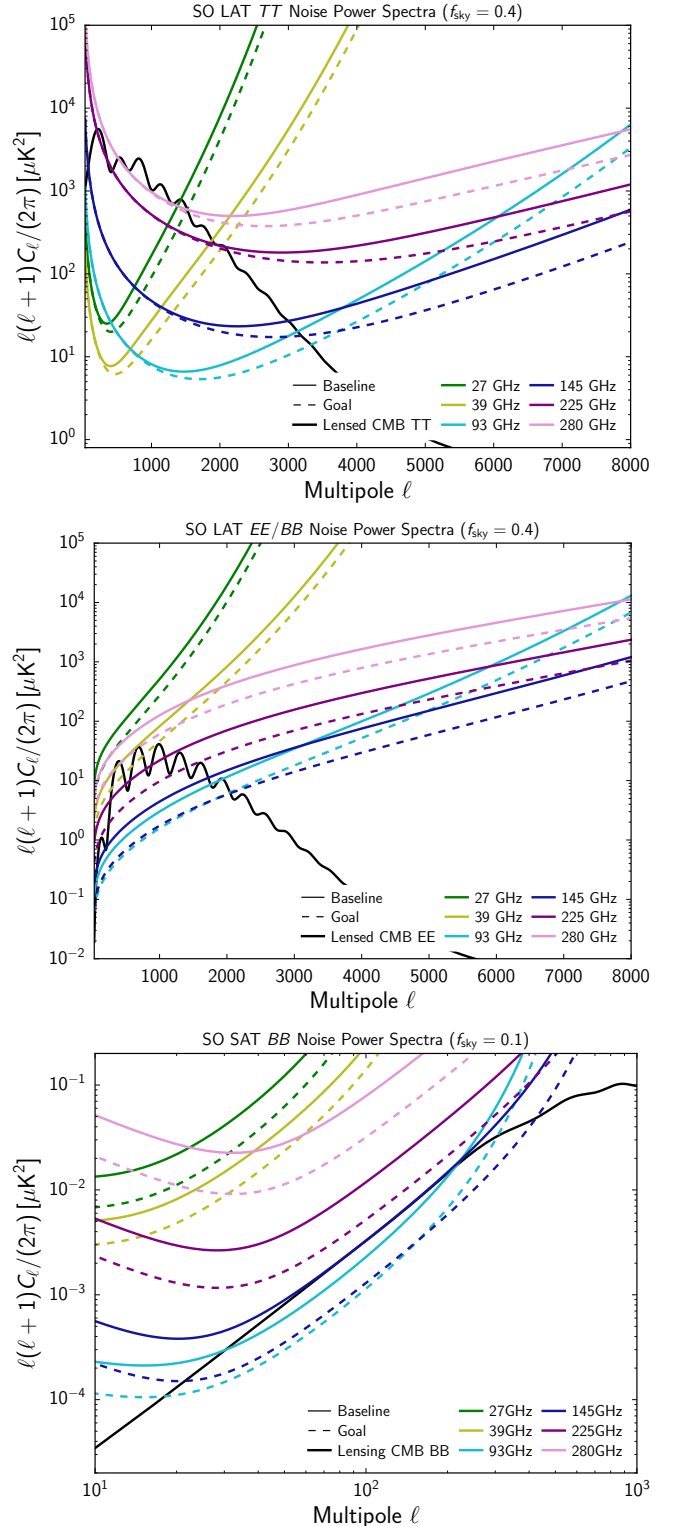


Figure 2. Per-frequency, beam-corrected noise power spectra as in Sec. 2.2 for the LAT temperature (top) and polarization (middle), and the SATs in polarization for the optimistic ℓ_{knee} case of Table 2 (bottom). Baseline (goal) sensitivity levels are shown with solid (dashed) lines, as well as the Λ CDM signal power spectra (assuming $r = 0$). The noise curves include instrumental and atmospheric contributions. Atmospheric noise correlated between frequency channels in the same optics tube is not shown for clarity, but is included in calculations.

⁷ In all forecasts we mistakenly used $N_{\text{red}} = 4 \mu\text{K}^2 s$ instead of $39 \mu\text{K}^2 s$ at 39 GHz. We corrected this error in Fig. 2, and it has negligible effect on forecasts as the *Planck* temperature noise is below the SO noise at these scales.

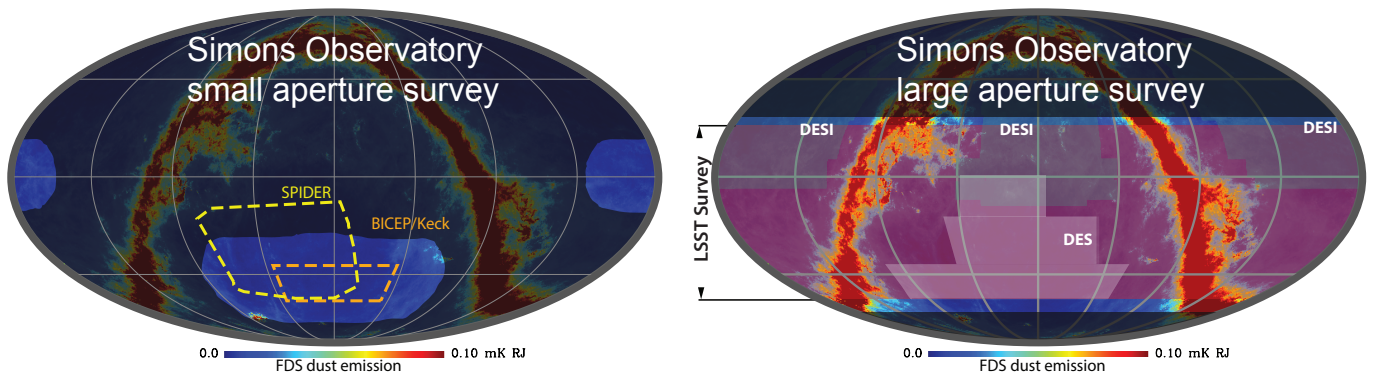


Figure 3. Anticipated coverage (lighter region) of the SATs (left) and LAT (right) in Equatorial coordinates, overlaid on a map of Galactic dust emission. For the SATs we consider a non-uniform coverage shown in Sec. 3. For the LAT, we currently assume uniform coverage over 40% of the sky, avoiding observations where the Galactic emission is high (red), and maximally overlapping with LSST and the available DESI region. This coverage will be refined with future scanning simulations following, e.g., De Bernardis et al. (2016). The survey regions of other experiments are also indicated. The LSST coverage shown here represents the maximal possible overlap with the proposed SO LAT area; while this requires LSST to observe significantly further to the North than originally planned, such modifications to the LSST survey design are under active consideration (Lochner et al. 2018; Olsen et al. 2018).

LAT, to determine the optimal coverage for our science goals.

A limited sky fraction of 10% would, for example, provide maximal overlap between the SATs and LAT, which would be optimal for removing the contaminating lensing signal from the large-scale B -mode polarization, as discussed in Sec. 5. However, we find in Sec. 3 that the impact of limiting the LAT sky coverage on our measurement of the tensor-to-scalar ratio is not significant, which is why we do not anticipate performing a deep LAT survey. In Secs. 4–7 we show how our science forecasts depend on the LAT area, and conclude that SO science is optimized for maximum LAT sky coverage, and maximum overlap with LSST and DESI. We show a possible choice of sky coverage in Fig. 3, which will be refined in further studies.

2.4. Foreground model

Our forecasts all include models for the intensity and polarization of the sky emission, for both extragalactic and Galactic components, and unless stated otherwise we use the common models described in this section. In intensity, our main targets of interest are the higher-resolution primary and secondary CMB signals measured by the LAT. In polarization our primary concern is Galactic emission as a contaminant of large-scale B -modes for the SATs. We also consider Galactic emission as a contaminant for the smaller-scale signal that will be measured by the LAT. We use map-based (Górski et al. 2005, HEALPix⁸) sky simulations in all cases, except for small-scale extragalactic and Galactic polarization for which we use simulated power spectra.

2.4.1. Extragalactic intensity

We simulate maps of the extragalactic components using the Sehgal et al. (2010) model, with modifications to more closely match recent measurements. The extragalactic contributions arise from CMB lensing, the thermal and kinematic SZ effects (tSZ and kSZ, respectively), the cosmic infrared background (CIB), and radio point source emission. The components

are partially correlated; the sources of emission are generated by post-processing the output of an N -body simulation.

Lensed CMB: We use the lensed CMB T map from Ferraro and Hill (2018), generated by applying the LensPix⁹ code to an unlensed CMB temperature map (generated at $N_{\text{side}} = 4096$ from a CMB power spectrum extending to $\ell = 10000$ computed with camb¹⁰) and a deflection field computed from the κ_{CMB} map derived from the Sehgal et al. (2010) simulation.

CIB: We rescale the Sehgal et al. (2010) CIB maps at all frequencies by a factor of 0.75, consistent with the Dunkley et al. (2013) constraint on the 148 GHz CIB power at $\ell = 3000$. These simulations fall short of the actual CIB sky in some ways. The resulting CIB power spectrum at 353 GHz is low compared to the Mak et al. (2017) constraints at lower ℓ . The spectral energy distribution (SED) of the simulated CIB power spectra is also too shallow compared to recent measurements (e.g., van Engelen et al. 2012), in the sense that the model over-predicts the true CIB foreground at frequencies below 143 GHz. The CIB fluctuations in the simulation are correlated more strongly across frequencies than indicated by Planck measurements on moderate to large angular scales (Planck Collaboration 2014e; Mak et al. 2017). However, few constraints currently exist on cross-frequency CIB decorrelation on the small scales relevant for tSZ and kSZ component separation. The tSZ–CIB correlation (Addison et al. 2012) has a coefficient (35% at $\ell = 3000$) a factor of two higher in the simulation than the SPT constraint (George et al. 2015) and Planck (Planck Collaboration 2016i).

While not perfect, this CIB model is plausible and has realistic correlation properties with other fields in the microwave sky. The original simulated CIB maps are provided at 30, 90, 148, 219, 277, and 350 GHz; to construct maps at the SO and Planck frequencies, we perform a pixel-by-pixel interpolation of the flux as a function of frequency using a piecewise linear spline in

⁸ <http://healpix.sf.net/>

⁹ <http://cosmologist.info/lenspix/>

¹⁰ <http://camb.info>

log-log space.

tSZ: We rescale the [Sehgal et al. \(2010\)](#) tSZ map by a factor of 0.75 to approximately match measurements from *Planck* ([Planck Collaboration 2014d, 2016h](#)), ACT ([Sievers et al. 2013](#)), and SPT ([George et al. 2015](#)). The resulting tSZ power spectrum is in good agreement with the 2013 *Planck* *y*-map power spectrum. From the tSZ template map, we construct the tSZ field at all SO and *Planck* frequencies using the standard non-relativistic tSZ spectral function.

kSZ: The power spectrum of the [Sehgal et al. \(2010\)](#) kSZ map is consistent with current upper limits from ACT ([Sievers et al. 2013](#)) and SPT ([George et al. 2015](#)). The kSZ map is approximately frequency independent in the blackbody temperature units that we use here.

Radio point sources: We apply a flux cut to the source population in the [Sehgal et al. \(2010\)](#) simulations, removing those with flux density greater than 7 mJy at 148 GHz. This models the effect of applying a point source mask constructed from sources detected in the maps. We construct the maps by populating the true density field in the simulation with sources, and interpolate to the SO and *Planck* frequencies.

2.4.2. Extragalactic source polarization

We adopt a Poissonian power spectrum of radio point sources, with amplitude $\ell(\ell + 1)C_\ell/(2\pi) = 0.009 \mu\text{K}^2$ at $\ell = 3000$ at 150 GHz (for both *EE* and *BB*). This value is consistent with upper limits from ACTPol ([Louis et al. 2017](#)) and SPTpol ([Henning et al. 2018](#)), and is computed by assuming a Poisson amplitude of $\ell(\ell + 1)C_\ell/(2\pi) = 3 \mu\text{K}^2$ in intensity and a polarization fraction of 0.05. The SED follows [Dunkley et al. \(2013\)](#), with a spectral index of -0.5 in flux units. We assume that the polarization of the CIB, tSZ, and kSZ signals are negligible. For the lensed CMB, we generate the polarization power spectra using `camb`.

2.4.3. Galactic intensity

Our model for Galactic emission intensity includes thermal dust, synchrotron, bremsstrahlung (free-free), and anomalous microwave emission (AME). We use simulated maps that give forecast results consistent with the PySM model ([Thorne et al. 2017](#)), but were generated using an alternative code. For thermal dust we use ‘model 8’ of [Finkbeiner et al. \(1999\)](#) in the [Sehgal et al. \(2010\)](#) simulation, with maps interpolated to the SO and *Planck* frequencies. Due to the SO LAT sky mask and large-scale atmospheric noise, our results are not particularly sensitive to the choice of Galactic thermal dust model. For synchrotron, free-free, and AME we use the *Planck* `Commander` models ([Planck Collaboration 2016k](#)) generated at $N_{\text{side}} = 256$ resolution. We refine these maps to $N_{\text{side}} = 4096$ to match the pixelization of the other maps in our analysis (with additional smoothing applied to suppress spurious numerical artifacts on small scales), but no additional information on sub-degree scales is added.

2.4.4. Galactic polarization

The dominant emission in Galactic polarization is from synchrotron and thermal dust, which we generate in map space for the SAT forecasts using the PySM model ([Thorne et al. 2017](#)), which extrapolates template Galactic emission maps estimated from *Planck* and WMAP data. They are scaled in frequency for both *Q* and *U* Stokes parameters assuming a curved power law and a modified blackbody spectrum, respectively

$$S_\nu^{\text{synch}} = \left(\frac{\nu}{\nu_0}\right)^{\beta_s + C \log(\nu/\nu_0)}, \quad S_\nu^{\text{dust}} = \frac{\nu^{\beta_d} B_\nu(T_d)}{\nu_0^{\beta_d} B_{\nu_0}(T_d)}, \quad (2)$$

where β_s is the synchrotron spectral index, C is the curvature of the synchrotron index, β_d the dust emissivity, T_d the dust temperature, and ν_0 a pivot frequency. All spectral parameters, except for the synchrotron curvature, vary across the sky on degree scales. We make the following choices to generate PySM simulations with three different levels of complexity:

‘*Standard*’: this corresponds to the PySM ‘a1d1f1s1’ simulation ([Thorne et al. 2017](#)), assuming a single modified-blackbody polarized dust and a single power-law synchrotron component. These use spatially varying spectral indices derived from the intensity measurements from *Planck* ([Planck Collaboration 2016c](#)). We compare the *B*-mode amplitude and frequency dependence of these foregrounds to the expected cosmological *B*-mode signal from lensing in [Fig. 4](#).

‘*2 dust + AME*’: this corresponds to the ‘a2d7f1s3’ PySM model described in [Thorne et al. \(2017\)](#), i.e., a power law with a curved index for synchrotron, dust that is decorrelated between frequencies, and an additional polarized AME component with 2% polarization fraction.

‘*High-res. β_s* ’: this includes small scale (sub-degree) variations of the synchrotron spectral index β_s simulated as a Gaussian realization of a power law angular spectrum with $C_\ell \propto \ell^{-2.6}$ ([Krachmalnicoff et al. 2018](#)).

For the LAT forecasts, we model the power spectra of the polarized components instead of using simulated maps. The power spectra of thermal dust and synchrotron are taken as power laws, with $C_\ell^{\text{dust}} \propto \ell^{-2.42}$, following measurements by *Planck* ([Planck Collaboration 2016q](#)), and $C_\ell^{\text{synch}} \propto \ell^{-2.3}$ ([Choi and Page 2015](#)). The dust spectral parameters defined in [Eq. 2](#) are $\beta_d = 1.59$ and dust temperature 19.6 K ([Planck Collaboration 2016q](#)), and the synchrotron spectral index is fixed to $\beta_s = -3.1$ ([Choi and Page 2015](#)). The *EE* and *BB* dust power spectrum amplitudes are normalized to the amplitudes at $\ell = 80$ for the PySM default sky model evaluated at 353 GHz for dust and 27 GHz for synchrotron (using the appropriate SO LAT sky mask). We include the cross-power due to dust–synchrotron correlations via a correlation coefficient (see, e.g., [Eq. 6](#) of [Choi and Page 2015](#)), determined by normalizing the model to the PySM model evaluated at 143 GHz in the SO LAT sky mask, after accounting for the dust and synchrotron auto-power.

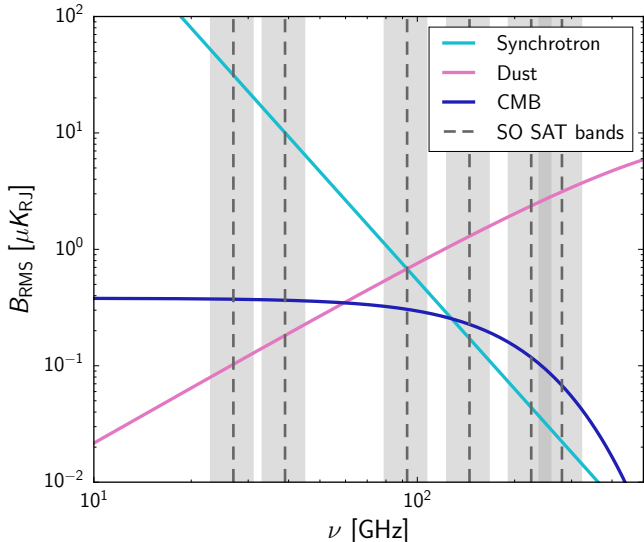


Figure 4. Frequency dependence, in RJ brightness temperature, of the synchrotron and thermal dust emission at degree scales within the proposed footprint for the SATs, compared to the CMB lensing B -mode signal. The turnover of the modified blackbody law for the dust lies above this frequency range.

2.5. Foreground cleaning for the LAT

Here we describe the foreground removal method used for the LAT, which is then propagated to Fisher forecasts for parameters derived from the temperature and E -mode power spectrum (Sec. 4), the lensing spectrum (Sec. 5), the primordial bispectrum (Sec. 6) and the SZ effects (Sec. 7). Our forecasts for primordial large-scale B -modes, the main science case for the SAT, are based on the comparison of a number of component separation methods run on map-level foreground and noise simulations, and are described in Sec. 3.

We generate signal-only simulations at the SO LAT frequencies and the *Planck* frequencies at 30, 44, 70, 100, 143, 217, and 353 GHz. The noise properties of the SO LAT channels are described in Sec. 2.2. The white noise levels and beams for the *Planck* frequencies are drawn from [Planck Collaboration \(2016a\)](#) (30, 44, and 70 GHz) and [Planck Collaboration \(2016b\)](#) (70, 100, 143, 217, and 353 GHz).¹¹ This yields thirteen frequency channels, which we take to have δ -function bandpasses for simplicity. We consider three SO LAT survey regions covering 10%, 20%, and 40% of the sky.¹² We measure the auto- and cross-power spectra at all frequencies, considering scales up to $\ell_{\max} = 8000$. We correct for the mask window function using a simple f_{sky} factor, given

¹¹ After these calculations were performed, the *Planck* products were updated with the final LFI and HFI mission processing ([Planck Collaboration 2018b,c](#)). Since the temperature noise levels have not changed compared to 2015, and as the SO LAT polarization noise is lower than that of *Planck* at all relevant scales, we do not anticipate our forecasts to change with the updated *Planck* noise levels.

¹² The region retaining a sky fraction of 40% was originally selected to minimize the polarized Galactic contamination and does not precisely match the planned sky area for the LAT shown in Fig. 3, which has since been tuned to have improved overlap with LSST and DESI. However, we estimate the impact on forecasts of choosing between these two different sky masks to be small.

the large sky area and lack of small-scale structure in the mask. We then add the instrumental and atmospheric noise power spectra for SO described in Sec. 2.2, and white noise power for *Planck*, to form a model of the total observed auto- and cross-power spectra.

2.5.1. Component separation method

We implement a harmonic-space Internal Linear Combination (ILC) code to compute post-component-separation noise curves for various LAT observables (e.g., [Bennett et al. 2003](#); [Eriksen et al. 2004](#)). While a more sophisticated method ([Delabrouille et al. 2009](#), e.g., Needlet ILC) will likely be used in actual analyses, the harmonic-space ILC is rapid enough to enable calculations for many experimental scenarios and sky models. This is essential for optimization of the SO LAT frequency channels, while still being representative of the likely outcome using other methods. Moreover, harmonic-space ILC forecasts can be evaluated given only models for the power spectra of the sky components (i.e., maps are not explicitly required). Although we simulate maps for the temperature sky, our limited knowledge of small-scale polarized foregrounds forces us to rely on power-spectrum-level modeling for polarization (however, see [Hervías-Caimapo et al. \(2016\)](#) for steps toward simulating such maps), and thus harmonic-space ILC is necessary in this case.

In the following, we consider forecasts for ‘standard ILC’, in which the only constraints imposed on the ILC weights are: (i) unbiased response to the known spectral energy distribution (SED) of the component of interest (e.g., CMB) and (ii) minimum variance (in our case, at each ℓ). We also consider ‘constrained ILC’ (e.g., [Remazeilles et al. 2011](#)), in which an additional constraint is imposed: (iii) zero response to some other component(s) with specified SED(s). We refer to this additional constraint as ‘deprojection’. Since this constraint uses a degree of freedom, i.e., one of the frequency channel maps, the residual noise after component separation is higher for constrained ILC than for standard ILC. We use the deprojection method as a conservative choice that reflects the need to explicitly remove contaminating components that may bias some analysis, even at the cost of increased noise (e.g., tSZ biases in CMB lensing reconstruction). Deprojection will impose more stringent requirements than standard ILC on the ability of the experiment’s frequency coverage to remove foregrounds.

For temperature forecasts, we consider deprojection of the thermal SZ spectral function and/or a fiducial CIB SED (or, in the case of tSZ reconstruction, deprojection of CMB and/or CIB). For polarization forecasts, we consider deprojection of a fiducial polarized dust SED and/or of a fiducial polarized synchrotron SED. Clearly, for components with SEDs that are not known *a priori* from first principles, deprojection could leave residual biases; these can be minimized in practice by sampling over families of SEDs ([Hill in prep.](#)). For later reference, we provide a dictionary of the relevant deprojection choices here:

CMB Temperature Cleaning:
 Deproj-0: Standard ILC
 Deproj-1: tSZ deprojection
 Deproj-2: Fiducial CIB SED deprojection

Deproj-3: tSZ and fiducial CIB SED deprojection

Thermal SZ Cleaning:

Deproj-0: Standard ILC

Deproj-1: CMB deprojection

Deproj-2: Fiducial CIB SED deprojection

Deproj-3: CMB and fiducial CIB SED deprojection

CMB Polarization Cleaning:

Deproj-0: Standard ILC

Deproj-1: Fiducial polarized dust SED deprojection

Deproj-2: Fiducial polarized synchrotron SED deprojection

Deproj-3: Fiducial polarized dust and synchrotron SED deprojection

2.5.2. Post-component-separation noise

We compute SO LAT post-component separation noise for CMB temperature maps, thermal SZ maps, and CMB polarization maps (E - and B -mode). We consider both the baseline and goal SO noise levels, as well as three sky fraction options (10%, 20%, and 40%) and the four foreground deprojection methods. These are the final LAT noise curves used throughout later sections of the paper for forecasting. As an illustration, we show noise curves for the LAT in Fig. 5 for CMB temperature and CMB E -mode polarization, for a wide survey ($f_{\text{sky}} = 0.4$). A similar figure for tSZ reconstruction can be found in Sec. 7.2. The figure shows the post-component-separation noise for various foreground cleaning methods and assumed noise levels. It also shows the pure inverse-noise-weighted (i.e., zero-foreground) channel-combined noise for the goal scenario, which allows a straightforward assessment of the level to which the foregrounds inflate the noise. In temperature, the foregrounds have a large effect; in contrast, in E -mode polarization at high- ℓ , the foregrounds are expected to have little effect, making this a prime region for cosmological parameter extraction from the primary CMB.

We use the temperature and polarization noise curves to obtain the lensing noise $N_L^{\kappa\kappa}$ assuming quadratic estimators are used to reconstruct the lensing field, as described in Hu et al. (2007a). We calculate the noise from five estimators (TT , ET , TB , EE , EB), and we combine the last two to obtain ‘polarization only’ noise curves and combine all of them to obtain ‘minimum variance’ noise curves. We show example lensing noise curves in Fig. 6 for a wide survey with SO LAT ($f_{\text{sky}} = 0.4$) and two foreground cleaning cases: (i) standard ILC for both CMB temperature and polarization cleaning, and (ii) tSZ and fiducial CIB SED deprojection for CMB temperature cleaning and fiducial polarized dust and synchrotron SED deprojection for CMB polarization cleaning.

Using these noise curves and anticipated sky coverage (40% for the LAT, and 10% for the SATs), we show the forecast errors on the temperature, polarization, and lensing power spectra in Fig. 7. These include the anticipated instrument noise and foreground uncertainty, but do not include any additional systematic error budget. Fig. 7 also shows projected errors for the B -mode power spectrum described in Sec. 3.

2.5.3. Optimization

Our nominal noise curves correspond to the SO LAT frequency distribution given in Table 1. However, to determine this frequency distribution, we performed a full end-to-end optimization for various LAT observables. This study will be described elsewhere, but we provide a summary here for reference. We considered a range of sky areas (from $f_{\text{sky}} = 0.03$ to 0.4) and all configurations of LAT optics tubes, with the constraint that there are a total of seven tubes, and they can each have 27/39 GHz, 93/145 GHz, or 225/280 GHz.

Using the noise calculator described in Simons Observatory Collaboration (in prep.) and Hill et al. (2018), we computed the SO LAT noise properties for each choice of survey region and experimental configuration, and then processed these noise curves through the foreground modeling and component separation methodology described in the previous subsections. We then used the post-component-separation noise curves to determine the S/N of various SO LAT observables: the CMB TT power spectrum, the CMB lensing power spectrum reconstructed via the TT estimator, the tSZ power spectrum, the kSZ power spectrum, the CMB EE power spectrum, the CMB BB power spectrum (lensing-only), and the CMB lensing power spectrum reconstructed via the EB estimator. We repeated this analysis for the set of deprojection assumptions in the ILC foreground cleaning, which impose different constraints on the frequency channel distribution. We found a set of configurations that was near-optimal for all observables (i.e., maximized their S/N) when using the simplest foreground cleaning method, and then we identified a near-optimal configuration that was also robust to varying the foreground cleaning method. This process yielded the final choice of the SO LAT optics tube distribution and survey area: one low-frequency tube, four mid-frequency tubes, and two high-frequency tubes, with the widest possible survey ($f_{\text{sky}} = 0.4$).

2.6. Parameter estimation and external data

The majority of our parameter forecasts use Fisher matrix approaches, with the foreground-marginalized noise curves described above as inputs. An important exception to this is the measurement of large-scale B -modes, described in Sec. 3. In this case the foregrounds are a more significant contaminant so we perform end-to-end parameter estimates on a suite of simulations: foreground-cleaning the maps, estimating B -mode power spectra, and then estimating parameters.

Unless stated otherwise we assume a six-parameter Λ CDM model as nominal (baryon density, $\Omega_b h^2$, cold dark matter density, $\Omega_c h^2$, acoustic peak scale, θ , amplitude and spectral index of primordial fluctuations, A_s and n_s , and optical depth, τ), and add additional parameters as described in each of the following sections. As reference cosmology we assume the parameters from the Planck Collaboration (2016e) Λ CDM temperature fit, except for τ which is assumed to be 0.06 in agreement with Planck Collaboration (2016o). We use the Boltzmann codes `camb` and `class`¹³ to generate theoretical predictions, using updated recombination models,

¹³ <http://www.class-code.net/>

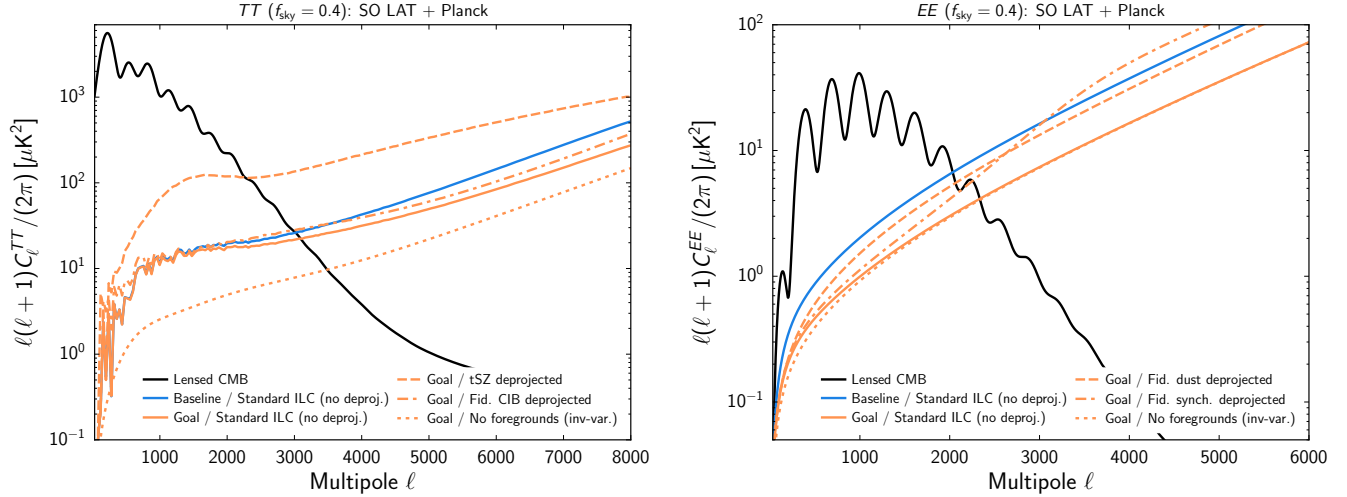


Figure 5. Post-component-separation noise curves for the combination of six SO LAT (27–280 GHz) and seven *Planck* (30–353 GHz) frequency channels, assuming a wide SO survey with $f_{\text{sky}} = 0.4$, compared to the expected signal (black). The left (right) panel shows CMB temperature (E -mode polarization). Foregrounds and component separation are implemented as in Sec. 2.4 and Sec. 2.5.1, considering multipoles up to $\ell_{\text{max}} = 8000$. The blue (orange) curves show the component-separated noise for the SO baseline (goal) noise levels, assuming standard ILC cleaning. The dashed and dash-dotted curves show various ILC foreground deprojection options, described in Sec. 2.5.1. The tSZ deprojection penalty is larger than that for CIB deprojection because of (i) the relatively high noise at 225 GHz compared to 93 and 145 GHz and (ii) the lack of a steep frequency lever arm for the tSZ signal as compared to the CIB. The dotted orange curves show the no-foreground goal noise, i.e., when SO LAT and *Planck* channels are combined via inverse-noise weighting. This is the minimal possible noise that could be achieved. The temperature noise curves fluctuate at low- ℓ due to the use of actual sky map realizations, as opposed to the analytic power-spectrum models in polarization.

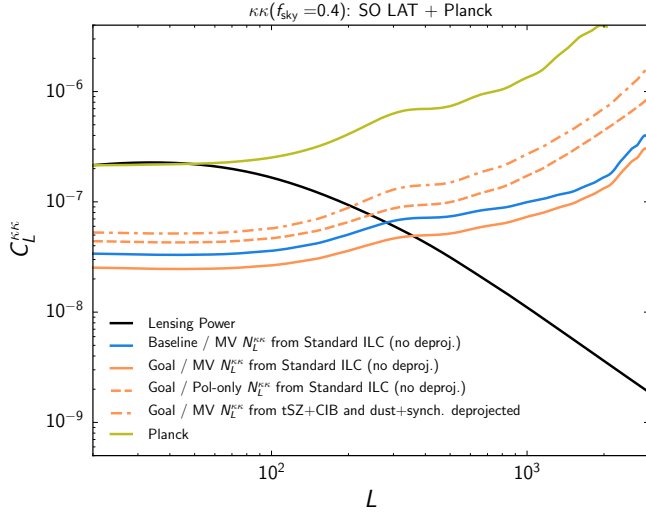


Figure 6. ΛCDM CMB lensing power spectrum (black) compared to SO LAT lensing noise curves, $N_L^{\kappa\kappa}$, reconstructed assuming a polarization only (Pol-only) or minimum variance (MV) combination of estimators in the case of standard ILC for both CMB temperature and polarization cleaning (solid and dashed curves), and tSZ and fiducial CIB SED deprojection for CMB temperature cleaning and fiducial polarized dust and synchrotron SED deprojection for CMB polarization cleaning (dot-dashed curve). SO baseline and goal scenarios are shown in blue and orange, respectively, and compared to the *Planck* lensing noise (Planck Collaboration 2018e, yellow). SO will be able to map lensing modes with $S/N > 1$ to $L > 200$.

with additional numerical codes to generate statistics including cluster number counts and cross-power spectra between CMB lensing and galaxy clustering.

We combine SO data with additional sky and frequency coverage provided by *Planck*. For the SATs this is done by assuming the *Planck* intensity data will be used at large scales. We also assume a prior on the optical depth

of $\tau = 0.06 \pm 0.01$ (Planck Collaboration 2016o; neglecting the small change in the mean value and the improvement to $\sigma(\tau) = 0.007$ with the 2018 results; Planck Collaboration 2018d). For the LAT, the *Planck* data are included in the co-added noise curves over the sky common to both experiments. Additionally, for the largest angular ranges not probed by SO, we include TT , TE and EE from *Planck* over 80% of the sky at $2 \leq \ell \leq 29$. For the sky area not accessible to SO, we add an additional 20% of sky from *Planck* in the angular range $30 \leq \ell \leq 2500$. This produces an overall sky area of 60% which is compatible with the area used by *Planck* after masking the Galaxy. For the *Planck* specifications we follow the procedure described in Allison et al. (2015) and Calabrese et al. (2017), scaling the overall white noise levels to reproduce the full mission parameter constraints. For reference, we give forecast constraints on the ΛCDM parameters in Table 3 for SO combined with *Planck*, compared to the published results from *Planck* alone ($TT, TE, EE + \text{lowE} + \text{lensing}$, Planck Collaboration 2018d). Both cases use temperature, polarization, and lensing data. In this paper we will refer to ‘SO Baseline’ and ‘SO Goal’ forecasts; these all implicitly include *Planck*.

In many cases we combine SO forecasts with DESI and LSST. For LSST we consider an overlap area of $f_{\text{sky}} = 0.4$ and two possible galaxy samples. First is the ‘gold’ sample, which has galaxies with a dust-corrected $i < 24.5$ magnitude cut after three years of LSST observations. This corresponds to 29.4 galaxies arcmin $^{-2}$ and $n(z) \propto z^2 \exp[-(z/0.27)^{0.92}]$ following LSST Science Collaboration (2009) and Chang et al. (2013). Second, we consider a more optimistic LSST galaxy sample with dust-corrected $i < 27$ and a $S/N > 5$ cut with ten years of LSST observation, following Gorecki et al. (2014). In that sample we include a possible sample of Lyman-break

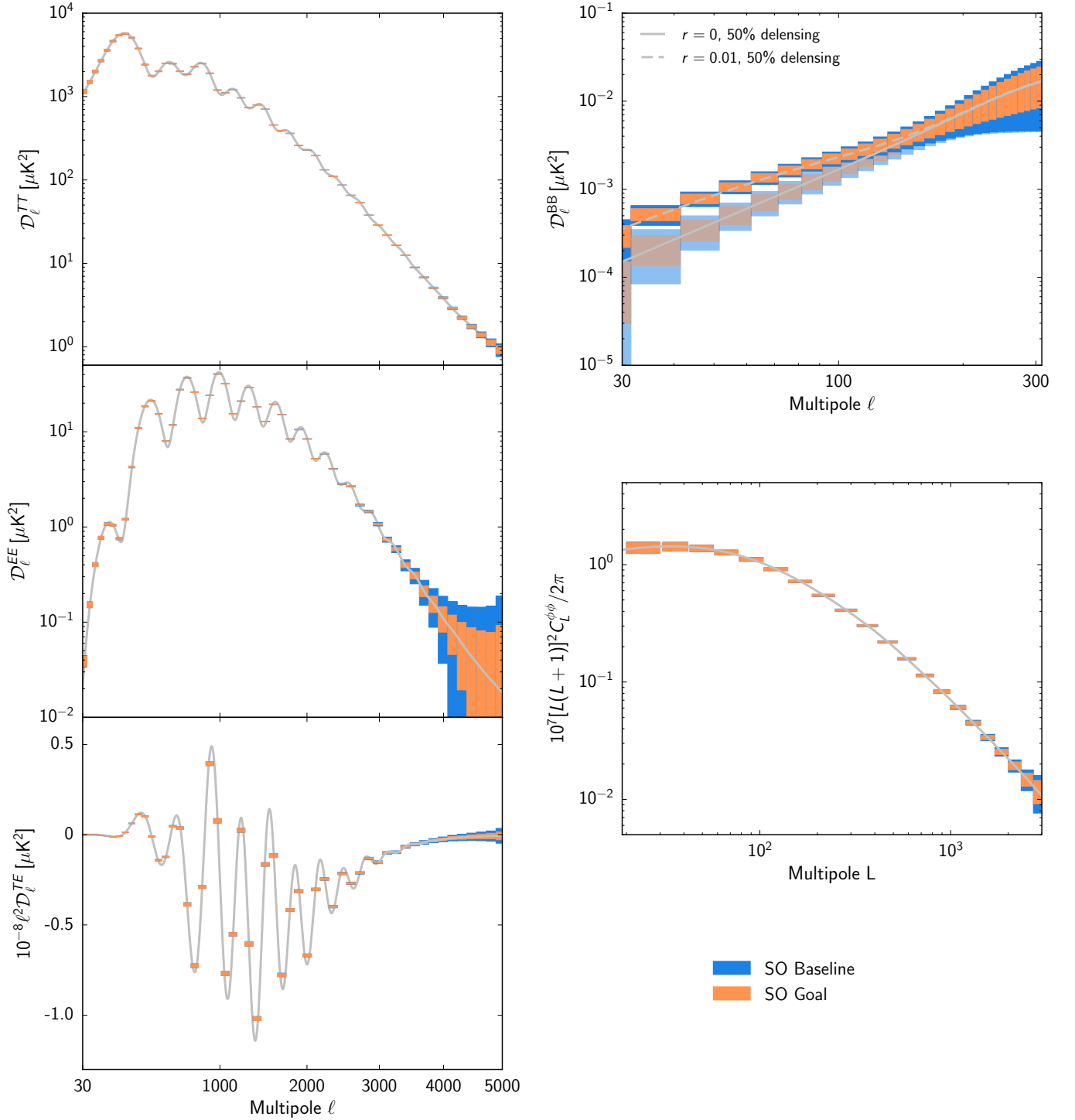


Figure 7. Forecast SO baseline (blue) and goal (orange) errors on CMB temperature (TT), polarization (EE , BB), cross-correlation (TE), and lensing ($\phi\phi$) power spectra, with $\mathcal{D}_\ell \equiv \ell(\ell+1)C_\ell/(2\pi)$. The errors are cosmic-variance limited at multipoles $\ell \lesssim 3000$ in T and $\ell \lesssim 2000$ in E . The B -mode errors include observations from both SAT and LAT surveys, and incorporate the uncertainty associated with foreground removal using BForE (see Sec. 3.3) for the optimistic ℓ_{knee} given in Table 2. The CMB signals for a fiducial ΛCDM cosmology (ΛCDM +tensor modes in the case of BB) are shown with gray solid (dashed) lines.

Table 3

Forecasts of Λ CDM parameter uncertainties for SO compared to *Planck*^a

Parameter	<i>Planck</i>	SO-Baseline+ <i>Planck</i>
$\Omega_b h^2$	0.0001	0.00005
$\Omega_c h^2$	0.001	0.0007
H_0 [km/s/Mpc]	0.5	0.3
$10^9 A_s$	0.03	0.03
n_s	0.004	0.002
τ	0.007	0.007

^aThe ‘*Planck*’-only constraints reported here are from the final 2018 *Planck* data (Planck Collaboration 2018d). We check that our *Planck* forecast code (using T/E at $2 \leq \ell \leq 29$ with $f_{\text{sky}} = 0.8$, $TT/TE/EE$ at $30 \leq \ell \leq 2500$ with $f_{\text{sky}} = 0.6$, and $\kappa\kappa$ at $8 \leq L \leq 400$ with $f_{\text{sky}} = 0.6$) yields similar results, except for small differences: we find $\sigma(H_0) = 0.6$ km/s/Mpc, $\sigma(10^9 A_s) = 0.04$, $\sigma(\tau) = 0.009$.

galaxies at $z=4-7$, identified using the dropout technique (see Dunlop 2012 for a review), with a number density estimated by extrapolating recent Hyper Suprime-Cam (HSC) results (Ono et al. 2018, Harikane et al. 2017, following Schmittfull and Seljak 2018).

For DESI we include projected measurements of the baryon acoustic oscillation (BAO) scale, by imposing a prior on r_s/D_V at multiple redshifts, as described in Levi et al. (2013). Here, r_s is the sound horizon at decoupling and D_V is the volume distance. We consider the DESI Luminous Red Galaxy (LRG) catalog as providing the target galaxies for the SZ studies described in Sec. 7. In these forecasts we assume an overlap area of 9000 square degrees between SO and DESI ($f_{\text{sky}} = 0.23$).

Throughout the paper we will retain two significant figures in many of our forecast errors to enable comparison of different experimental configurations. In the summary table we restrict errors to one significant figure.

3. LARGE-SCALE B -MODES

In this section we describe the motivation for measuring large-scale B -modes (Sec. 3.1), the challenges for measuring them in practice (Sec. 3.2), our forecasting machinery (Sec. 3.3), and our forecast constraints (Sec. 3.4), including a discussion of limitations in Sec. 3.5.

3.1. Motivation

Large-scale B -modes offer a unique window into the early universe and the physics taking place at very high energies. Primordial tensor perturbations, propagating as gravitational waves, would polarize the CMB with this particular pattern (Kamionkowski et al. (1997); Zaldarriaga and Seljak (1997)). Since scalar perturbations generate only primary E -mode polarization, the amplitude of the B -mode signal provides an estimate of the tensor-to-scalar ratio, r . While the scalar perturbations have been well characterized by, e.g., Planck Collaboration (2018d), we so far have only upper limits on the amplitude of tensor perturbations, with $r < 0.07$ at 95% confidence (BICEP2/Keck and Planck Collaborations 2015; Planck Collaboration 2018d) at a pivot scale of $k = 0.05/\text{Mpc}$.

Theories for the early universe can be tested via their predictions for the tensor-to-scalar ratio, in addition to other properties of the primordial perturbations including the shape of the primordial scalar power spectrum

and the scalar spectral index (Sec. 4.2 and Table 3), degree of non-Gaussianity (Sec. 6), and degree of adiabaticity. While late-time probes of structure formation can be used to further characterize the scalar perturbations, the CMB is likely to be the most powerful probe to constrain the tensor-to-scalar ratio on large scales.

Simple inflationary models can generate tensor perturbations at a measurable level. The current upper limit on r already excludes a set of single-field slow-roll inflation models, as illustrated in, e.g., Planck Collaboration (2018d,f). As discussed in, e.g., Abazajian et al. (2016), there is a strong motivation to further lower the current limits, with certain large-field plateau models predicting an $r \approx 0.003$ (e.g., Starobinsky 1980). SO, through its sensitivity, frequency coverage and angular resolution, is designed to be able to measure a signal at the $r = 0.01$ level at a few σ significance, or to exclude it at similar significance, using the B -mode amplitude around the recombination bump at $\ell \approx 90$. A detection of a signal at this level or higher would constitute evidence against classes of inflationary models (Martin et al. 2014b,a), e.g., $r \propto 1/N^2$ models¹⁴ such as Higgs or R^2 inflation (Starobinskiĭ 1979; Bezrukov and Shaposhnikov 2008). Measurably large tensor perturbations can also be generated by additional time-varying fields during inflation which contribute negligibly to inflation dynamics (Namba et al. 2016).

On the other hand, alternative non-inflationary cosmologies include scenarios in which the big bang singularity is replaced by a bounce – a smooth transition from contraction to expansion (Ijjas and Steinhardt 2018). During the slow contraction phase that precedes a bounce, the universe is smoothed and flattened and nearly scale-invariant super-horizon perturbations of quantum origin are generated that seed structure in the post-bounce universe (Levy et al. 2015). These models are not expected to produce detectable tensor perturbations, and therefore a detection of primordial B -modes would allow us to rule them out.

Beyond the tensor-to-scalar ratio, measurements of the large scale polarization signal could be used to explore constraints on the tensor tilt, n_T . Although these constraints would be weak even in a case with $r \sim 0.01$ and 50% delensing (with projected statistical uncertainty $\sigma(n_T) \approx 0.6$), SO would be able to test large deviations from the consistency relation for simple inflationary models predicting $r = -8n_T$.

The data could also be used to test for the presence of non-standard correlations such as non-zero TB and EB , generated by early- or late-time phenomena, e.g., chiral gravitational waves and Faraday rotation (see e.g., POLARBEAR Collaboration 2015; Contaldi 2016; Abazajian et al. 2016; Planck Collaboration 2016n; BICEP2 Collaboration et al. 2017).

3.2. Measuring B -modes

Figure 4 shows the amplitude of the CMB lensing B -modes compared to the two main polarized Galactic contaminants: synchrotron and dust emission. Our goal is to search for a primordial B -mode signal that is of the same order or smaller than this lensing signal. Although

¹⁴ Here N is the number of e -folds of inflation.

the level of contamination depends on the sky region, polarized foregrounds are known to have amplitudes corresponding roughly to $r=0.01\text{--}0.1$ (Krachmalnicoff et al. 2016) at their minimum frequency (70–90 GHz). As a function of scale, foreground contamination can be up to two orders of magnitude higher than the CMB B -mode power spectrum (see Fig. 11), which itself is dominated by non-primordial lensing B -modes over the scales of interest for SO (BICEP2/Keck and Planck Collaborations 2015). Our forecasts will therefore focus both on $\sigma(r)$, the 1σ statistical uncertainty on r after foreground cleaning, as well as on the possible bias on r caused by foreground contamination.

To discriminate between the primordial CMB signal and other sources of B -modes, SO will use multi-frequency observations to characterize the spectral and spatial properties of the different components and remove the foreground contribution to the sky’s B -mode signal. Lensing B -modes can be viewed as an additional source of stochastic noise, with an almost-white power spectrum with a $\sim 5\ \mu\text{K-arcmin}$ amplitude on the largest angular scales (Hu and Okamoto 2002). Fortunately, this contamination can be partially removed at the map level through a reconstruction of the lensing potential. For SO this reconstruction will be based on external large-scale structure datasets, such as maps of the CIB, as well as on internal CMB lensing maps estimated from the LAT observations. Further details can be found in Sec. 5.1.

While our forecasts in this paper focus on using data from the SATs to clean and estimate the large-scale B -modes, the complementarity between the SATs and the LAT will allow us to perform component characterization and subtraction over a wide range of angular scales, adding to the robustness of our foreground cleaning. SO will also provide the community with new high-resolution templates of the Galactic polarized emission (both on its own, and in combination with high-frequency data from balloon-borne experiments or low frequency measurements from other ground-based facilities). Complementary to *Planck* data, this will provide valuable information on the characteristics of the dust populations and the properties of the Galactic magnetic field.

3.3. Forecasting tools

Our B -mode forecasts are based on a set of foreground cleaning and power spectrum estimation tools. We use the following suite of four foreground cleaning codes:

- **Cross-spectrum (C_ℓ -MCMC)**: is a method that models the BB cross-spectra between the six frequencies similarly to Cardoso et al. (2008) and BICEP2/Keck and Planck Collaborations (2015). The free parameters of the foreground contribution are the dust and synchrotron spectral indices $\{\beta_d, \beta_s\}$, and the amplitude and power-law tilt of their power spectra ($\{A_{BB}^d, A_{BB}^s\}$ and $\{\alpha_d, \alpha_s\}$, respectively). The method fixes the dust temperature to $T_d = 19.6\text{ K}$, the synchrotron curvature to $C = 0$, and explicitly ignores the spatial variation of the other spectral parameters. Finally, the noise bias is modeled by averaging the spectra of noise-only simulations that reproduce both the inhomogeneous sky coverage and the effect of $1/f$ noise. Fifty simulations were used for each case explored.

A Fisher-matrix version of this method (**C_ℓ -Fisher**) was also used to obtain fast estimates of $\sigma(r)$ for a large number of different instrumental configurations and survey strategies. The code marginalizes over a larger set of 11 cosmological and foreground parameters, including E -mode and B -mode amplitudes $\{A_{EE}^d, A_{BB}^d, A_{EE}^s, A_{BB}^s\}$, and tilts $\{\alpha_s, \alpha_d\}$, spectral parameters $\{\beta_s, \beta_d\}$, a dust-synchrotron correlation parameter ρ_{ds} , the lensing amplitude A_{lens} and the tensor-to-scalar index r . The results of this method were verified against **xForecast**, and informed some of the main decisions taken during the experiment design stage.

- **xForecast**: (Stompor et al. 2016) is a forecast code that uses a parametric pixel-based component separation method, explicitly propagating systematic and statistical foregrounds residuals into a cosmological likelihood. For this paper, the algorithm has been adapted to handle inhomogeneous noise and delensing. By default, the code fits for a single set of spectral indices $\{\beta_d, \beta_s\}$ over the whole sky region, fixing the dust temperature to 19.6 K. The inherent spatial variability of the spectral parameters in the input sky simulations naturally leads to the presence of systematic foreground residuals in the cleaned CMB map, and therefore can produce a non-zero bias in the estimation of r . We explore extensions to this method that marginalize over residual foregrounds as described in Sec. 3.4.2.
- **BFoRe**: (Alonso et al. 2017) is a map-based foreground removal tool that fits for independent spectral parameters for the synchrotron and dust in separate patches of the sky. We use BFoRe as an alternative to **xForecast** to explore certain scenarios with a higher degree of realism. These imply running an ensemble of simulations with independent CMB and noise realizations in order to account for the impact of foreground residuals in the mean and standard deviation of the recovered tensor-to-scalar ratio. For these forecasts, 20 simulations were generated for each combination of sky and instrument model.
- **Internal Linear Combination**: We also implemented a B -mode foreground-cleaning pipeline based on the Internal Linear Combination (ILC) method (Bennett et al. 2003). Our implementation calculates the ILC weights in harmonic space in a number of ℓ bands and marginalizes over the residual foregrounds at the power spectrum level in the cosmological likelihood, see Sec. 3.4.2. The method is similar to that used in Appendix A of the CMB-S4 CDT report¹⁵. This pipeline was run on 100 sky simulations for each of the cases explored here.

All of these methods are based on the same signal, noise and foregrounds models and, except for the C_ℓ -Fisher method, all use the same foreground simulations. All

¹⁵ https://www.nsf.gov/mps/ast/aaac/cmb_s4/report/CMBS4_final_report_NL.pdf

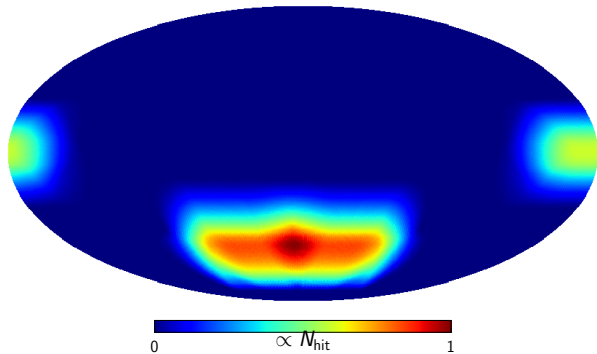


Figure 8. Simulated map of hit counts in Equatorial coordinates for the SATs, resulting from the preliminary scan strategy considered in this study. The N_{hit} is proportional to the amount of time anticipated to be spent observing each pixel. Regions of high Galactic emission are avoided.

methods make extensive use of HEALPix for the manipulation of sky maps.

For power spectrum estimation we use the following code:

- **NaMaster**:¹⁶ a software library that implements a variety of methods to compute angular power spectra of arbitrary spin fields defined on the sphere. We use the code to estimate pure- B power spectra from our simulations. Pure- B estimators (Smith 2006; Grain et al. 2009) minimize the additional sample variance from the leakage of E modes due to the survey footprint and data weighting.

Finally, we note that, for simplicity, our forecasts assume a Gaussian likelihood for the B -mode power spectrum over the scales probed ($30 \leq \ell \leq 300$). This is not guaranteed to be a valid assumption given the reduced sky fraction and possible filtering of the data, and should be replaced in the future by, for example, the more accurate likelihood of Hamimeche and Lewis (2008).

3.4. Forecast constraints

This section discusses the impact of the large-area scanning strategy pursued by the SATs, and our fiducial forecasts for $\sigma(r)$ after component separation. We also explore departures from the fiducial hypotheses, including different assumptions about delensing, the fiducial r model, and the foreground models.

3.4.1. Impact of large-area scanning strategy

The combination of the anticipated scanning strategy with the large field-of-view of the SATs gives rise to a sky coverage with broad depth gradients around a small effective area of $A \simeq 4000$ square degrees, as shown in Fig. 8. A more compact sky coverage would arguably be more optimal for B -mode searches. However, B -modes cannot be measured locally, and on a cut sky some signal is lost near the patch boundaries, which could have a significant impact on the signal-to-noise obtained from a compact sky mask. This is probably negligible, however, for the broad area covered by this scanning strategy, given that the shallower regions must also be down-weighted in an

inverse-variance way (i.e., with a window function proportional to the local hit counts in the simplest case). It is therefore important to assess the level to which this choice of survey strategy and field of view could degrade the achievable constraints on the tensor-to-scalar ratio with SO.

To do this we have considered two different types of survey window functions: the one described above and a window function with homogeneous depth over a circular patch with the same hit counts. For each of them, we generate 1000 sky simulations containing only the CMB signal with $r = 0$ and lensing amplitude $A_{\text{lens}} = 1, 0.5$ and 0.25 (see definition in Eq. 3), and non-white noise corresponding to both the baseline and goal noise models described in Sec. 2.2. For all simulations using the SO small-aperture window function, the homogeneous noise realizations are scaled by the local $1/\sqrt{N_{\text{hits}}}$ to account for the inhomogeneous coverage. In all cases we explore the impact of the additional apodization required by the pure- B C_ℓ estimator (Smith 2006) for different choices of apodization scale. In particular, we use the C^2 apodization scheme described in Grain et al. (2009) with 5° , 10° , and 20° apodization scales. For each combination of A_{lens} , noise level, window function and apodization we estimate the associated uncertainty in the B -mode power spectrum as the scatter of the estimated power spectrum in the 1000 realizations.

The results are shown in Fig. 9: in all cases we find that, within the range of multipoles relevant to the SO SATs ($30 \lesssim \ell \lesssim 300$), the uncertainties associated with our fiducial window function are equal or smaller than the uncertainties corresponding to the compact mask, regardless of the apodization scale, and that the apodization scale is mostly irrelevant for this fiducial window function. Furthermore, the uncertainties obtained for the fiducial window function are remarkably close to the ‘mode-counting’ error bars $\sigma(C_\ell) = (C_\ell + N_\ell)/\sqrt{(\ell + 1/2)f_{\text{sky}}^{\text{eff}}\Delta\ell}$ (Knox 1995), where C_ℓ and N_ℓ are the signal and noise power spectra, $\Delta\ell$ is the bandpower bin width and $f_{\text{sky}}^{\text{eff}}$ is the effective sky fraction associated with the window function, given by $f_{\text{sky}}^{\text{eff}} = \langle N_{\text{hits}} \rangle^2 / \langle N_{\text{hits}}^2 \rangle$ ¹⁷.

We therefore conclude that, in the absence of foreground systematics, assuming $r = 0$ and given the achievable sensitivity, the sky coverage that results from the scanning strategy and instrumental field-of-view has a sub-dominant effect on the achievable constraints on primordial B -modes for SO. Throughout the rest of this section we use this sky coverage in our simulations to assess the impact of foregrounds.

Before we move on, we should also note that some of the results shown here are specific of the power spectrum estimator used (pseudo- C_ℓ with B -mode purification), and more optimal results could be obtained with brute-force E/B projection or quadratic estimators (e.g., Tegmark and de Oliveira-Costa 2001; Lewis 2003).

¹⁷ Note that this definition of $f_{\text{sky}}^{\text{eff}}$ is appropriate to quantify the variance of the power spectra computed from noise-dominated maps. For the hit counts map shown in Fig. 8, this is $f_{\text{sky}}^{\text{eff}} = 0.19$. For signal-dominated maps this hit counts maps has $f_{\text{sky}}^{\text{eff}} = 0.1$.

¹⁶ <https://github.com/damonge/NaMaster>

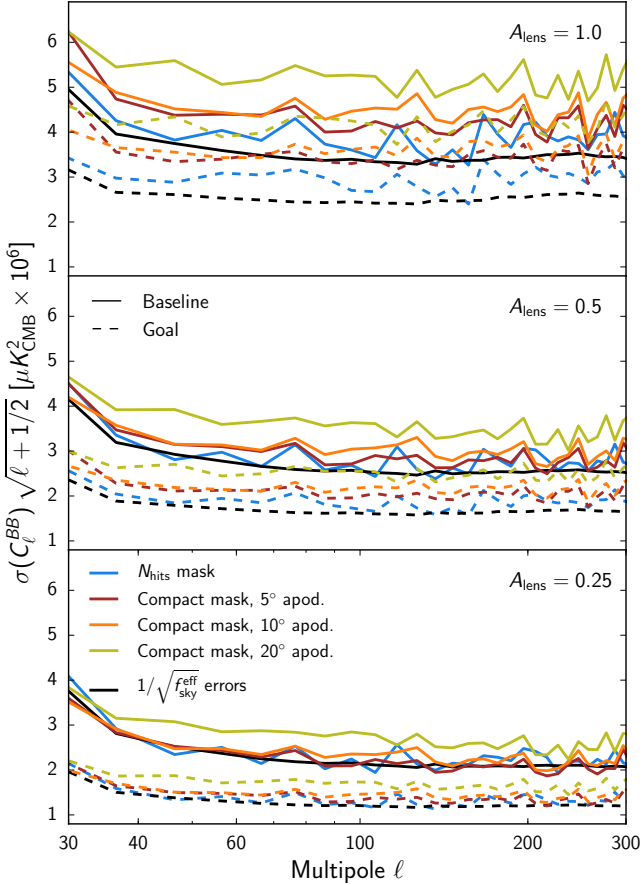


Figure 9. Impact of field of view and scanning strategy on the B -mode power spectrum (C_ℓ^{BB}) uncertainties. The panels show increasing levels of delensing (top to bottom), parametrized by the lensing amplitude A_{lens} , for the SO baseline and goal noise levels described in Table 1. We compare two different sky masks: the fiducial SO footprint in Fig. 8 with $1/N_{\text{hits}}$ weighting and additional 10° tapering, compared to a compact circular mask with the same effective sky area and three different levels of apodization. Errors using the fiducial footprint closely match the mode-counting errors (labeled $1/\sqrt{f_{\text{sky}}^{\text{eff}}}$) achievable with this sky fraction.

3.4.2. Fiducial forecasts for r

We generate forecasts for the different SO instrument configurations described in Sec. 2.2 and shown in Table 1. At the likelihood level, all our calculations assume that the B -mode power spectrum can be described as a sum of two contributions, corresponding to primordial tensor perturbations and lensing B -modes respectively

$$C_\ell^{BB} = r C_\ell^{\text{tensor}} + A_{\text{lens}} C_\ell^{\text{lensing}}, \quad (3)$$

where C_ℓ^{tensor} and C_ℓ^{lensing} are templates for the unlensed, $r = 1$ B -mode power spectrum and the lensed scalar B -mode power spectrum respectively¹⁸. Thus we as-

¹⁸ We assume a scale-invariant spectrum of tensor modes, and define r at the pivot scale $k = 0.005 \text{ Mpc}^{-1}$. Our fiducial cosmology has $A_s = 2.4 \times 10^{-9}$ at that pivot scale, which is $\sim 4\%$ higher than the *Planck* 2018 cosmology (Planck Collaboration 2018d). Our lensing template is $\sim 2\%$ higher at low ℓ than predicted by *Planck* 2018 with power $C_{\ell=100}^{\text{lensing}} = 2.03 \times 10^{-6} \mu\text{K}^2$. We expect these differences in fiducial cosmology to have a smaller impact on our results than other assumptions made here (e.g., on foreground modeling).

sume that the effects of delensing can be encapsulated into a single parameter A_{lens} parametrizing the amplitude of the lensing contribution relative to the expected one without delensing for the fiducial cosmological parameters. In the nominal case we present results for $A_{\text{lens}} = 1$ (no delensing) and $A_{\text{lens}} = 0.5$, corresponding to the delensing efficiency that is expected to be achievable with external maps of the large-scale structure or the CIB (Yu et al. 2017). $A_{\text{lens}} = 0.5$ could also optimistically be achieved by internally delensing with SO data, as described in Sec. 5.

The achievable constraints on the tensor-to-scalar ratio depend, to some extent, on the choice of analysis method.

C_ℓ method: The simplest scenario corresponds to the C_ℓ cross-spectrum approach. These forecasts are shown in Table 4 for the C_ℓ -Fisher method. This optimistic method predicts a sensitivity to primordial B -modes with $\sigma(r) \simeq 1\text{--}2 \times 10^{-3}$, depending on the different noise and delensing assumptions. We run the same pipeline on the 50 simulations and compute the bias and uncertainty on r as its mean and standard deviation over the simulations set (C_ℓ -MCMC of Table 4 and Fig. 10). This case yields similar, although slightly higher values of $\sigma(r)$. However, the simple parametric model assumed by this method, with constant spectral indices across the full footprint (see Fig. 8), gives rise to foreground contamination and an associated bias on r . We find that this bias is of the order of the 1σ error ($\sim 2 \times 10^{-3}$) for our standard foreground configuration, and significantly larger for simulations with more highly-varying synchrotron spectral indices (described in the next subsection).

xForecast, BFoRe and ILC methods: Motivated by these results, we explore more sophisticated, map-based cleaning methods with **xForecast**, **BFoRe** and the ILC pipeline. We analyze the maps in two steps:

1. After foreground cleaning, an estimate of the B -mode power spectrum is obtained from the foreground-cleaned map. This will contain contamination from statistical and systematic foreground residuals.
2. We then marginalize over residual foreground contamination at the likelihood level. To do so, we add a term of the form $A_{\text{FG}}^T C_\ell^{\text{FG}}$ to the model in Eq. 3, where C_ℓ^{FG} is a vector of templates for the expected foreground contamination from different components and A_{FG} is a vector of free amplitudes¹⁹.

The marginalization over foreground residuals at the power spectrum level will reduce the foreground bias at the cost of degrading the final uncertainty on r . We therefore also compare the results before and after this additional marginalization, to provide a rough estimate

¹⁹ **xForecast** uses residual templates built as $C_\ell^{\text{FG}} \equiv \mathbf{W}^T \mathbf{F}_\ell \mathbf{W}$, where \mathbf{W} is the operator projecting sky templates onto frequency maps, and \mathbf{F}_ℓ the matrix containing all frequency cross spectra for that component. The ILC pipeline uses a similar approach, where \mathbf{W} is constructed from the ILC weights. **BFoRe** uses a single template built from the power spectrum of the foreground residual map obtained from the simulations.

Table 4
Forecasts for $r = 0$ model using six different cleaning methods, for fiducial foreground model^a

	Method	SO Baseline		SO Goal	
		pess-1/ f	opt-1/ f	pess-1/ f	opt-1/ f
$A_{\text{lens}} = 1$	C_ℓ -Fisher	$\sigma = 2.4$	$\sigma = 1.9$	$\sigma = 1.7$	$\sigma = 1.5$
	C_ℓ -MCMC	1.9 ± 2.6	2.3 ± 2.3	2.2 ± 2.1	2.4 ± 2.1
	xForecast	1.3 ± 2.7	1.6 ± 2.1	1.4 ± 1.9	1.6 ± 1.6
	xForecast ^b	0.0 ± 4.0	0.0 ± 3.5	0.0 ± 3.3	0.2 ± 2.8
	BFoRe ^b	-0.5 ± 5.8	-0.5 ± 3.6	-0.6 ± 4.3	-0.5 ± 3.4
	ILC ^b	-0.4 ± 3.9	-0.3 ± 3.1	-0.2 ± 3.9	-0.3 ± 3.0
$A_{\text{lens}} = 0.5$	C_ℓ -Fisher	$\sigma = 1.8$	$\sigma = 1.4$	$\sigma = 1.2$	$\sigma = 0.9$
	C_ℓ -MCMC	1.7 ± 2.1	2.2 ± 2.0	2.0 ± 1.7	2.2 ± 1.7
	xForecast	1.3 ± 2.1	1.6 ± 1.5	1.3 ± 1.3	1.5 ± 1.0
	xForecast ^b	0.1 ± 3.2	0.1 ± 2.6	0.0 ± 2.5	0.3 ± 1.8
	BFoRe ^b	-0.2 ± 5.0	-0.4 ± 2.6	-0.6 ± 3.2	-0.5 ± 2.0
	ILC ^b	-0.3 ± 3.0	-0.3 ± 2.4	-0.1 ± 2.8	-0.2 ± 2.3

^a Table gives $(r \pm \sigma(r)) \times 10^3$ for different analysis pipelines (different rows), and different noise configurations (different columns, see Sec. 2.2 for details.). The results for the fiducial lensing and noise combination are highlighted in boldface.

^b In these cases a foreground residual is additionally marginalized over after map-based cleaning.

of the level of foreground contamination in the cleaned maps.

These forecasts are summarized in Table 4. For **xForecast**, the map-based pipeline is able to recover values of $\sigma(r)$ similar to those predicted by the Fisher matrix, although foreground residuals cause a bias at the level of $r = 2 \times 10^{-3}$, or equivalently at the 1σ level.

We show the B -mode power spectrum of these foreground residuals, as computed by **BFoRe**, in Fig. 11, together with the average power spectrum measured from the simulated and foreground-cleaned maps before residual foreground marginalization. The foreground residuals are comparable to a primordial signal with $r = 0.0016$, also shown for reference. We find that the foreground bias can be substantially reduced by the final marginalization over foreground residuals, at the cost of a noticeable increase in the final uncertainties. In this more conservative scenario, our forecasts predict that SO will be able to measure r to the level of $2\text{--}3 \times 10^{-3}$, with the potential to rule out an $r = 0.01$ model at the 3σ level. The statistical error bars on \mathcal{D}_ℓ^{BB} are shown in Fig. 7.

To verify these results, we repeat these forecasts using the more realistic approaches of **BFoRe** and the **ILC** method, that include the effects of E -to- B leakage. The results, after residual foreground marginalization, are also reported in Table 4 and shown in Fig. 10. These results agree well in most cases with the values predicted by **xForecast**. For example we forecast

$$\begin{aligned}
 r &= (+0.1 \pm 2.6) \times 10^{-3} && \text{xForecast,} \\
 r &= (-0.4 \pm 2.6) \times 10^{-3} && \text{BFoRE,} \\
 r &= (-0.3 \pm 2.4) \times 10^{-3} && \text{ILC,}
 \end{aligned} \tag{4}$$

for the baseline noise case, with $A_{\text{lens}} = 0.5$. This agreement of methods increases our confidence in the ability of SO to separate the components to reach this level.

The approach described here of map-based foreground removal, combined with additional residual marginalization in the B -mode spectrum, provides an estimate of the anticipated errors due to foreground uncertainty. In practice, though, we will not know what the foreground residuals look like. We therefore anticipate using other

Table 5
Forecasts exploring departures from the fiducial case^a

Method	Fiducial	$r = 0.01$	2-dust	
			+AME	High-res β_s
C_ℓ -Fisher	$\sigma = 1.4$	$\sigma = 1.8$	$\sigma = 1.4$	$\sigma = 1.4$
C_ℓ -MCMC	2.2 ± 2.0	12 ± 2.3	1.5 ± 1.9	5.3 ± 2.0
xForecast ^b	0.1 ± 2.6	9.9 ± 3.3	0.5 ± 3.1	0.0 ± 2.7
BFoRe ^b	-0.4 ± 2.6	9.5 ± 3.2	-0.3 ± 2.4	-0.4 ± 2.7
ILC ^b	-0.3 ± 2.4	9.7 ± 2.8	-0.3 ± 2.5	-0.5 ± 3.5

^a Table gives $(r \pm \sigma(r)) \times 10^3$ for different analysis pipelines (different rows), and different departures from the fiducial case (an $r = 0.01$ model and two alternative foreground models).

^b Marginalized over foreground residual after cleaning.

strategies to mitigate the impact of foreground residuals. This can be done by increasing the complexity of the foreground model, either fitting for individual spectral parameters over smaller pixels in the sky (Alonso et al. 2017), or using a moment expansion to account for spatial variations of foreground SEDs, both at the map and power-spectrum levels (Chluba et al. 2017).

Another approach would be to avoid the areas of larger foreground contamination. Using the same simulations, but focusing the analysis on the cleanest 5% of the sky, we are able to limit the residual bias to the level of $r < 10^{-4}$ without additional marginalization, at the cost of larger uncertainties ($\sigma(r) = 0.003$ for baseline noise and $A_{\text{lens}} = 0.5$) due to the area loss. Finally, the robustness of any constraints on r will ultimately be verified by exploring the dependence of the measured cosmological signal on different data cuts, both spatial and in frequency.

3.4.3. Departures from the fiducial case

Fixing the instrumental noise properties to the ‘optimistic’ ℓ_{knee} and baseline white noise case, we explore a set of departures from the fiducial scenario: increasing the foreground complexity, exploring the impact of delensing, and testing the impact of varying the low-frequency angular resolution.

Foreground complexity.— Beyond the ‘standard’ foreground simulations used in the previous section, we re-

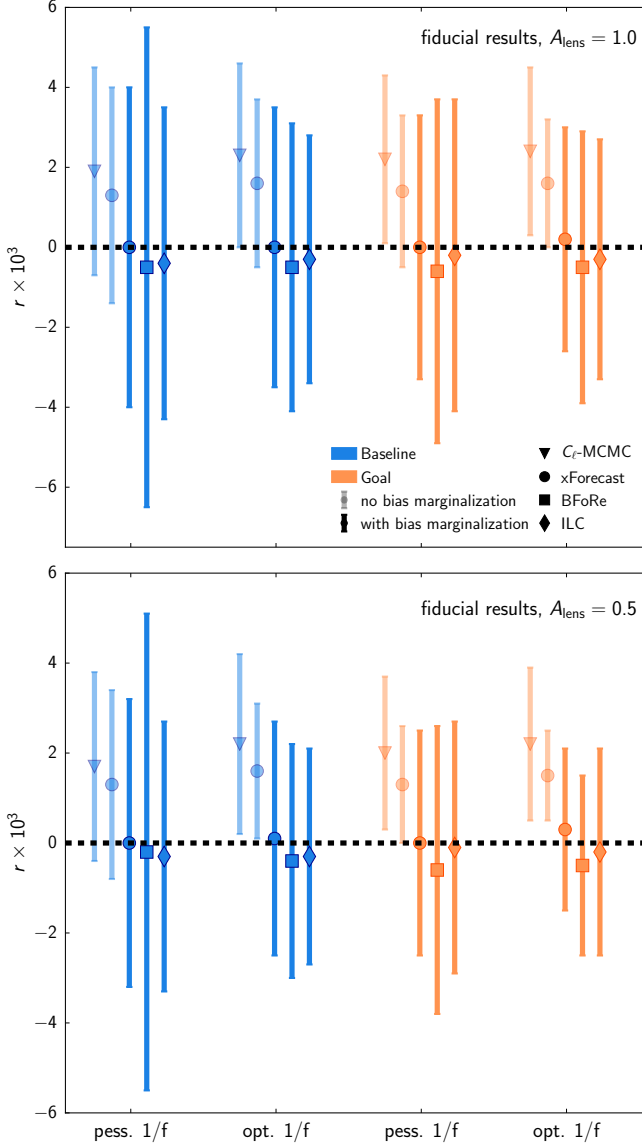


Figure 10. Estimated r and 1σ uncertainties for simulations with $r = 0$ and $A_{\text{lens}} = 1$ (top) and 0.5 (bottom). The fiducial sky model has single dust and synchrotron components with spatially varying spectral indices, described in Sec 2.4.4. We show baseline and goal noise levels, with either pessimistic or optimistic $1/f$ scenarios, for the C_ℓ -MCMC and xForecast methods, without residual marginalization (translucent), and for the xForecast , BFoRe and ILC methods that additionally marginalize over foreground residuals at the power spectrum level (solid).

peat our forecasts using two more complex foreground models (the ‘2 dust + AME’ and ‘High-res. β_s ’ models described in Sec. 2.4.4). The projections for these two cases are reported in Table 5 and shown in Fig. 12. In both cases we observe that, while the more complex models lead to a larger r bias before residual marginalization, particularly in the case of high-resolution β_s , marginalization over residuals mitigates this bias without a significant loss of sensitivity when compared with our fiducial foreground simulations.

Delensing. — Our fiducial forecasts only explore two possible scenarios regarding delensing: no delensing or 50% delensing, achievable with external CIB and large-scale structure data. In the upper panel of Fig. 13 we show

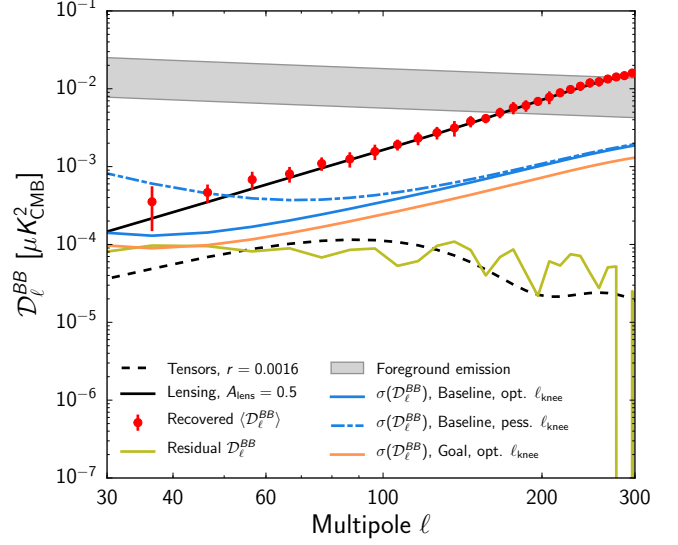


Figure 11. Mean B -mode power spectrum, D_ℓ^{BB} , estimated from simulations using map-level component separation (red) with errors from 100 realizations. The input spectrum (black solid) has $r = 0$ and assumes 50% delensing. The power of the total foreground emission is shown shaded (between 93 GHz, lower, and 145 GHz, upper). Power spectrum uncertainties for $\Delta\ell = 10$ bandpowers are shown (blue, orange) for different SO noise configurations. The contribution of foreground residuals to the recovered D_ℓ^{BB} (yellow) biases the red circles above the input and is comparable to a signal with tensor-to-scalar ratio $r = 0.0016$ (dashed). This bias can be suppressed by marginalizing over the foreground residuals in the likelihood.

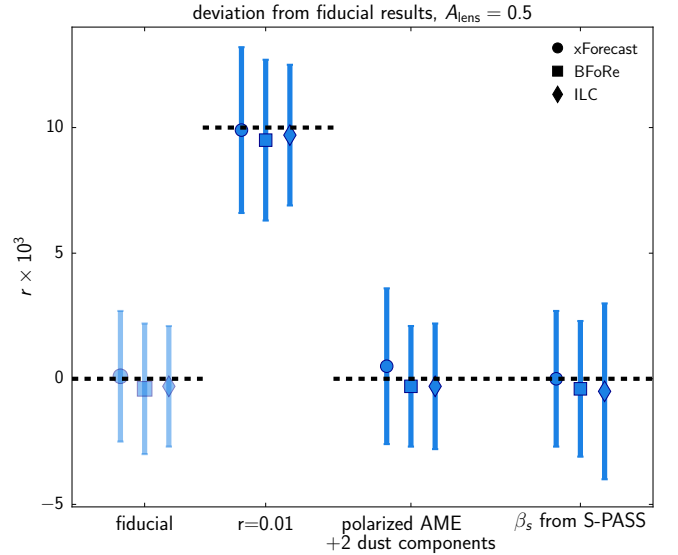


Figure 12. As in Fig. 10, for the cases deviating from the fiducial forecasts. The ‘fiducial’ points match the second panel of Fig. 10 for baseline sensitivity and optimistic $1/f$. The three other cases assume $r = 0.01$ in the input sky simulations (left), $r = 0.0$ with 2 dust components and polarized AME (middle), and $r = 0.0$ with synchrotron scaling based on a high-resolution β_s template (right). These models are described in Sec. 2.4.4 with forecasts in Table 5.

how $\sigma(r)$ is expected to improve as a function of the lensing amplitude A_{lens} . We find that the expected reduction of $\sigma(r)$ in lowering A_{lens} below 0.5 is not substantial for the SO noise levels considered here. Since $A_{\text{lens}} = 0.5$ is expected to be achievable using external tracers of the lensing potential, we do not find strong motivation to

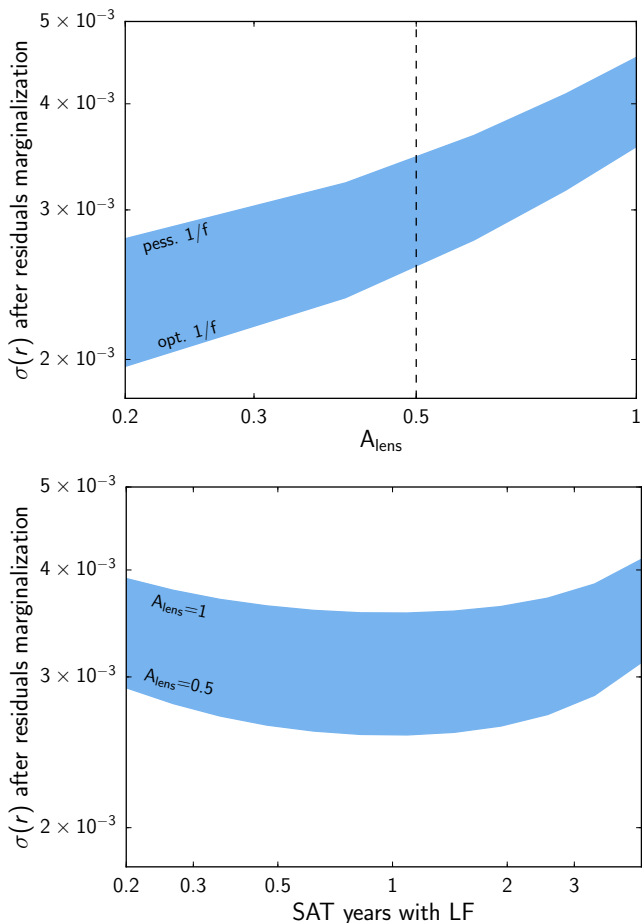


Figure 13. *Top:* forecast $\sigma(r)$ as a function of the residual lensing amplitude A_{lens} , for an $r = 0$ signal. The band corresponds to SO baseline between the optimistic and pessimistic $1/f$ noise models. We expect $A_{\text{lens}} = 0.5$ from external delensing and 0.7 from internal delensing (this assumes the LAT covers $f_{\text{sky}} = 0.4$; focusing all of the LAT time on the $f_{\text{sky}} = 0.1$ SAT region would give $A_{\text{lens}} = 0.5$ from internal delensing – not a significant gain). *Bottom:* forecast $\sigma(r)$ as a function of the time devoted to low-frequency (LF) observations, at the expense of the mid-frequency channels. The band corresponds to $0.5 \leq A_{\text{lens}} \leq 1.0$. We find one year of LF observations to be optimal.

optimize the LAT survey for internal iterative delensing (described in Sec. 5).

Specifically, we find that if we were to focus all of the LAT survey time on the 10% of sky overlapping with the SATs, we could achieve $A_{\text{lens}} = 0.52$ (0.42) for baseline (goal) noise level from internal delensing. This would give a negligible improvement in $\sigma(r)$ compared to the $A_{\text{lens}} = 0.5$ achievable from external delensing. Our nominal case, with the LAT surveying $f_{\text{sky}} = 0.4$, projects $A_{\text{lens}} = 0.71$ (0.62). This is comparable to external delensing levels, and will provide a useful cross-check. Furthermore, the projected SO measurement of r is not strongly lensing-limited. With no delensing, we project that errors would increase from $\sigma(r) = 0.0026$ to 0.0035 for the xForecast method; this is non-negligible but, in practice, systematic and foreground effects are likely to be at least as impactful.

Our choice to keep the LAT survey as wide as possible was therefore simple, because the degradation in $\sigma(r)$ from a wide $f_{\text{sky}} = 0.4$ LAT survey, compared to a deeper $f_{\text{sky}} = 0.1$ LAT survey, appears negligible, and all of the

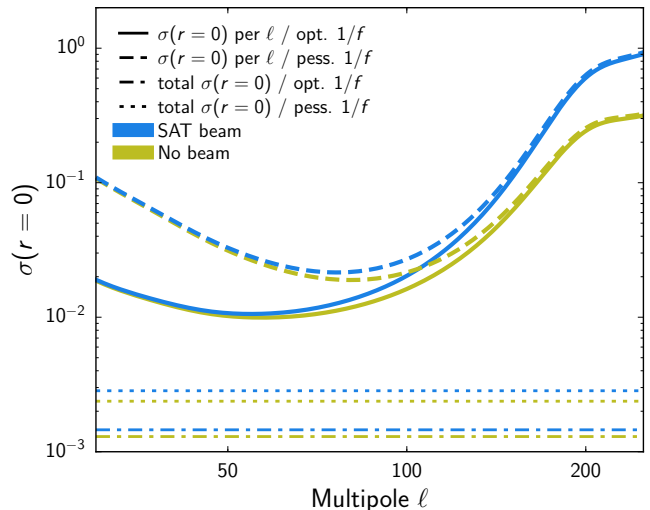


Figure 14. Contribution to the total error on the tensor-to-scalar ratio r for each multipole ℓ ($r = 0$ is used as fiducial). Results are shown assuming baseline noise levels for an instrument with the fiducial SAT resolution (blue) and for infinite resolution (light green), and for optimistic (solid) and pessimistic (dashed) $1/f$ noise. The horizontal dot-dashed and dotted lines show the final $\sigma(r)$ obtained by combining all multipoles for the optimistic and pessimistic $1/f$ noise cases, respectively. The finite resolution of the SATs, including the LF bands, does not impact the projections for our nominal modeling assumptions. These results were derived using power spectrum errors obtained from BFore after component separation, accounting for inhomogeneous noise coverage and E/B leakage, and assuming $A_{\text{lens}} = 0.5$. The curves assume an optimal combination of sensitivity from the SATs and the LAT.

other SO science cases benefit from surveying more sky with the LAT. Of course, this conclusion depends on the SO noise levels and the SAT survey area. If we were to improve the noise levels significantly, or reduce the SAT survey area significantly, these conclusions would change, and would be relevant for future survey design with SO or future telescopes. The impact of delensing is further discussed in Sec. 5.1.

LF sensitivity and resolution.— The bottom panel of Fig. 13 shows how $\sigma(r)$ depend on the observation time for the low-frequency channels (27 and 39 GHz), at the expense of the mid-frequency channels (93 and 145 GHz, see description in Sec. 2.1), after component separation. We find a broad optimal duration around $T_{\text{LF}} = 1$ year, which has been used as the default in the results presented so far.

Figure 14 shows the impact of the SATs’ finite resolution on the achievable constraints. Since most of the constraining power on r is concentrated on angular scales $\ell \leq 100 - 150$, for angular resolutions $\leq 90'$, the constraints are mainly driven by scales larger than the beam FWHM. Thus, for SO, the relatively low resolution of the SATs does not appear to limit the instrument’s performance, including the ability of the low-frequency channels to map the synchrotron emission.

3.5. Limitations of current forecasts

Although we have attempted to produce realistic forecasts in terms of foreground complexity and other technical sources of uncertainty, such as E/B leakage, one of the main shortcomings of these forecasts has to do with the impact of instrumental systematics. Imperfect

knowledge of the instrument bandpasses, relative gains, polarization angle, ground pickup, half-wave plate imperfections, crosstalk, etc. are challenges to achieve the promised performance of these next generation CMB polarization observatories. Although many mitigation solutions, based on both hardware and software, are currently designed and tested on real data, developing these methods in the context of high-sensitivity experiments will be critical for the success of SO. As an example of this, in the context of bandpass and relative gain calibration, it is shown in [Ward et al. \(2018\)](#) that post-calibration knowledge of bandpass shifts and relative gains at the percent level may be necessary in order to reduce instrumental systematics below the statistical uncertainties, unless the bandpass uncertainties can be successfully self-calibrated at the likelihood level. An assessment of systematic effects is now the subject of a new SO study. Future forecasts will also need to account for the effects of filtering in a realistic way, since this can be one of the major challenges for B -mode power spectrum analyses ([BICEP2/Keck and Planck Collaborations 2015](#)).

Our forecasts have also not assessed the possible benefit of combining the SO observations with external datasets in terms of characterizing the dust and synchrotron SEDs. At high frequencies, and particularly on large angular scales, *Planck*'s 353 GHz map will help in constraining the spatial variation of β_d and setting tighter priors on T_d . At low frequencies, observations from C-BASS ([Jones et al. 2018](#)), S-PASS ([Krachmalnicoff et al. 2018](#)) and QUIJOTE ([Poidevin et al. 2018](#)) will help constrain the spatial variation of β_s as well as set upper bounds on the non-zero synchrotron curvature or the presence of polarized AME. Our forecasts have also neglected the possible spatial variation of the synchrotron curvature, which could be informed by these experiments. Future forecasts and analysis pipelines will take this into account.

4. SMALL-SCALE DAMPING TAIL

At small angular scales, the main SO science targets are the number of relativistic species in the early universe, the spectrum of primordial perturbations, the expansion rate of the universe, the masses of neutrinos, the abundances of primordial elements, and the particle nature of dark matter and its interactions. These phenomena affect the damping tail (high- ℓ region) of the CMB power spectra in temperature and polarization, as well as the growth of structure revealed by CMB lensing. In this section we describe our methodology, present forecasts for N_{eff} (Sec. 4.1), for the primordial scalar power (Sec. 4.2), the Hubble constant (Sec. 4.3), and additional high- ℓ science parameters (Sec. 4.4).

We use the effective number of relativistic species, N_{eff} , as our main proxy for the information encoded in the CMB at small scales, and use it to investigate the SO experimental requirements (the CMB-S4 science book followed a similar approach; [Abazajian et al. 2016](#)). The N_{eff} parameter tracks the qualitative effect of early universe physics on the CMB, and also has precise theoretical predictions. In this section we then report forecast for N_{eff} and how these are affected by the LAT survey specifications, and also report projections for other SO high- ℓ science targets.

We forecast the science performance with a Fisher matrix based on SO noise levels, with details described in Sec. 2. We explore the experimental parameter space (including resolution, sensitivity, observed sky fraction) and systematic and contaminating effects (including beam errors, atmospheric noise, and polarized source contamination). Our observables are the lensed TT, TE, EE power spectra and the lensing convergence power spectrum, $\kappa\kappa$. We include lensing-induced covariances ([Benoit-Lévy et al. 2012](#)). To mitigate residual foreground contamination (dominating in temperature and leaking to lensing at $\ell \sim 3000$), we retain only the angular scales in the range $30 \leq \ell \leq 3000$ for TT and $\kappa\kappa$, while we use the full range of CMB scales, $30 \leq \ell \leq 5000$, for the cleaner TE and EE correlations. We impose Big Bang Nucleosynthesis (BBN) consistency relations ([Pisanti et al. 2008](#)) on the Helium abundance, Y_p , by assuming the value N_{eff} was the same during BBN and recombination. In all cases we combine SO data with *Planck* as described in Sec. 2.6.

We simplify all the damping tail forecasts in this section by assuming perfect foreground removal from the power spectra and a single, co-added noise level for the LAT. For this we use the CMB temperature and CMB polarization Deproj-0 N_{ℓ}^{TT} and N_{ℓ}^{EE} described in Sec. 2.5, and the minimum-variance noise curves for $\kappa\kappa$. For a further suite of tests on individual components of the noise, including the atmosphere or point source terms, and tests of the foreground cleaning, we co-add the 93 GHz and 145 GHz white noise levels²⁰ in Table 1. We demonstrate the validity of these assumptions in Sec. 4.1.2.

4.1. Forecasts for N_{eff}

At its baseline sensitivity, SO will be sensitive to well-motivated, non-standard scenarios for relativistic species in the early universe. The usual parametrization of the neutrino contribution to radiation density at early times is (see, e.g., [Kolb and Turner 1990](#))

$$\rho_{\text{rad}} = \left[1 + \frac{7}{8} \left(\frac{4}{11} \right)^{\frac{4}{3}} N_{\text{eff}} \right] \rho_{\gamma}, \quad (5)$$

where ρ_{γ} is the CMB photon energy density, and N_{eff} is the effective number of relativistic species. The Standard Model of particle physics predictions for N_{eff} is 3.046, assuming standard electroweak interactions, three active light neutrinos, small effects from the non-instantaneous neutrino decoupling from the primordial photon-baryon plasma, and corrections due to energy-dependent neutrino interactions ([Dolgov et al. 1997, 1999; Mangano et al. 2002; de Salas and Pastor 2016](#)). Via its impact on the expansion rate, primordial element abundances, and radiation perturbations, N_{eff} affects the damping and the position of the acoustic peaks in the temperature, E -mode of polarization, and TE power spectra (see, e.g., [Bashinsky and Seljak 2004; Hou et al. 2013; Abazajian et al. 2015](#)).

For the nominal SO LAT survey covering 40% of the

²⁰ We checked that using the full range of LAT frequencies does not improve on the 93 and 145 GHz co-added signal.

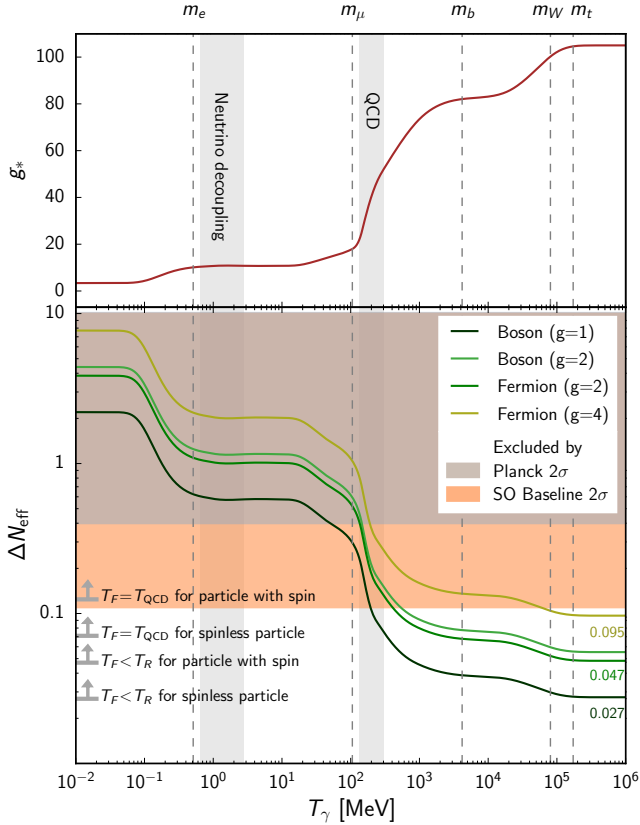


Figure 15. Theoretical targets for N_{eff} , assuming the existence of an additional Beyond-the-Standard-Model relativistic particle that was in thermal equilibrium with the Standard Model at temperatures $T > T_{F=\text{freeze-out}}$. *Top*: evolution of the effective degrees of freedom for Standard Model particle density, g_* , as a function of photon temperature in the early universe, T_γ . Vertical bands show the approximate temperature of neutrino decoupling and the QCD phase transition, and dashed vertical lines denote some mass scales at which corresponding particles annihilate with their antiparticles, reducing g_* . The solid line shows the fit of [Borsanyi et al. \(2016\)](#) plus standard evolution at $T_\gamma < 1$ MeV. *Bottom*: expected ΔN_{eff} today for species decoupling from thermal equilibrium as a function of the decoupling temperature, where lines show the prediction from the [Borsanyi et al. \(2016\)](#) fit assuming a single scalar boson with $g = 1$ (dark green), bosons with $g = 2$ (e.g., a gauge vector boson, light green), a Weyl fermion with $g = 2$ (green), or fermions with $g = 4$ (yellow). Shaded regions show the exclusion regions for *Planck* and SO (baseline). Arrows on the left show the lower limits for specific cases, for example any particle with spin that decoupled after the start of the QCD phase transition would typically be measurable by SO at 2σ . The lower two arrows and corresponding numbers on the right give lower bounds for particles produced any time after reheating (at T_R).

sky, our Fisher forecast yields errors:

$$\begin{aligned} \sigma(N_{\text{eff}}) &= 0.055 && \text{SO Baseline,} \\ \sigma(N_{\text{eff}}) &= 0.050 && \text{SO Goal.} \end{aligned} \quad (6)$$

The current limit from *Planck* is $\sigma(N_{\text{eff}}) = 0.19$ (TT,TE,EE+lowE+lensing, [Planck Collaboration 2018d](#)).

Figure 15 compares the SO baseline sensitivity to interesting science targets for new particles that were at some point in thermal equilibrium with Standard Model particles and then decoupled. The predicted N_{eff} depends on the number and spin of the particles which decouple (determining the degrees of freedom, g , of the new particles), and effective degrees of freedom for en-

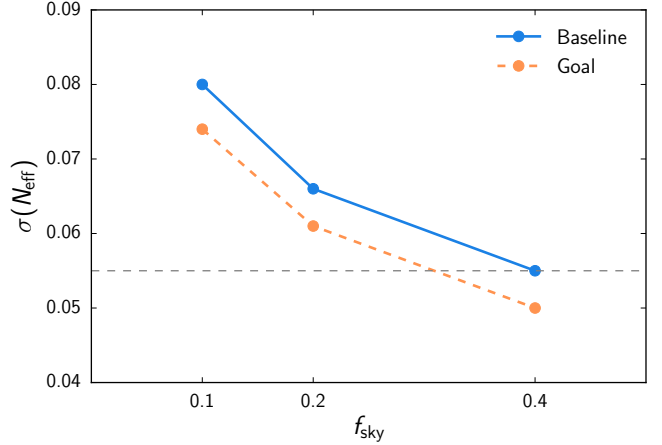


Figure 16. Dependence of the forecast $\sigma(N_{\text{eff}})$ on the fractional sky coverage for SO baseline and goal scenarios. The measurement degrades by 40% when reducing $f_{\text{sky}} = 0.4$ to $f_{\text{sky}} = 0.1$. The dashed gray line gives a reference for the baseline forecast.

tropy g_s , or equivalently the effective degrees of freedom for density g_* , of the Standard Model plasma at the time of decoupling.

A single particle with spin 1/2 that decouples just before or after the QCD phase transition contributes $\Delta N_{\text{eff}} \geq 0.12$, and a similar particle with spin 1 contributes $\Delta N_{\text{eff}} \geq 0.14$; these cases should be measurable at the 2σ significance level for SO. Models predict deviations at $\Delta N_{\text{eff}} \geq 0.047$ for additional light particles of spin 1/2, 1 and/or 3/2 that were in thermal equilibrium with the particles of the Standard Model at any point back to the time of reheating (see, e.g., [Brust et al. 2013](#); [Chacko et al. 2015](#); [Baumann et al. 2016b](#)); these could be measurable by SO if multiple species are involved. Four or more scalar bosons would also be measurable at 2σ significance by SO, as would various scenarios involving multiple non-thermal axions if they contribute sufficiently to the energy density.

In the following we assess how the forecasts for N_{eff} depend on survey strategy, foreground residuals, and instrument beams. These studies were used in practice to guide the nominal choice of the SO experimental specifications.

4.1.1. Survey requirements

Although different experimental configurations can trade sensitivity, resolution and observed sky area to achieve the same errors for N_{eff} , the errors depend most strongly on sky area. We show the dependence on survey and instrument design in Figs. 16 and 17.

Sky area— At fixed-cost effort, and for maps with temperature noise exceeding $4 \mu\text{K-arcmin}$, damping tail science depends strongly on f_{sky} . In particular, $f_{\text{sky}} \geq 0.4$ is needed to reach $\sigma(N_{\text{eff}}) \leq 0.06$, as shown in Fig. 16. The N_{eff} constraint worsens for smaller sky coverage, with a 40% degradation going from $f_{\text{sky}} = 0.4$ to $f_{\text{sky}} = 0.1$. This is also visible in the two scenarios shown in Fig. 17, where the amplitude of the likelihood surface increases for lower f_{sky} (right hand side).

Resolution— The uncertainty in N_{eff} does not improve significantly with resolution finer than $2'-3'$ if other specifications are held fixed (see Fig. 17).

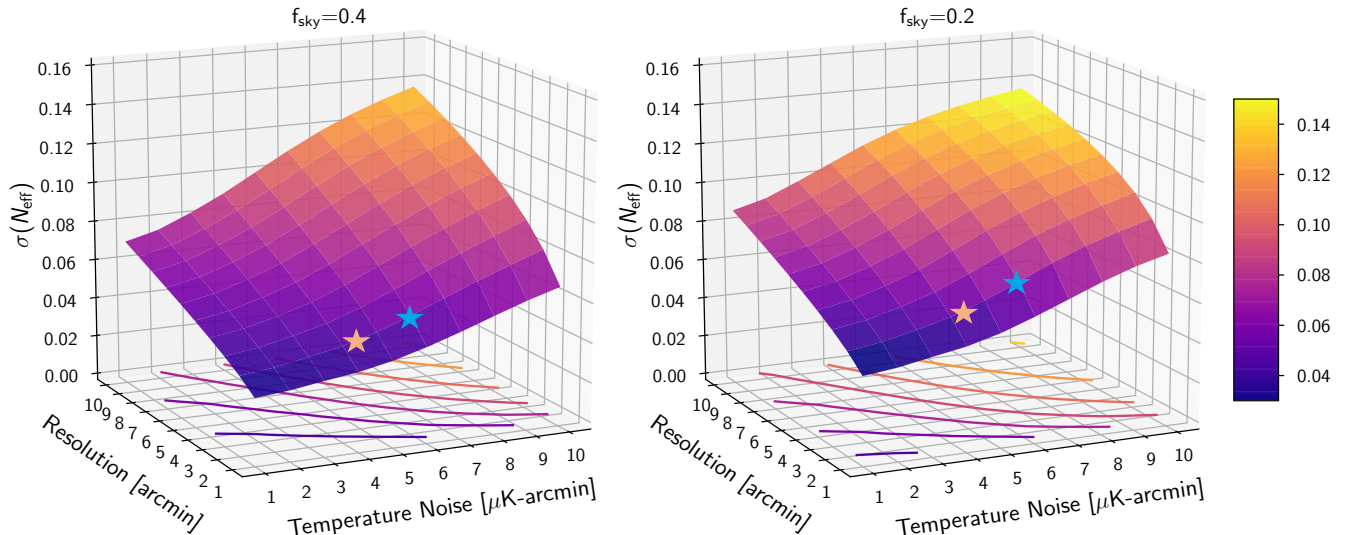


Figure 17. Dependence of the N_{eff} estimate on resolution, sensitivity and sky coverage (with wide coverage shown on the left and a smaller, deeper survey on the right). In order to reach the science target of $\sigma(N_{\text{eff}}) = 0.06$, a reduced noise of $5 \mu\text{K}\text{-arcmin}$ on 40% of the sky and resolution $< 3'$ at 145 GHz are needed. Stars show the expected SO measurements in the case of goal (orange) and baseline (blue) configurations.

Sensitivity— Assuming a wide survey ($f_{\text{sky}} = 0.4$) and resolution better than $3'$ at 145 GHz, a white noise level of $5 \mu\text{K}\text{-arcmin}$ is needed to reach $\sigma(N_{\text{eff}}) = 0.06$ (see Fig. 17).

Frequency coverage— In the next subsection we show that cosmological parameters from the damping tail are not strongly reliant on having broad frequency coverage to mitigate foreground contamination.

4.1.2. Testing foreground contamination

We find that foreground contamination, at the level that exists in our simulations, has little impact on these forecasts. At the SO level of sensitivity and resolution (and for all beyond-Stage-3 CMB experiments), we expect polarization observations to dominate cosmological constraints (see, e.g., Galli et al. 2014; Calabrese et al. 2017). At small scales, this comes with the advantage of reducing the impact of foreground contaminants. In the damping tail, the TT power spectrum is more contaminated by Galactic and extragalactic foreground emission than the TE and EE spectra, which are mainly affected by residual power in unresolved radio sources. However, the shape of the power spectrum for radio source emission is well known and therefore easy to separate from the CMB. Polarized thermal dust and synchrotron emission from the Galaxy, in our current simulations and after masking, have a negligible impact on these small angular scales.

All our forecasts for parameters derived from the damping tail therefore assume that the LAT information has been compressed in a single channel, co-adding the foreground-marginalized noise curves of Sec. 2.5 and without retaining multi-frequency information. To demonstrate the validity of this assumption, we perform a full multi-frequency power spectrum analysis, running simulations to test the impact on the N_{eff} constraints of

marginalizing over Galactic and extragalactic emission in TT , TE and EE .

We do not use the map-based simulations described in Sec. 2, but instead simulate LAT multi-frequency spectra with a model for the sky. The lensed CMB signal is added to the following foreground components: (i) emission in temperature from the tSZ and kSZ effects; Poisson-like and clustered dusty star-forming galaxies for the CIB; radio galaxies; a cross-correlation term between the clustered component of the CIB and the thermal SZ; thermal dust emission from the Galaxy; and (ii) emission in polarization from unresolved Poisson sources. The modeling follows methods used for ACT, SPT, and *Planck* analyses (Dunkley et al. 2013; Reichardt et al. 2012; George et al. 2015; Planck Collaboration 2016d, 2014a), and is consistent with the map-based modeling used in Sec. 2.5. We implement the temperature model described in Dunkley et al. (2013), and include polarized radio sources at the level measured in Louis et al. (2017). The level of foregrounds present in the simulated data has the following \mathcal{D}_ℓ power at $\ell = 3000$ at 150 GHz: 4 and $2 \mu\text{K}^2$ for the tSZ and kSZ components; 7, 3 and $6 \mu\text{K}^2$ for CIB-Poisson, radio, and CIB-clustered sources; a 10% correlation between the tSZ and CIB clustered component; $0.5 \mu\text{K}^2$ of Galactic dust emission; $1 \mu\text{K}^2$ for radio sources in EE (this is based on a very conservative upper level, as no polarized sources were masked in the analysis of Louis et al. 2017), and no emission in TE (consistently with what was found in Louis et al. 2017). We model the SO LAT noise following the white-noise levels and atmospheric contributions described in Sec. 2.

The simulations are used to form a multi-frequency likelihood and processed in two steps: first, the foreground power is marginalized over and the uncertainty due to foreground marginalization is propagated to marginalized CMB bandpowers. Second, parameter estimation is then carried out from the marginalized CMB

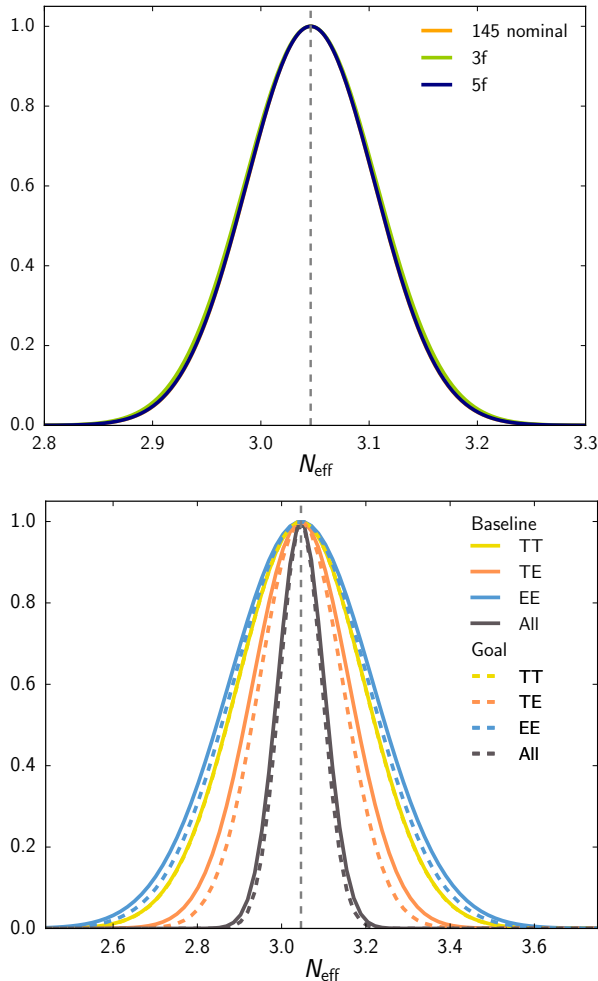


Figure 18. *Top:* Impact of foreground cleaning the LAT using 5 (blue) or 3 (green) frequencies on the N_{eff} estimate. The 145 nominal orange curve shows the result assuming the ideal case of having no foregrounds in the data. The gain from retaining frequency information is completely negligible. *Bottom:* Constraints on N_{eff} from individual small-scale spectra (TT , TE , EE) and the total, shown for baseline (solid) and goal (dashed) scenarios. The most constraining channel is the foreground-clean TE spectrum.

bandpowers using standard MCMC techniques. The results are shown in the top panel of Fig. 18: when using 5 frequencies (39, 93, 145, 225, 280) to marginalize over the foregrounds present in the LAT data we recover the nominal foreground-free estimate, and with 3 frequencies (93, 145, 225) the degradation in the N_{eff} estimate is negligible.

We find that component separation has a relatively small impact on damping-tail forecasts because, at the noise level and resolution of SO, constraints on N_{eff} are mainly driven by the $TE+EE$ constraining power, as shown in the bottom panel of Fig. 18. We also find that *Planck* TT data at $\ell < 1500$ could be used in place of SO TT information, and still achieve the full constraining power of SO without needing to model and clean the SO TT spectrum. Of course, since we have not included Galactic contamination in the TE and EE statistics in these simulations, and we included only EE point source power described by a Poisson term, it is unsurprising that we find no impact of foregrounds on the forecast constraints from TE and EE . Future studies will be

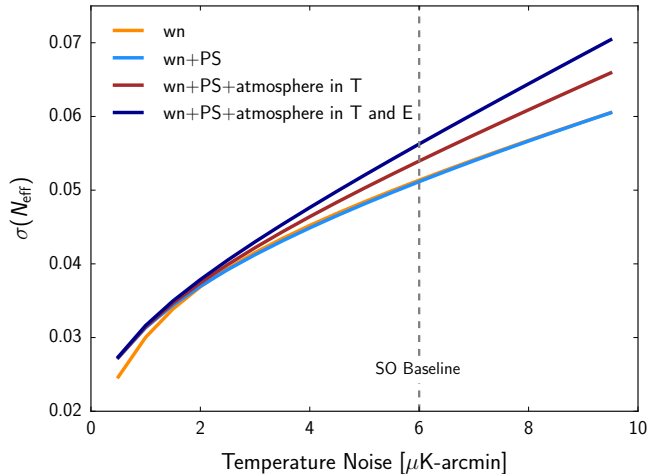


Figure 19. Impact of atmospheric and point source (PS) noise contamination on N_{eff} forecasts. For temperature noise (white noise levels, wn) above $1.5 \mu\text{K-arcmin}$, the dominant effect is the atmosphere. This is due to the increase in the temperature noise at $\ell < 3000$. *Planck* data on the same SO sky coverage are included to minimize the impact of the atmosphere as much as possible. The SO baseline noise case is highlighted with a dashed vertical line.

useful to validate these assumptions.

4.1.3. Impact of point source and atmospheric noise

In addition to component separation, atmospheric noise and noise from polarized point sources can both impact the forecast constraints²¹. In our nominal forecasts, we include atmospheric noise as described in Sec. 2. This effectively increases the noise levels above the white noise level on scales $\ell < \ell_{\text{knee}}$. For temperature noise, $\ell_{\text{knee}}^{TT} \approx 3000$ and so this can be an important effect for TT and TE . Some of this impact is mitigated by adding *Planck* data to minimize N_{ℓ}^{TT} at large scales, as described in Sec. 2.

We test the impact of atmospheric noise on the N_{eff} forecasts by removing the atmospheric noise component, as shown in Fig. 19. For the combined *Planck* and SO surveys, it shows that the atmospheric contribution to N_{ℓ}^{TT} has a small impact on the N_{eff} forecasts. The SO baseline temperature noise level is $6 \mu\text{K-arcmin}$ co-added over 93 and 145 GHz, so the effect of removing atmospheric noise would be to reduce the N_{eff} error by ≈ 0.005 . For EE , atmospheric noise impacts scales at $\ell < 700$, which play an important role in breaking degeneracies with other cosmological parameters (and in particular n_s). We find that the atmospheric contribution to N_{ℓ}^{EE} impacts N_{eff} forecasts at the same level as temperature, as shown in Fig. 19, even though $\ell_{\text{knee}}^{TT} \gg \ell_{\text{knee}}^{EE}$. This reflects the role the *Planck* data play in N_{ℓ}^{TT} .

Unresolved polarized emission is expected from extragalactic radio sources as shown in Tucci et al. (2004); Battye et al. (2010); Tucci and Toffolatti (2012); Puglisi et al. (2017) and discussed in detail in Sec. 8. This emission effectively contributes as an additional source of noise for small-scale polarization data. The point source (PS) power enters D_{ℓ}^{TT} and D_{ℓ}^{EE} with a white spectrum, characterized by a single amplitude parameter at a pivot

²¹ Here we study the impact of point sources as an additional source of small-scale noise, rather than as a foreground contaminant.

scale, $D_\ell = A(\ell/\ell_0)^2$. We study the impact of this additional noise term by including power at 150 GHz from point sources with an amplitude of

$$\begin{aligned} D_{\text{PS},\ell=3000}^{TT} &= 6 \mu\text{K}^2, \\ D_{\text{PS},\ell=3000}^{EE} &= (3 \times 10^{-3}) \times 6 \mu\text{K}^2. \end{aligned} \quad (7)$$

These values are based on *Planck*, ACT, and SPT measurements of dusty and radio emission in temperature and on the measured polarization fraction of the point sources (Dunkley et al. 2011; Planck Collaboration 2014b; George et al. 2015). Here we assume that all dusty-star-forming and radio sources present in temperature are polarized, but in practice, at frequencies below 150 GHz, we expect only polarized radio sources to contribute to the signal, as described in Sec. 8.

A more realistic estimate of the polarized source level comes from Puglisi et al. (2017), who combine state-of-the-art catalogs of polarized radio sources at frequencies ranging from 1.4 to 217 GHz, to derive the statistical properties of fractional polarization, $\Pi = P/S$. They find $\langle \Pi^2 \rangle$ to have a roughly constant value, 2.5×10^{-3} . The amplitude of D_{PS}^{EE} depends on the differential number counts expected at a given frequency, the detection flux, commonly set at 5σ the sensitivity flux, and the average fractional polarization of radio sources. We use these results to estimate $D_{\text{PS},\ell=3000}^{EE} = 0.015 \mu\text{K}^2$ for SO, consistent with the value considered above.

Even with the over-estimate of the *EE* point source power assumed in Eq. 7, the contribution from *EE* point sources would have to be two orders of magnitude larger to meaningfully impact the forecasts. This is illustrated in Fig. 19, which shows no significant impact of *EE* point sources on the SO N_{eff} forecasts.

4.1.4. Beam requirements

High- ℓ science goals can be adversely affected by beam imperfections, as the beam alters the shape of the observed power spectrum. We can recover the primordial power spectrum by measuring and removing the effect of the beam, but marginalizing over uncertainties in this calibration can potentially weaken the constraining power for cosmology. In addition, a bias in the beam calibration can also bias the cosmological parameters.

The observed C_ℓ^{obs} is a product of the beam shape, B_ℓ , times the true power spectrum, C_ℓ , or $C_\ell^{\text{obs}} = B_\ell^2 C_\ell$. For a Gaussian beam, $B_\ell \approx \exp(-\ell(\ell+1)\theta_{\text{FWHM}}^2/8 \log 2)$. The primordial spectra at high ℓ are similarly damped due to diffusion, $C_\ell \propto e^{-\ell^2/\ell_d^2}$; high- ℓ parameters like N_{eff} and Y_p alter the amount of damping and are measured primarily through effects on ℓ_d . In the observed spectra, a change to θ_{FWHM}^2 is indistinguishable from a change to ℓ_d . Of course, beam calibration allows us to distinguish these two effects but only if the uncertainty in the beam shape is smaller than cosmic variance on the scales of interest.

It is conventional to decompose B_ℓ into eigenmodes that diagonalize the beam covariance matrix. To model the calibration uncertainty, we use the ACT temperature²² beam eigenmodes from Hasselfield et al. (2013a)

²² For the purpose of this analysis we assume that beams are equal in temperature and polarization.

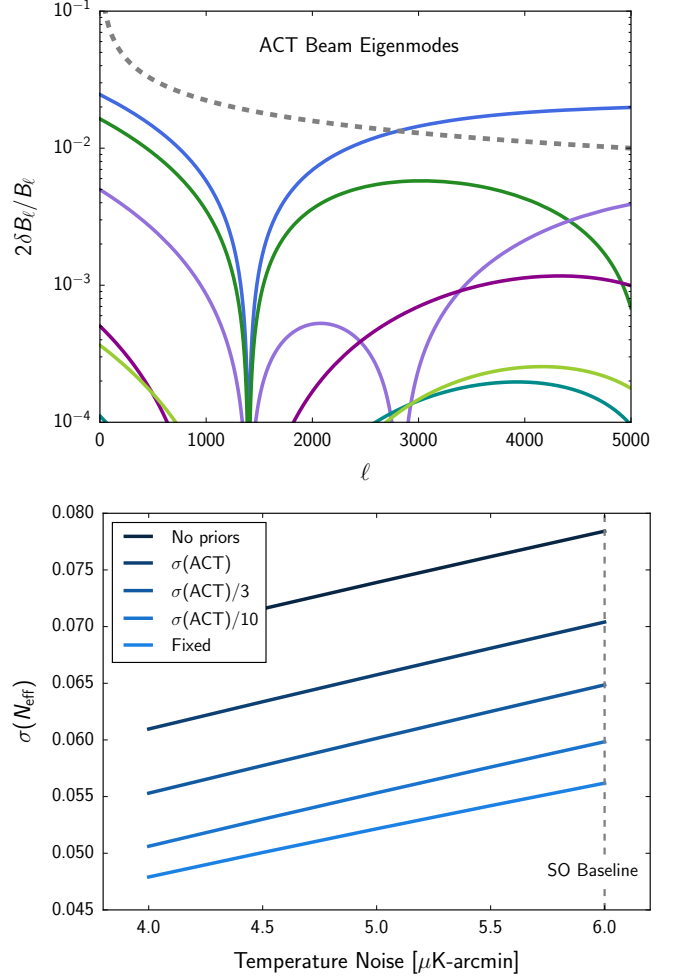


Figure 20. *Top:* The first five ACT beam eigenmodes described in Eq. 8 (solid colored lines) compared to the cosmic variance term (gray dashed line). Each eigenmode is normalized to have unit variance with ACT calibration. *Bottom:* N_{eff} forecasts for different assumptions in the beam calibration uncertainty, ranging from no marginalization (‘Fixed’, lower light-blue line) to marginalization without any prior (‘No priors’, top dark blue line). The SO baseline noise case is highlighted with a dashed vertical line.

and project out the average B_ℓ such that

$$C_\ell^{\text{eff}} = \left(1 + \sum_{i=1}^5 b_i \frac{\delta B_\ell^{(i)}}{B_\ell} \right)^2 C_\ell, \quad (8)$$

where $\delta B_\ell^{(i)}$ are the beam eigenmodes shown in the top panel of Fig. 20. The eigenmodes are normalized such that the coefficients b_i have unit variance for the calibration achieved by ACT. The beam factor multiplying C_ℓ is also compared to the cosmic variance term, $1/\sqrt{2\ell+1}$, shown with a gray dashed line. This highlights that the uncertainty in the power spectrum due to the variance of the largest beam eigenmode is larger than cosmic variance for $\ell > 2500$ and therefore degrades the measurement of N_{eff} . A quantitative estimate of this degradation is obtained by marginalizing over the amplitudes of each mode, b_i , assuming a mean of $b_i = 0$. In this normalization, $\sigma(b_i) = 1$ corresponds to the size of beam errors from ACT in temperature.

The resulting N_{eff} forecasts are shown in the bottom panel of Fig. 20 for choices of prior on b_i with vari-

ances of $\sigma(b_i) = 0, 1/10, 1/3, 1, \infty$. (In the figure, these correspond to a perfect beam with no error (‘Fixed’), $\sigma(\text{ACT})/10$, $\sigma(\text{ACT})/3$, $\sigma(\text{ACT})$ and ‘No priors’.) We see that $\sigma(b_i) < 1/3$ is needed to avoid inflating the errors, and thus would require significant improvements over current ACT beam calibration. From the normalization of the eigenmodes in Fig. 20, this corresponds to sub-percent calibration of the beam shape. However, as will be described in Sec. 9, we allow for a systematic error inflation term in our baseline science forecasts, that could include this beam uncertainty and other effects, and will be the subject of future SO studies.

4.2. Primordial scalar power

SO will make substantial improvements to our knowledge of the primordial density perturbations. The standard approach is to model their power spectrum with a power law with the scalar spectral index n_s and an amplitude of perturbations A_s as $\mathcal{P}(k) = A_s (k/k_*)^{n_s-1}$. The power $\mathcal{P}(k)$ is then mapped onto the angular power spectrum C_ℓ through the transfer function.

Deviations from this power law prescription can take many forms, including adding a running of the spectral index with wavenumber. Instead, we parameterize the power spectrum as a series of band powers binned in 20 k bins between wave numbers $k = 0.001 \text{ Mpc}^{-1}$ and $k = 0.35 \text{ Mpc}^{-1}$, with $k_{i+1} = 0.756k_i$. We perform a cubic spline over the band powers to ensure smoothness and we normalize the power spectrum in units of 10^{-9} . Similar approaches at reconstructing the primordial power are followed by, e.g., Bridle et al. (2003); Guo et al. (2011); Hložek et al. (2012); Aich et al. (2013); Hunt and Sarkar (2014); de Putter et al. (2014); Miranda et al. (2016); Hazra et al. (2016); Obied et al. (2017). The *Planck* inflation papers (see Planck Collaboration 2016g, 2018f and references therein) performs an exhaustive search over model space, but we restrict ourselves to one model of perturbations.

We compute the power deviation in bins for $0.001 < k/\text{Mpc}^{-1} < 0.35$. This roughly corresponds to a range in multipoles of $14 < \ell < 5000$, given that $\ell = kD(z = 1089)$, where $D(z = 1089) \simeq 14000 \text{ Mpc}$ is the comoving distance to the last scattering surface. Given the degeneracy between the power spectrum amplitude and the optical depth, τ , we present the results in terms of marginalized errors on the quantity $e^{-2\tau}P(k)$. The forecasts are shown in Fig. 21. Picking out the $k^* = 0.2 \text{ Mpc}^{-1}$ scale, which is the scale that shows the largest improvement over current results, we forecast

$$\begin{aligned} \sigma(e^{-2\tau}\mathcal{P}(k^*)) &= 6.5 \times 10^{-12} && \text{SO Baseline,} \\ \sigma(e^{-2\tau}\mathcal{P}(k^*)) &= 5.9 \times 10^{-12} && \text{SO Goal,} \end{aligned} \quad (9)$$

for $e^{-2\tau}\mathcal{P}(k^*) = 1.8 \times 10^{-9}$, a 0.4% measurement. For comparison, $\sigma(e^{-2\tau}\mathcal{P}(k^*)) = 5.3 \times 10^{-11}$ currently for *Planck*, a 3% measurement of the power at these scales. The improvement in the polarization of SO over the current *Planck* constraints (which include high- ℓ temperature and polarization, and low- ℓ polarization with the same prior on τ) leads to a reduction in the error on the primordial power over a wide range of scales $0.001 < k/\text{Mpc}^{-1} < 0.3$. The errors are somewhat sensitive to the choice of binning in the primordial power,

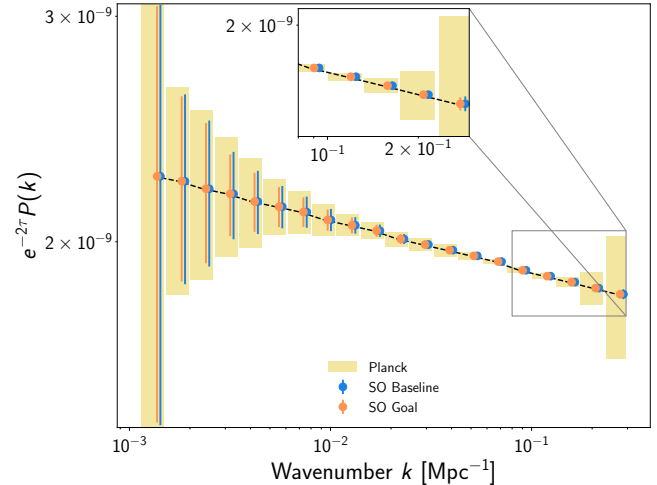


Figure 21. Constraints on the primordial power $e^{-2\tau}P(k)$ from SO baseline (blue) and goal (orange) configurations, compared to estimated constraints from *Planck* temperature and polarization (yellow boxes). The large-scale constraints come from the combined SO+*Planck* temperature and polarization, with *Planck* significantly contributing to the constraint. The largest improvement in the spectra is seen on small scales, where the error on the primordial power spectrum at $k = 0.2 \text{ Mpc}^{-1}$ improves by an order of magnitude thanks to the SO polarization data.

future work will investigate the optimal number of bins given the noise properties of the survey. Finally we note that the constraints are not strongly dependent on the lensing reconstruction $\kappa\kappa$: the SO improvement over *Planck* is dominated by high-precision polarization.

4.3. The Hubble constant

The local Hubble constant, H_0 , can be estimated from the CMB power spectrum for a given cosmological model.

Since 2013, with the first *Planck* cosmological release, the Hubble constant derived from the CMB and its local measurement from Cepheids in Type Ia Supernovae host galaxies are in increasing tension if one assumes the Λ CDM model. They are now discrepant at the level of 3.6σ (see e.g., Planck Collaboration 2018d; Riess et al. 2018 for recent discussions). Recent works have demonstrated that this tension with the local measurement exists even independently of *Planck*, considering for example WMAP or BBN results combined with BAO and SNe (Addison et al. 2018; DES Collaboration 2018; Lemos et al. 2018). The explanation for this discrepancy is currently unknown, and simple extensions to the Λ CDM model cannot explain all current cosmological data. Residual systematics in the data and/or new physics are possible explanations.

The constraint on the power spectra from SO in its baseline configuration²³ translates into a forecast measurement of H_0 in units of km/s/Mpc, within Λ CDM, with

$$\sigma(H_0) = 0.3 \quad \text{SO Baseline.} \quad (10)$$

²³ We note that SO Goal leads to the same measurement, as the constraining power on Λ CDM basic parameters saturates at SO noise levels.

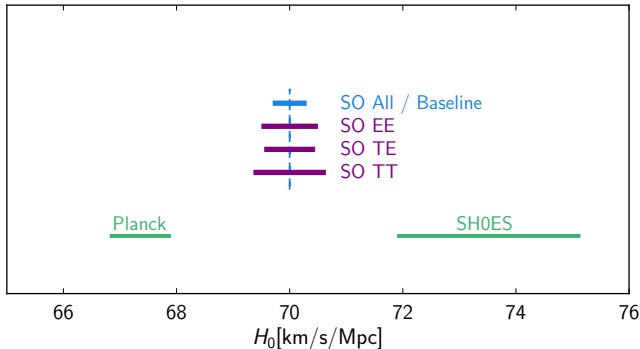


Figure 22. Constraints on the Hubble constant in a Λ CDM model from different SO high- ℓ channels and the full SO baseline dataset (purple and blue bars), compared to the current estimate provided by *Planck* (TT,TT,EE+lowE+lensing, [Planck Collaboration 2018d](#)) and the most recent local measurement from the SH0ES project ([Riess et al. 2018](#)). The SO forecasts are centered on a fiducial value of $H_0 = 70$ km/s/Mpc, i.e., the mean value between the *Planck* and the SH0ES measurements.

This has contributions from each high- ℓ spectrum, with

$$\begin{aligned}\sigma(H_0) &= 0.6 & \text{SO } TT, \\ \sigma(H_0) &= 0.5 & \text{SO } TE, \\ \sigma(H_0) &= 0.5 & \text{SO } EE.\end{aligned}\quad (11)$$

The total uncertainty expected from SO is about a factor of two better than current estimates from *Planck* and five times better than determinations of H_0 from Cepheids in the local universe (see [Riess et al. 2018](#) for the most recent estimates), as shown in Fig. 22.

SO is therefore expected to provide a new compelling CMB estimate of H_0 which will test the *Planck* and other early universe results. Beyond improvement at the statistical level, the sensitivity of the different spectra (TT , TE , EE) will provide three nearly-independent and similarly powerful routes for SO to estimate H_0 , checking for internal consistency and ensuring robustness against systematics. Although the forecast SO numbers include *Planck* data, we note that the significant improvement expected from SO, and a *Planck*-independent new estimate of H_0 , is coming from the $TE+EE$ combination at scales not well measured by *Planck*.

4.4. Additional high- ℓ science

4.4.1. Neutrino mass

One of the ways in which SO will measure the neutrino mass is indirectly via precise measurements of the CMB lensing signal (see Sec. 5 for details). The lensing signal is best measured in the convergence power spectrum computed from temperature and polarization four-point correlations (described in Sec. 5), but it also affects the two-point correlation function, through lensing-induced peak smearing in the temperature and polarization power spectrum. For the LAT baseline configuration, and for CMB power spectrum data alone, we forecast a constraint on the total sum of the masses of

$$\sigma(\Sigma m_\nu)^{2\text{pt}} = 110 \text{ meV}.\quad (12)$$

This constraint from the two-point function is a somewhat weaker constraint than can be derived from the CMB alone using the 4-point function, described in

Sec. 5, where $\sigma(\Sigma m_\nu)^{4\text{pt}} = 90 \text{ meV}^{24}$. From either method, the error improves significantly when including BAO information from DESI. As discussed in Sec. 5, the error would also improve if improved optical depth measurements become available. Both the two-point and four-point estimators yield neutrino mass constraints of the same order of magnitude. Considering that at SO noise levels, correlations between two-point and four-point statistics are at the level of only a few percent ([Peloton et al. 2017](#)), these neutrino mass measurements will provide two nearly-independent constraints and therefore an important robustness check on each other.

4.4.2. Big bang nucleosynthesis

Big bang nucleosynthesis is the process by which light elements were formed in the early universe (for reviews see [Patrignani et al. 2016](#); [Cyburt et al. 2016](#)). In standard cosmology, the predicted primordial light element abundances are determined by the baryon-to-photon ratio (which is fixed by $\Omega_b h^2$ and the current CMB temperature) and radiation energy density as measured by N_{eff} .

We focus here on the primordial abundances of deuterium, parameterized by $y_D \equiv 10^5 n_D/n_H$, and ${}^4\text{He}$, parameterized by $Y_p \equiv 4n_{\text{He}}/n_b$. Theoretical predictions exist for the abundances of ${}^3\text{He}$, ${}^6\text{Li}$, and ${}^7\text{Li}$, but the observational status of these isotopes is much less certain ([Cyburt et al. 2016](#)). We use an interpolation of the results of the PRIMAT code ([Pitrou et al. 2018](#)) to predict y_D and Y_p . The uncertainty on the predicted deuterium abundance is $\sigma(y_D) = 0.06$ and is dominated by the nuclear reaction rate $d(p,\gamma){}^3\text{He}$ ([Adelberger et al. 2011](#)). The theoretical uncertainty of $\sigma(Y_p) = 0.0003$ on the primordial helium abundance is dominated by the neutron lifetime ([Patrignani et al. 2016](#)).

Under the assumption of a standard cosmology with $N_{\text{eff}} = 3.046$, BBN is a one-parameter model depending only on the baryon density, $\omega_b \equiv \Omega_b h^2$, which is precisely measured with the CMB. Astrophysical measurements of primordial light element abundances ([Aver et al. 2015](#); [Cooke et al. 2018](#)) can then be used as a consistency check on the standard BBN model. The results of this comparison with current CMB constraints on $\Omega_b h^2$ from *Planck* ([Planck Collaboration 2018d](#)) and forecast constraints from SO are shown in Fig. 23. For the precision of SO, the consistency check on the primordial abundance of deuterium will be limited by uncertainties on the nuclear reaction rates used for the theoretical prediction from BBN. These uncertainties should be reduced by forthcoming results from low-energy accelerator experiments ([Gustavino 2016](#)).

Motivated by models with non-standard thermal histories, we should seek simultaneous constraints on the primordial helium abundance and the light relic energy density (see e.g., [Fischler and Meyers 2011](#); [Millea et al. 2015](#)). Both the primordial helium abundance and the light relic density impact the damping tail of the CMB power spectrum, and so Y_p and N_{eff} are partially degenerate in CMB constraints when both are allowed to

²⁴ We emphasize that, differently from the numbers reported in Sec. 5, these estimates are CMB-only constraints, i.e., without adding large-scale-structure or improved optical depth data.

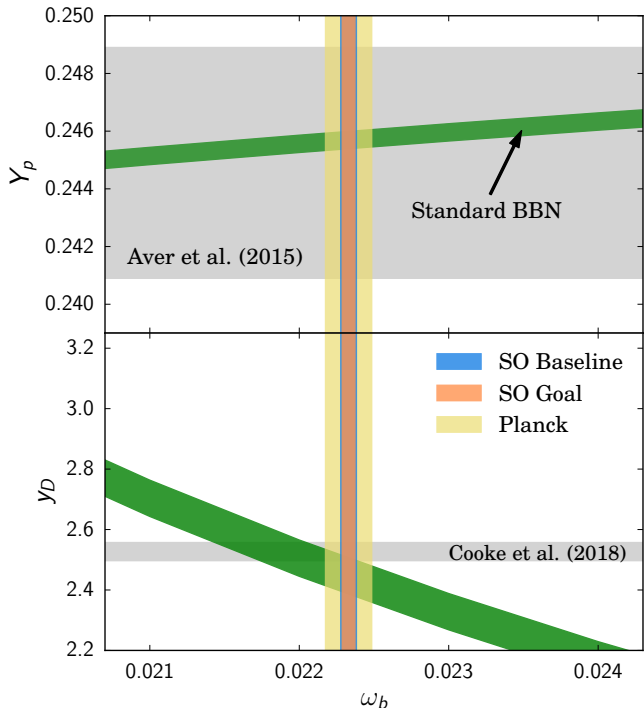


Figure 23. Predictions of the primordial ${}^4\text{He}$ and deuterium abundances assuming standard cosmology and $N_{\text{eff}} = 3.046$ for the current *Planck* constraint and the forecast SO constraint on $\omega_b \equiv \Omega_b h^2$, compared to current astrophysical measurements of the primordial abundances.

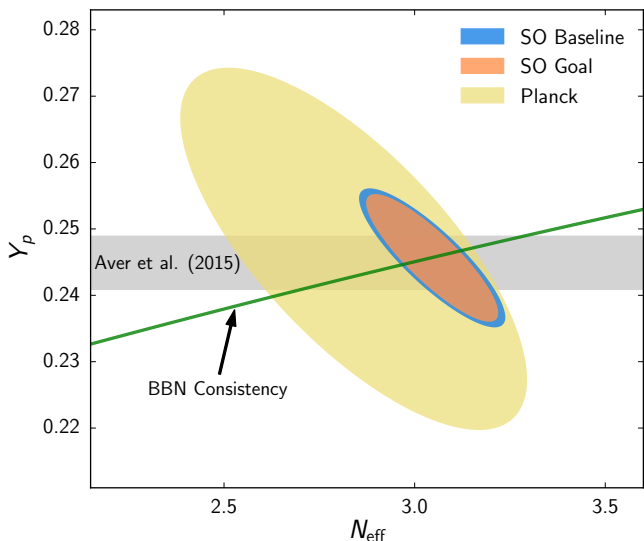


Figure 24. Simultaneous CMB constraints, at 68% confidence level, on the primordial helium abundance and light relic density from *Planck* and forecast constraints from SO. We also show the region predicted by BBN consistency, assuming a constant value for N_{eff} after neutrino freeze-out.

vary. However, this degeneracy is mitigated by effects on the polarization and on the phase of the acoustic oscillations (Bashinsky and Seljak 2004; Hou et al. 2013; Baumann et al. 2016a). In Fig. 24 we show the current constraints from *Planck* (Planck Collaboration 2018d) along

with the error forecasts for SO. We forecast

$$\sigma(Y_P) = 0.007 \quad \text{SO Baseline, varying } N_{\text{eff}}^{25}. \quad (13)$$

These are plotted with the prediction from BBN assuming that the value of N_{eff} remains constant after neutrino freeze-out.

4.4.3. Dark Matter nature and interactions

Evidence for non-gravitational interactions of dark matter particles would provide insight into the unknown physical nature of dark matter. To date, the CMB has opened a valuable window into some of these interactions through the limits on dark matter annihilation (Padmanabhan and Finkbeiner 2005). However, *Planck* has largely saturated this measurement (Madhavacheril et al. 2014; Planck Collaboration 2016e, 2018d; Green et al. 2018), and so SO is expected to improve it by only ~ 30 percent over *Planck*. Below we focus on two scenarios in which SO can substantially improve the sensitivity of CMB searches: elastic scattering of sub-GeV dark matter with Standard Model baryons and ultra-light axion dark matter. We also note that galaxy cluster measurements discussed in Sec. 7 will also provide information on the dark-matter density profiles and thus may prove valuable in constraining other types of DM interactions (see, e.g., More et al. 2016; Berezhiani et al. 2018; Adhikari et al. 2018), but those scenarios are not directly discussed in this paper.

Dark matter–baryon interactions—The dark matter–baryon scattering processes sought by traditional direct-detection experiments can also leave imprints on cosmological observables. They transfer momentum and heat between the dark matter and photon–baryon fluids, damp the acoustic oscillations, and suppress power on small scales in the primary CMB, the linear matter power spectrum, and the CMB lensing anisotropy.

CMB measurements have been used to search for interactions of dark matter particles with masses down to 1 keV (Gluscevic and Boddy 2018; Boddy and Gluscevic 2018; Slatyer and Wu 2018; Xu et al. 2018) – far beyond the reach of current nuclear-recoil based experiments that are optimized to detect weakly interacting massive particles (WIMPs) much heavier than the proton (Cushman et al. 2013). Furthermore, cosmological searches for dark matter are conducted in the context of a wide variety of interaction theories (including the most general non-relativistic effective theory of dark matter–proton elastic scattering) and need not be restricted to a particular dark matter model (Sigurdson et al. 2004; Boddy and Gluscevic 2018; Xu et al. 2018; Slatyer and Wu 2018). Finally, they probe large (nuclear-scale) interaction cross sections which are inaccessible to traditional dark-matter direct searches, due to the extensive shielding of those experiments (Chen et al. 2002; Dvorkin et al. 2014; Emken and Kouvaris 2018). For these reasons, they present a unique avenue for testing dark matter theory, complementary to laboratory searches.

²⁵ Delensing the temperature and polarization sharpens acoustic peaks and further helps to reduce the degree of this degeneracy (Green et al. 2017). The improvement of delensing is however negligible at SO noise levels – only 5% – and therefore not included here.

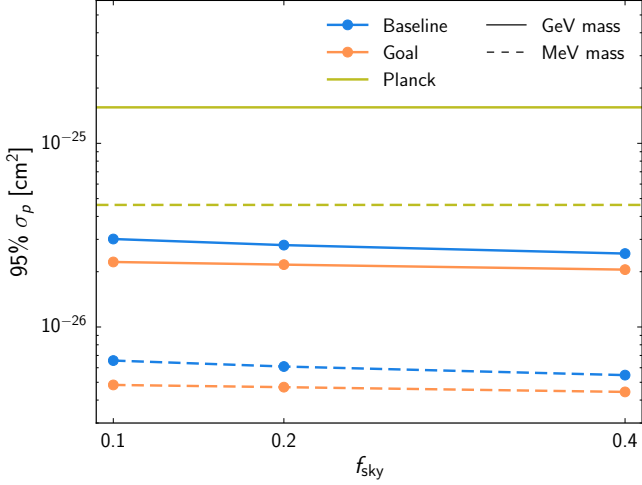


Figure 25. We show current 95% confidence-level upper limits on the cross section for dark matter–proton elastic scattering, derived using *Planck* temperature, polarization, and lensing anisotropy measurements (Gluscevic and Boddy 2018, yellow lines) assuming a velocity-independent spin-independent interaction. Limits for dark matter masses of 1 GeV and 1 MeV are shown as horizontal solid and dashed line, respectively. We also show the projected limits for the baseline and goal SO LAT configurations, as a function of the fractional sky coverage, for the same two masses. We see an improvement of a factor of 7.6 in constraining power for SO with $f_{\text{sky}} = 0.4$, over *Planck*.

In Fig. 25, we show the current 95% confidence-level upper limits on the cross section for elastic scattering of dark matter and protons, for two dark matter particle masses: 1 GeV and 1 MeV, and assuming velocity-independent scattering, from Gluscevic and Boddy (2018). In the same plot, we also show the projected SO upper limits for two configurations (baseline and goal noise levels), for a range of sky areas, f_{sky} , given a fixed observing time. SO is expected to improve the sensitivity to dark matter–proton scattering cross section by a factor of ~ 8 , for a survey that covers 40% of the sky, when temperature, polarization, and lensing are all included in the analysis. We forecast

$$\begin{aligned} \sigma_p(\text{GeV}) &< 3 \times 10^{-26} \text{ cm}^2 \text{ (95\%)} \quad \text{SO Baseline,} \\ \sigma_p(\text{MeV}) &< 5 \times 10^{-27} \text{ cm}^2 \text{ (95\%)} \quad \text{SO Baseline,} \end{aligned} \quad (14)$$

compared to current limits of 2×10^{-25} and 5×10^{-26} cm² respectively from *Planck* (Gluscevic and Boddy 2018).

We find that reducing the noise from the baseline to goal level would improve the limit by about 25%, and narrowing the sky coverage to $f_{\text{sky}} = 0.1$ would degrade the limit by about 15%. We note that the limit is driven by both the measurement of the primary CMB and intermediate- ℓ lensing power spectrum (inclusion of the SO lensing signal, which is discussed in Sec. 5, improves the limits by a factor of 3).

Ultra-light axions— In addition to interactions from massive dark matter candidates, SO will open up a window into non-thermal ultra-light particle dark matter. One example of this candidate dark matter are ultra-light axions (ULAs). Axions were initially proposed to solve the strong CP problem (Peccei and Quinn 1977; Weinberg 1978; Wilczek 1978; Abbott and Sikivie 1983; Iqbal and Sikivie 1983; Moody and Wilczek 1984; Kim and Carosi 2010), however we consider here not the QCD axion with

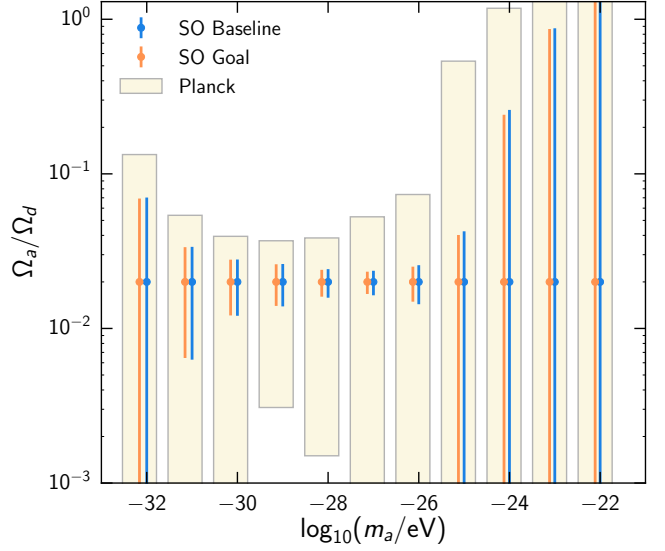


Figure 26. Forecast constraints on the axion fraction, assuming an axion fraction of 2% of the total dark matter content for the baseline (blue) and goal (orange) SO LAT configurations, at a fixed neutrino mass of 0.06 eV. The boxes and error bars represent the 1σ errors from a Fisher matrix analysis. The *Planck* errors match the current constraints in Hložek et al. (2015). SO will greatly improve the chance of detecting even a small amount of axions in the intermediate mass regime, which is bounded at 2σ by current *Planck* constraints.

mass $\sim 10^{-7}$ eV but its much lighter cousin, the ULA, with masses between $10^{-33} < m_a/\text{eV} < 10^{-22}$ (Amendola and Barbieri 2006; Arvanitaki et al. 2010; Hui et al. 2017) The light end of the mass range are axions that exhibit dark-energy-like behavior, while the axions with masses $m_a \geq 10^{-27}$ eV are dark-matter-like.

The ULAs we consider here are created through vacuum realignment and as such are non-thermal dark matter candidates (Amendola and Barbieri 2006; Hwang and Noh 2009; Arvanitaki et al. 2010; Noh et al. 2013; Hui et al. 2017). A recent review of the cosmology of axions is found in Marsh (2016).

At a redshift specified by their mass, the axion field coherently oscillates, and the ULAs transition from behaving more like scalar field dark energy to being a dark-matter-like cosmological component, which has strong cosmological implications for structure formation (Schive et al. 2016; Armengaud et al. 2017; Poulin et al. 2018; Fairbairn et al. 2018). Hence for the lightest axions masses ($m_a \simeq 10^{-33}$ eV, the value of H_0 in eV today), the field is frozen and never begins oscillating and the axions appear dark-energy-like today.

Axions affect the primordial power spectrum by smoothing out structures on small scales through their scale-dependent sound speed (Marsh and Ferreira 2010; Hložek et al. 2015). In addition to these matter-power-spectrum effects, they impart signatures on the CMB temperature and polarization spectra depending on whether the mass transition was before or after decoupling. The lightest axions have a signature on the CMB power spectra similar to dark energy; they generate an Integrated Sachs–Wolfe signal due to the fact that the gravitational potential wells are shallower when the 10^{-33} eV axions dominate the total energy of the universe. We consider the full range of axion masses, to test

the ability of SO to constrain both dark-matter-like and dark-energy-like axions.

For our constraints we make use of the publicly available code `axionCAMB`²⁶, integrated into a modified version of the Fisher forecast code `OxFish` (Allison et al. 2015). We perform a Fisher matrix forecast at fixed mass and vary the allowed axion fraction, where we assume a fiducial value set by the upper limit of current experiments $\Omega_a/\Omega_d = 0.02$ (Hložek et al. 2015). We compute the error on the axion fraction for the baseline and goal LAT configurations and using a sky fraction of $f_{\text{sky}} = 0.4$. These are shown in Fig. 26. The improvement in the constraints with respect to current data is significant, with for example the uncertainty on the axion fraction reducing current limits by more than a factor of 5 for $m_a = 10^{-26}\text{eV}$, as summarized in Table 11.

5. GRAVITATIONAL LENSING

Measurements of CMB lensing underlie many key areas of SO science, including constraints on the tensor-to-scalar ratio, neutrino mass, dark energy, and high-redshift astrophysics. In this section, we detail the calculations we use to guide the design of SO from the perspective of lensing science, focusing on the delensing efficiency (Sec. 5.1), neutrino mass constraints (Sec. 5.2), and science from cross-correlations (Sec. 5.3) including growth of structure, primordial non-Gaussianity, shear bias, and spatial curvature. We show how lensing can be used for halo mass calibration in Sec 5.4, and discuss the impacts of foregrounds in Sec. 5.5.

Our nominal lensing noise curves are described in Sec. 2 and shown in Fig. 6. SO lensing noise is derived based on LAT temperature and polarization data (the SATs have much lower resolution and hence are not useful for lensing measurements); in our derivation, we assume that lensing is reconstructed using the minimum-variance lensing quadratic estimator (Hu et al. 2007a), which is nearly optimal for our noise levels. The noise curves we obtain are used for most of the results of this paper (including Secs. 5.1, 5.2, and also Sec. 4). Deviations from the nominal case are considered in some specific cases. In particular: in Sec. 5.2 we also explore polarization-only estimators; in Secs. 5.3 and 5.4, we apply a foreground cleaning prescription to the gradient leg of the estimator (i.e. the low-pass filtered field in the quadratic estimator), as described in Sec. 5.5; in Sec. 5.4 we in addition apply a maximum ℓ cut of $\ell = 2000$ to the gradient leg of the estimator, as detailed in that section.

5.1. Delensing efficiency

Lensing-induced B -modes limit the measurement of the tensor-to-scalar ratio, r . Fortunately, given an estimate of the particular realization of the CMB lensing potential in a given patch of sky, it is possible to partially undo the effect of lensing on CMB maps (Knox and Song 2002; Seljak and Hirata 2004). This procedure is called ‘delensing’. Delensing reduces the lensing contribution to the B -mode polarization power spectrum, reducing cosmic variance and allowing an improved measurement of any underlying primordial B -modes. The estimate of the lensing potential can be obtained through internal reconstruction, using the CMB maps themselves, or

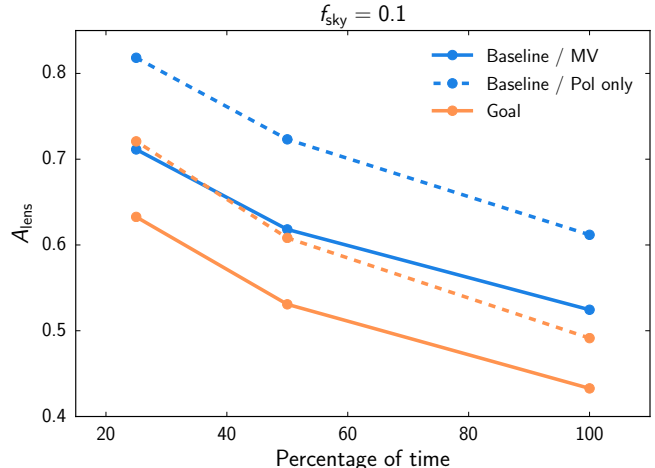


Figure 27. Fraction of lensing B -mode power remaining after delensing, A_{lens} , as a function of time spent observing the SAT survey footprint with the LAT. We show SO baseline and goal sensitivities, using the minimum variance lensing estimator (‘MV’), which combines temperature and polarization data, as well as the polarization lensing estimators alone (‘Pol only’). Here we assume standard ILC foreground cleaning as in Sec. 2.5.1. We note that the nominal plan for sky coverage, as discussed Sec. 2.3, is to spend 25% of the LAT time observing the SAT footprint. For comparison, we anticipate that $A_{\text{lens}} = 0.5$ can be achieved using external delensing.

through appropriately weighted combinations of external tracers of the dark matter, such as the CIB (Sherwin and Schmittfull 2015) or high-redshift galaxies (Smith et al. 2012).

We forecast the fraction of lensing B -mode power remaining in the delensed CMB map, A_{lens} , after delensing. We assume iterative maximum likelihood lensing reconstruction in our forecasts, using the formalism of Smith et al. (2012). We assume the lensing potential will be obtained using the minimum variance lensing estimator, using both temperature and polarization, though, where indicated, we also show polarization-only lensing reconstruction for comparison.

In Fig. 27, we show A_{lens} as a function of the fraction of time spent observing the SAT survey footprint with the LAT. Here, 100% observing time corresponds to the LAT survey covering only the $f_{\text{sky}} = 0.1$ coincident with the SAT survey. Observing percentages of 50% and 25% correspond to a LAT survey covering $f_{\text{sky}} = 0.2$ and 0.4 respectively.

The delensing performance is best for a LAT survey overlapping fully with the SAT. In this case, from Fig. 27, the fraction of B -mode lensing power remaining after delensing is optimistically of order 0.5 for baseline noise, which would reduce $\sigma(r)$ by $\approx 30\%$, as summarized in Table 4. Polarization-only reconstruction, which potentially has fewer systematic concerns, does not perform as well. Foreground cleaning causes a more significant loss of delensing performance in this case.

While this configuration gives optimal delensing, the smaller sky area is non-optimal for SO’s broader science goals. In addition, we expect to achieve A_{lens} of order 0.5 from external delensing (Sherwin and Schmittfull 2015) using CIB emission and other external matter tracers. Though practical delensing demonstrations have not yet achieved such low A_{lens} directly (Larsen et al. 2016; Man-

²⁶ Available at <https://github.com/dgrin1/axionCAMB>.

zotti et al. 2017; Carron et al. 2017), recent work has shown the construction of multi-tracer maps with sufficient correlation with lensing to achieve $A_{\text{lens}} \approx 0.5$ (Yu et al. 2017; Planck Collaboration 2018e).

We therefore anticipate the primary delensing path for SO to come from external delensing. Though the delensing performance is expected to be fairly robust to astrophysical uncertainty (Sherwin and Schmittfull 2015), systematic errors in external delensing are only now being investigated. The internal delensing approach will therefore provide an important cross-check. For the nominal configuration where the LAT surveys $f_{\text{sky}} = 0.4$, we forecast

$$A_{\text{lens}} = 0.71 \quad \text{SO Baseline.} \quad (15)$$

Here we assume the standard ILC foreground cleaning (Deproj-0) described in Sec. 2. We find $A_{\text{lens}} = 0.80$ with more pessimistic foreground cleaning assumptions, using the Deproj-1 method.

5.2. Neutrino mass and lensing spectra

Non-zero neutrino masses suppress the amplitude of fluctuations measured at late times relative to the amplitude measured early on, at the CMB last scattering surface (see, e.g., Lesgourgues et al. 2013). We can exploit this to measure the sum of the neutrino masses using the combination of the primary CMB power spectrum and the CMB lensing potential spectrum. We use a Fisher code to forecast constraints on the sum of neutrino masses using this combination, together with DESI BAO information as described in Sec. 2. We use unlensed $C_{\ell S}$ for the primary CMB and thus do not include any covariance between the primary CMB and the CMB lensing spectra. As discussed in Peloton et al. (2017), this is reasonable for the neutrino mass forecasts here since we include the BAO information which breaks parameter degeneracies (in particular, with the matter density). Here we assume a single-parameter extension to ΛCDM , varying the total sum of the neutrino masses around a fiducial value of 0.06 eV. We consider that only one of the three neutrino species is massive, and that it carries the total mass. This is approximately correct if neutrino masses obey the ‘normal hierarchy’ with the lowest mass zero and the larger mass splitting between the middle and largest-mass states.

We show the anticipated constraints as a function of sky area in Fig. 28. Here we include foreground cleaning with explicit tSZ deprojection for temperature and dust deprojection for polarization (Deproj-1), since these foregrounds could potentially cause the largest systematic effects (see Sec. 5.5 below). We forecast

$$\begin{aligned} \sigma(\Sigma m_\nu) &= 33 \text{ meV} \quad \text{SO Baseline + DESI-BAO,} \\ \sigma(\Sigma m_\nu) &= 31 \text{ meV} \quad \text{SO Goal + DESI-BAO,} \end{aligned} \quad (16)$$

for $\sigma(\tau) = 0.01$ – i.e., for current measurements of τ . The constraints depend only weakly on sky area, and moderately on sensitivity. This is due to constraints being limited by the knowledge of the CMB optical depth τ (e.g., Allison et al. 2015), which allows the high-redshift amplitude of structure to be determined. With a different foreground cleaning assumption, namely Deproj-0, we find $\sigma(\Sigma m_\nu) = 30 \text{ meV}$ for the baseline case.

The constraints on neutrino mass improve significantly with the addition of better τ data, as can be obtained

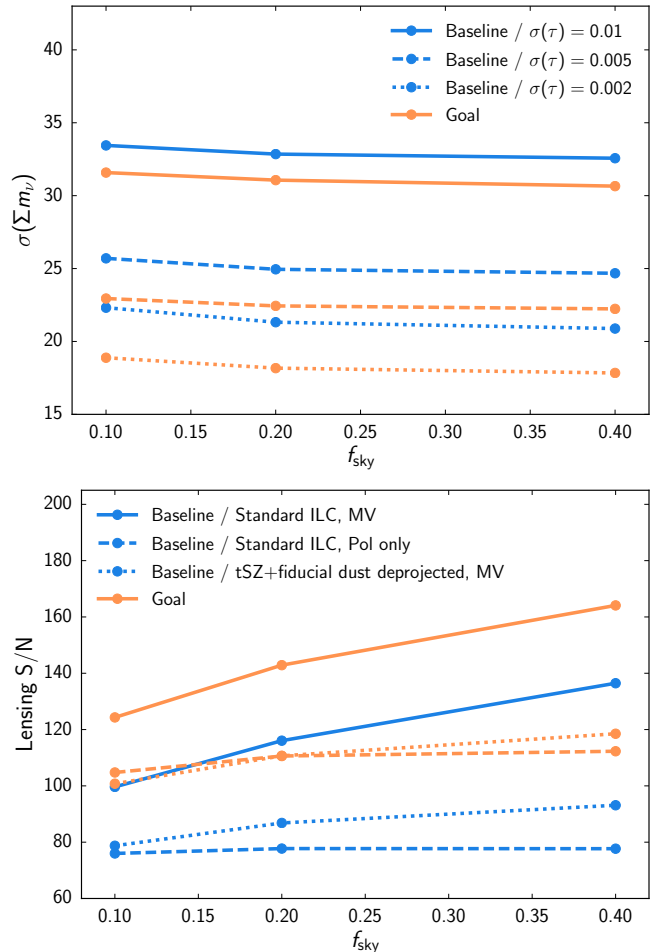


Figure 28. *Top:* Neutrino mass constraints from temperature and polarization CMB power spectra and lensing potential autospectrum, including foreground cleaning with explicit tSZ deprojection for temperature and dust deprojection for polarization, as a function of sky area. *Bottom:* Lensing potential autospectrum signal-to-noise ratio from temperature and polarization CMB data as a function of sky area. Foreground cleaning is included with standard ILC without explicit deprojection (Deproj-0) or tSZ deprojection for temperature and dust deprojection for polarization (Deproj-1), as discussed in Sec. 2.5.1.

from improved measurements of large-angular-scale ($\ell < 30$, $\theta > 6^\circ$) CMB E -modes. Current and upcoming ground-based, balloon, and satellite experiments show great promise to make these measurements. Challenges include dust and synchrotron foreground removal, as well atmospheric instability at ~ 150 GHz and above for ground-based measurements. CLASS (Essinger-Hileman et al. 2014; Appel et al. 2018) is a currently ongoing ground-based experiment aiming to measure large angular scale CMB from the ground at 40/90/150 GHz with a single dust channel at 220 GHz. If the data is sufficient for full foreground cleaning, it would provide a measurement of τ with $\sigma(\tau) = 0.003$ (Watts et al. 2018), which is near the half-sky cosmic variance (CV) limit. BFORE (Bryan et al. 2018b,a) aims to use the improved access to large angular scales and high frequencies offered by the balloon platform to measure the CMB at 150 GHz, and dust at 217/280/353 GHz. The latter would yield a τ measurement, robust to dust contamination, also of $\sigma(\tau) = 0.003$. BFORE has been selected by NASA for

further study, and the current schedule has a launch in 2022. The LiteBIRD satellite (Hazumi et al. 2012; Matsumura et al. 2013; Sekimoto et al. 2018) aims to take all-sky CMB and foreground data at 40–400 GHz, and would be in a position to make an all-sky CV-limited measurement of reionization (i.e., $\sigma(\tau) = 0.002$). LiteBIRD is under study by a large international team, and the current schedule has a launch in 2027. Combining SO with CV-limited reionization data and DESI BAO data, we forecast

$$\begin{aligned}\sigma(\Sigma m_\nu) &= 22 \text{ meV} && \text{SO Baseline} + \text{DESI-BAO} + \tau, \\ \sigma(\Sigma m_\nu) &= 17 \text{ meV} && \text{SO Goal} + \text{DESI-BAO} + \tau.\end{aligned}\quad (17)$$

The latter combination of data would enable a 3.5σ detection of $\Sigma m_\nu = 0.06$ eV (the minimal summed mass allowed in the case of normal mass hierarchy; Capozzi et al. 2017; Esteban et al. 2017; de Salas et al. 2018) and a 5.9σ detection of $\Sigma m_\nu = 0.1$ eV (the minimal summed mass in the case of inverted mass hierarchy).

Even without new measurements of large-scale E -modes, it may also be possible to obtain improved measures of τ using indirect methods with surveys operating from the ground. On the timescale of SO, these methods involve using measurements of ionization perturbations, either of neutral hydrogen from an experiment such as the Hydrogen Epoch of Reionization Array (Liu et al. 2016a) or the kSZ effect from the SO itself (Ferraro and Smith 2018; see Sec. 7.6 below), and to tie these measurements to the spatially averaged ionization state using modeling of reionization. Alternative indirect methods with the CMB that do not rely on such modeling, such as reconstructing large-scale E -modes from the lensed small-scale data (Meerburg et al. 2017) and using the polarized SZ effect from lower-redshift objects (Meyers et al. 2018), require noise levels beyond the reach of SO.

Since the lensing potential power spectrum is a powerful cosmological probe, we also show forecasts for the signal-to-noise ratio of that observable in Fig. 28. We forecast

$$S/N_{\text{lensing}} = 140 \quad \text{SO Baseline.} \quad (18)$$

We note that this signal-to-noise ratio only includes the lensing power spectrum derived from the four-point function. We find that the signal-to-noise ratio improves as sky area increases, although there is minimal improvement when we consider the potentially more systematic-error-free polarization-only lensing power spectrum. We find $S/N = 93$ for Deproj-1 foreground cleaning.

5.3. Cross-correlations

Cross-correlations between maps of the reconstructed CMB lensing potential and low-redshift tracers of the matter distribution provide a handle on the growth of structure, primordial non-Gaussianity, curvature, and dark energy. Here we forecast the science obtainable from cross-correlations of the SO reconstructed lensing potential with LSST, which is particularly suited for this type of analysis because it will observe a large number of galaxies out to high redshift, covering a large fraction of the CMB lensing redshift kernel. The LSST galaxy samples we consider are described in Sec. 2.

For the gold sample, we forecast the cross-correlation coefficient between the SO lensing field, κ (using the min-

imum variance estimator), and the galaxy overdensity field, g , given by $\rho = C_L^{\kappa g} / (C_L^{\kappa\kappa} C_L^{gg})^{1/2}$, to be $\rho \geq 80\%$ for lensing scales $L \leq 80$, with a maximum correlation of $\rho \simeq 86\%$ for $10 \leq L \leq 20$, if the LSST galaxies are optimally weighted in redshift to match the CMB lensing kernel (Sherwin and Schmittfull 2015; Schmittfull and Seljak 2018). We forecast that the optimistic LSST sample will improve the cross-correlation coefficient to $\rho \geq 80\%$ for $L \leq 150$, with a maximum correlation of $\rho \simeq 90\%$ for $15 \leq L \leq 25$.

These high cross-correlation coefficients imply that sample variance cancellation can be useful (Seljak 2009), and thus that the naive signal-to-noise ratio calculation for a cross spectrum can underestimate the potential constraining power of combining CMB and large-scale structure (LSS). We include this sample variance cancellation by forecasting joint constraints from SO lensing and LSST clustering power spectra, $C_L^{\kappa\kappa}$, $C_L^{\kappa g}$, and C_L^{gg} , accounting for (Gaussian) covariances between these power spectra.

Here and in Sec. 5.4, we assume a CMB lensing estimator where only the CMB gradient in the quadratic estimator pair has explicit deprojection of foregrounds (Madhavacheril and Hill 2018), which is suitable for cross-correlation measurements. We discuss this gradient foreground cleaning in Sec. 5.5.

5.3.1. Growth of structure: $\sigma_8(z)$

We forecast how well the growth of structure as a function of redshift, parametrized by the amplitude of matter perturbations, $\sigma_8(z)$, could be constrained by combining LSST galaxies and SO CMB lensing data, for different sky fractions and sensitivities. We consider six tomographic redshift bins ($z = 0-0.5, 0.5-1, 1-2, 2-3, 3-4, 4-7$) and marginalize over one linear galaxy bias parameter in each bin. As in Sec. 5.3, our observables are $C_L^{\kappa\kappa}$, $C_L^{\kappa g}$ and C_L^{gg} . We assume scale-cuts in both L and k (which the Limber approximation maps to an L for each redshift bin) of $L_{\text{min}} = 50$ and $k_{\text{max}} = 0.3h/\text{Mpc}$. We follow the standard methods described in Sec. 2, marginalizing over ΛCDM parameters and including DESI BAO information. In this analysis, however, we allow $\sigma_8(z)$ to vary independent of the expansion history. We assume ΛCDM for the background expansion; we also neglect any effect on the CMB power spectra.

We show projected constraints in Fig. 29, finding forecasts for $\sigma_8(z)$ that are competitive with cluster and weak lensing probes, with percent-level forecast constraints on the amplitude of structure for a significant number of redshift bins. We find that constraints improve moderately as sky area and sensitivity are increased, as shown in Fig. 29. For the nominal SO survey we project

$$\begin{aligned}\sigma(\sigma_8)/\sigma_8 &= 0.015 \quad (z = 1-2), \text{ SO Baseline} + \text{LSST} \\ &= 0.015 \quad (z = 2-3).\end{aligned}\quad (19)$$

These measurements would provide unique constraints on deviations from the cosmological constant, Λ , at redshifts higher than typically accessible to optical cluster and weak lensing probes. These deviations could include modified gravity, non-standard dark energy models, as well as other deviations from ΛCDM .

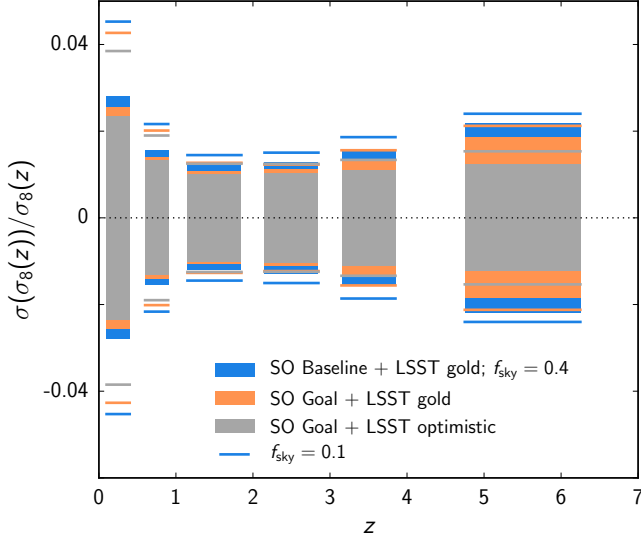


Figure 29. The relative uncertainty on σ_8 , defined in six tomographic redshift bins ($z=0-0.5, 0.5-1, 1-2, 2-3, 3-4, 4-7$), as a function of redshift. The forecast assumes a joint analysis of $C_L^{\kappa\kappa}, C_L^{\kappa g}$ and C_L^{gg} , where κ is SO CMB lensing and g denotes LSST galaxies binned in tomographic redshift bins. We use multipoles from $L_{\min} = 30$ to L_{\max} corresponding to $k_{\max} = 0.3h\text{Mpc}^{-1}$ in each tomographic bin. We marginalize over one linear galaxy bias parameter in each tomographic bin and over ΛCDM parameters. We also include *Planck* CMB information – with a τ prior, $\sigma(\tau) = 0.01$ – and BAO measurements (DESI forecast). The filled bands and single lines distinguish between an SO survey over $f_{\text{sky}} = 0.4$ and 0.1, respectively. Different colors distinguish between the SO baseline and goal configurations, and for this latter case different LSST number density, with 29.4 and 66 arcmin^{-2} galaxies for the gold and optimistic sample, respectively.

5.3.2. Local primordial non-Gaussianity

Local primordial non-Gaussianity, parameterized by the amplitude f_{NL} , can be generated by multi-field inflation models, and a measurement of non-zero $|f_{\text{NL}}| \gtrsim 1$ would robustly rule out all single-field inflation models with standard Bunch-Davies initial conditions (Maldacena 2003; Creminelli and Zaldarriaga 2004). Observationally, in addition to the effect on higher-point functions described in Sec. 6, this type of non-Gaussianity leads to a distinct scale-dependence of galaxy bias on large scales, scaling as a function of comoving wavenumber k as f_{NL}/k^2 (Dalal et al. 2008). A joint analysis of CMB lensing and galaxy clustering data can search for this effect by comparing the scale-dependence of lensing and clustering auto- and cross-spectra on the largest scales. The high cross-correlation coefficient between SO lensing and LSST clustering discussed above allows us to cancel part of the sample variance that usually limits constraints derived from large scales.

The forecasts of local f_{NL} from cross-correlations between SO lensing and LSST clustering are shown in Fig. 30, following a similar procedure as for $\sigma_8(z)$ (using the same six tomographic LSST redshift bins and marginalizing over the same linear bias parameters). We find that competitive constraints are possible with SO. If clustering and CMB lensing data are used down to $L_{\min} = 20$, we project

$$\begin{aligned} \sigma(f_{\text{NL}}) &= 1.8 && \text{SO Baseline + LSST-gold,} \\ \sigma(f_{\text{NL}}) &= 1.2 && \text{SO Baseline + LSST-opt.} \end{aligned} \quad (20)$$

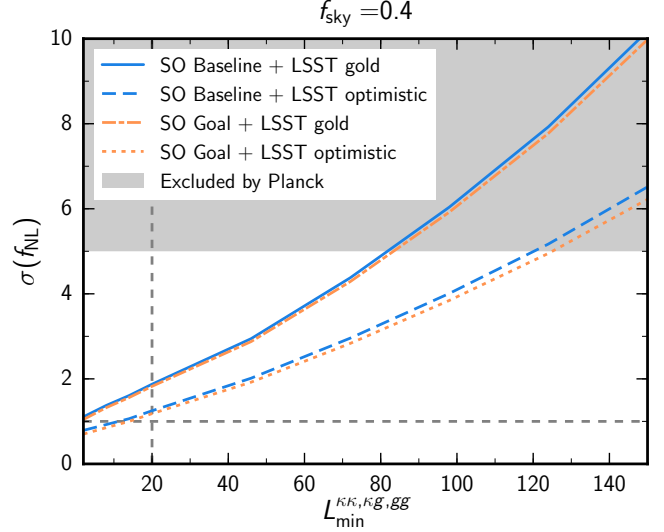


Figure 30. Constraint on local primordial non-Gaussianity expected from SO CMB lensing (minimum variance combination, including foreground-deprojected gradient cleaning; Madhavacheril and Hill 2018) cross-correlated with LSST galaxy clustering, exploiting the large-scale scale-dependent bias effect from f_{NL} (Dalal et al. 2008). Different lines show different assumptions about SO sensitivity and LSST number density and redshift distribution. The gray shaded region is excluded by *Planck* (Planck Collaboration 2016f). We marginalize over the amplitude of one linear galaxy bias parameter per tomographic redshift bin that rescales the fiducial bias redshift dependence $b(z) = 1 + z$ (LSST Science Collaboration 2009). We also marginalize over an artificial parameter that changes the matter power spectrum with the same shape as f_{NL} changes the galaxy bias (see Schmittfull and Seljak 2018 for details). The gray dashed vertical line marks our primary forecasts in Eq. 20 with $L_{\min}=20$, the horizontal line marks the $f_{\text{NL}}=1$ target.

This is close to the value of $f_{\text{NL}} = 1$ that is typically chosen as a target in efforts to separate multi-field from single-field inflation models. These constraints improve as sky area is increased, but the strongest dependence is on the minimum lensing and galaxy density multipole used in our analysis. Indeed, we project that $\sigma(f_{\text{NL}}) = 1$ could be achieved for lensing- and clustering- $L_{\min} = 14$, assuming SO baseline sensitivity and optimistic LSST galaxies, and the error would be reduced even further with lower L_{\min} . This motivates preserving low multipoles when designing SO lensing and LSST clustering observations and analysis pipelines for this kind of measurement.

Most of the f_{NL} constraint comes from comparing $\kappa\kappa$ and gg power spectra on large scales. It is also possible to work only with $\kappa\kappa$ and κg on very large scales and include gg only on smaller scales; however this degrades the f_{NL} forecast by a factor of two or more, since sample-variance cancellation is no longer fully effective.

The above forecast assumes that f_{NL} is only measured from a scale-dependent difference between $\kappa\kappa, \kappa g$ and gg that scales as f_{NL}/k^2 on large scales. This is implemented by marginalizing over an artificial f_{NL} parameter that rescales the matter power spectrum in the same way as f_{NL} rescales the galaxy bias, so that any information from gg alone is not taken into account and only the relative bias between clustering and lensing is used (Schmittfull and Seljak 2018).

Alternatively, f_{NL} can be constrained from LSST alone by measuring the shape of the large-scale gg power spec-

trum assuming that the matter power spectrum and large-scale galaxy bias are known. This can also achieve $\sigma(f_{\text{NL}}) \simeq 1\text{--}2$, but with different systematics. In particular, such a gg -only measurement is only sensitive to the absolute value of the large-scale gg power spectrum rather than the relative ratio between lensing and clustering power spectra. Additionally, a cross-correlation analysis can help to reduce the impact of catastrophic photo- z errors, because these errors affect κg and gg power spectra differently, so that measuring these spectra can constrain catastrophic outlier rates and f_{NL} simultaneously. This is the case for a simple idealized parameterization of the distribution of catastrophic errors (Schmittfull and Seljak 2018), but requires further study in the case of more realistic LSST catastrophic photo- z errors. Using cross-correlations with SO can therefore help to increase the robustness of f_{NL} constraints from LSST alone.

5.3.3. Shear bias validation

The upcoming optical lensing experiments, such as LSST, Euclid and WFIRST, will rely on shear measurements, achieved by estimating the correlated shapes of galaxies, to deliver percent-level precision measurements of the amplitude of structure as a function of redshift. This task is complicated by various systematics which bias the shear. The resulting shear multiplicative bias is degenerate with the amplitude of structure, which makes it a critical systematic for optical lensing surveys. State-of-the-art optical lensing analyses currently reach $\sim 1\%$ shear calibration (Zuntz et al. 2017; Fenech Conti et al. 2017; Mandelbaum et al. 2017), relying in most – but not all – cases on image simulations, and are expected to achieve the stringent $\sim 0.5\%$ requirement for LSST, Euclid and WFIRST (Huterer et al. 2006). Newer techniques using meta-calibration may even achieve 0.1% shear calibration (Sheldon and Huff 2017). However, because the shear multiplicative bias is such a crucial systematic, any independent method to calibrate or validate it will be valuable, and will add confidence to any potential dark energy discovery from LSST, Euclid and WFIRST.

CMB lensing from SO can provide such an external validation (Schaan et al. 2017). Indeed, jointly analyzing auto- and cross-correlations of CMB lensing with galaxy shear and galaxy number density gives information on the shear multiplicative bias. This method has been proposed in Vallinotto (2012), Vallinotto (2013), and Das et al. (2013) and subsequently applied to current datasets (e.g., in Liu et al. 2016b; Baxter et al. 2016; Miyatake et al. 2017; Singh et al. 2017). In Fig. 31 we show how combining CMB lensing from SO with galaxy number density and shapes from LSST enables a shear calibration close to the LSST requirements in many redshift bins, while marginalizing over nuisance parameters (galaxy bias and photometric redshifts) and varying cosmological parameters. In this forecast, we assume a conservative LSST lens sample as in Schaan et al. (2017), to guarantee accurate photometric redshifts. This process is independent from any shear calibration internal to LSST, Euclid, and WFIRST. It is also robust to expected levels of intrinsic alignment, to uncertainties in non-linearities and baryonic effects, and to changes in the photo- z accuracy, as verified in Schaan et al. (2017). A similar level

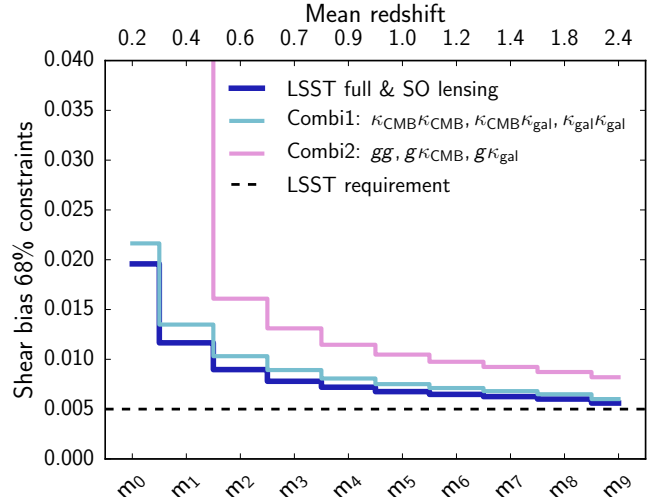


Figure 31. 68% confidence-level constraints on the shear biases m_i for the 10 tomographic bins of LSST, when self-calibrating them from the cross- and auto-correlations of CMB and galaxy lensing (combination 1, light blue), from clustering and the cross-correlation of galaxy density with CMB and galaxy lensing (combination 2, pink) and the full LSST & SO lensing (dark blue). The self-calibration is very close to the level of the LSST requirements (black dashed line) for the highest redshift bins, where shear calibration is otherwise most difficult. We stress that all the solid lines correspond to self-calibration from the data alone, without relying on image simulations. CMB lensing will thus provide a valuable consistency check for building confidence in the results from LSST.

of shear calibration is achieved with WFIRST or Euclid instead of LSST.

5.3.4. Lensing ratios: curvature

Two-point correlation functions between galaxies and gravitational lensing are powerful cosmological probes. However, fully exploiting the available signal is complicated by the challenges of modeling the small-scale regime, where non-linearities, baryons and galaxy bias all become important. Several authors (Jain and Taylor 2003; Hu et al. 2007b; Das and Spergel 2009) have pointed out that these complications can be circumvented by measuring ratios of lensing-galaxy two-point functions involving a single set of ‘lens’ galaxies and multiple gravitational lensing source planes. In the limit that the lens galaxies are narrowly distributed in redshift, such ‘lensing ratios’ reduce to a purely geometrical ratio of angular diameter distances. The sensitivity of lensing ratios to cosmological distances make them useful cosmological probes, while the fact that they are insensitive to the lens galaxy power spectrum means that all available signal at small scales can be exploited without difficult modeling.

On account of the large distance to the last scattering surface, the cosmological sensitivity of the lensing ratios can be dramatically increased by using the CMB as one of the gravitational lensing source planes (see, for example, recent first measurements in Miyatake et al. 2017 and Singh et al. 2017). In this case, the lensing ratios are particularly sensitive to the curvature of the universe. Purely geometric constraints on curvature from the primary CMB alone are significantly degraded by degeneracies between the matter density, curvature, and the equa-

tion of state of dark energy (i.e., the so-called geometric degeneracy). The addition of lensing ratio measurements breaks this degeneracy and can yield significantly tighter constraints on the curvature density parameter, Ω_k , while still relying on purely geometric information.

The combination of CMB lensing maps from SO and galaxy imaging from LSST can be used to place tight constraints on lensing ratios. In order for the galaxy power spectrum to cancel in the lensing ratio, the lens galaxies must be narrowly distributed in redshift. We find that bins of width $\Delta z = 0.05$ are sufficiently narrow, given the projected uncertainties on the ratio measurements. Such redshift accuracy can be achieved photometrically in LSST data using an algorithm like `redMaGiC` (Roza et al. 2016). A `redMaGiC`-like selection would sacrifice number density for the improved photometric accuracy necessary for using lensing ratios.

Given these considerations, for this forecast we do not use the same assumptions about LSST as described in Sec. 2. Instead we assume that LSST can provide a population of lens galaxies divided into redshift bins of width $\Delta z = 0.05$ between $z = 0.2$ and $z = 0.7$ with a number density of 100 per square degree in each bin. These numbers are comparable to what is achieved currently from the Dark Energy Survey (Cawthon et al. 2018). We further assume that LSST provides a source galaxy population distributed between $z = 1.2$ and $z = 1.6$ with density of 25 galaxies per square arcminute; the source galaxies are assumed to have photometric redshifts that are accurate to 1%, and we assume that multiplicative shear bias can be controlled to the 0.1% level (Sheldon and Huff 2017), although our projections are not very sensitive to this assumption.

Assuming overlap between SO and LSST of 40% of the sky, we find that the lensing ratios can be measured to roughly 3% precision assuming SO goal sensitivity, with some variation depending on the lens galaxy redshift bin. We adopt SO projections for CMB lensing maps generated via the gradient field cleaning described in Sec. 5.5. When combined with geometric information from the primary CMB anisotropies (using the geometric CMB likelihood of Aubourg et al. 2015), we project that constraints of roughly $\sigma(\Omega_k) = 0.026$ can be achieved in a Λ CDM+ $w_0+\Omega_k$ scenario, after marginalizing over the matter and baryon densities, $\Omega_m h^2$ and $\Omega_b h^2$, the dark energy equation of state parameter, w_0 , the Hubble constant, h , and systematics parameters describing photometric redshift and shear calibration uncertainty. It should be emphasized that a constraint obtained in this way is purely geometrical, depending only on the distances to the lens and source galaxies and to the last scattering surface. It does not make use of any information coming from the growth of structure or the matter power spectrum.

5.4. Halo lensing: mass calibration

With arcminute resolution of the CMB, gravitational lensing on cluster and galaxy group scales can be resolved (see Seljak and Zaldarriaga 2000; Holder and Kosowsky 2004) and has been measured with data (Madhavacheril et al. 2015; Baxter et al. 2015, 2018; Planck Collaboration 2016j; Geach and Peacock 2017). Such ‘halo lensing’ measurements of the 1-halo-dominated lensing contribution from dark matter halos allow for constraints on the

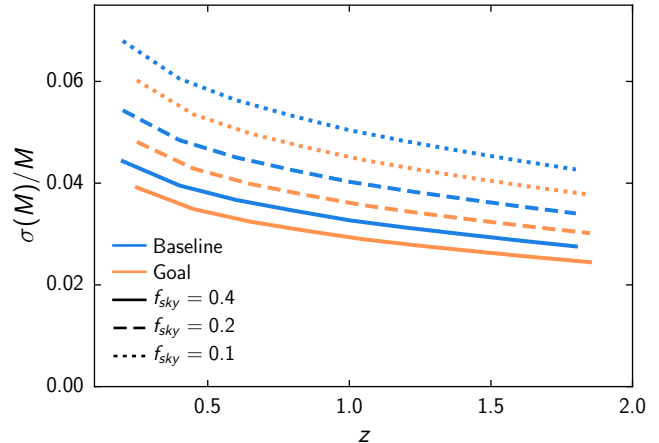


Figure 32. The relative mass calibration uncertainty from CMB halo lensing on a sample of clusters $N = \{1000, 500, 250\}$ for corresponding fixed-time observations over $f_{\text{sky}} = \{0.4, 0.2, 0.1\}$ as a function of mean redshift of the sample. The sample is assumed to be of mean mass $M_{500} = 2 \times 10^{14} M_{\odot}/h$. Both temperature and polarization data are used and noise from temperature foregrounds is included.

total halo mass while being mostly independent of assumptions about baryonic physics. CMB lensing measurements of halos will enable mass calibration of the SZ cluster sample from SO (described in Sec. 7) as well as cluster and galaxy group samples from external optical surveys. This will provide a complementary mass calibration to that obtained from optical weak lensing follow-up using LSST background galaxies. The high-redshift cluster sample ($z > 0.7$) will rely on this measurement, since optical measurements at these high redshifts will suffer from photometric redshift uncertainties, systematics, and a general decline in the number of available background galaxies.

Polarization-derived lensing estimators can also be used to get complementary information on the mass calibration with minimal and differing systematics due to foregrounds. At SO sensitivities, polarization-only estimators have 2 to 3 times lower sensitivity than minimum variance estimators, but are still informative and can be used as a cross-check for systematics.

In Fig. 32, we show the relative mass calibration uncertainty, $\sigma(M)/M$, expected for SO as a function of redshift when using both temperature and polarization data (we follow the Madhavacheril et al. 2017 method). This combination of foreground-cleaned temperature and polarization data is designed to be free from bias from the tSZ effect using the ideas described in Madhavacheril and Hill (2018), as discussed in Sec. 5.5. We note that the quadratic estimator used for halo lensing uses a maximum CMB multipole of $\ell = 2000$ for the gradient since this significantly reduces a mass-dependent bias when probing small scales. For the nominal $f_{\text{sky}} = 0.4$, we project that SO can calibrate the mass of a sample of 1000 clusters to

$$\sigma(M)/M(z = 1) = 0.03 \quad \text{SO Baseline.} \quad (21)$$

Deeper measurements would improve the mass sensitivity on any given cluster, but since constraints are obtained on a stack, increasing the survey overlap with a fixed cluster sample improves the overall constraint. In Sec. 7, we use an internal SZ-detected sample to forecast

cosmological parameters, and discuss the optimal survey design.

A promising application of CMB halo lensing mass calibration is applying it to measurements of the splashback radius (More et al. 2016; Baxter et al. 2017), which has recently been established as a useful dynamical boundary of dark matter dominated halos. With the large SZ cluster sample provided by SO, high accuracy measurements of splashback which can be compared with simulation based predictions will be available, and this comparison will benefit from precise mass calibration from a combination of galaxy lensing and CMB halo lensing with SO. The splashback radius itself is also a test of the physics of dark matter and gravity, and useful for galaxy evolution studies.

5.5. Impact of foregrounds on lensing

Extragalactic and Galactic foregrounds can significantly affect measurements of both gravitational lensing and delensing (van Engelen et al. 2014; Osborne et al. 2014; Ferraro and Hill 2018). The trispectra of objects such as galaxy clusters and galaxies and the bispectra from their cross-correlation with the lensing field will give biases on measurements of the power spectrum of the lensing potential. Though simulated estimates have been made in some cases, many of these higher order statistics have not yet been fully measured in CMB data.

Several approaches exist for characterizing or avoiding these biases: One can attempt to reduce them using their known statistical properties (i.e., bias hardening); one can deproject them with multi-frequency observations; one can use a shear-only estimator; or one can use polarization-only data.

Bias hardening: One method to reduce the impact of non-Gaussian unresolved foregrounds is to form optimal estimates for these signals in the CMB maps. One can then project them out of lensing estimates, a procedure known as ‘bias hardening’ (Namikawa et al. 2013). This has been shown to reduce the contamination from the tSZ effect and the CIB (Osborne et al. 2014), and was recently applied to the analysis of the *Planck* data (Planck Collaboration 2018e).

Gradient cleaning: Another promising approach, particularly for cross-correlations and halo lensing, is to clean the CMB gradient part of the pair of maps used in the quadratic estimator using a combination of SO and existing *Planck* data (Madhavacheril and Hill 2018). At SO frequencies of 93 and 145 GHz where the CMB lensing signal is most informative, there is considerable contamination from tSZ, as well as emission from dusty sources, kSZ, and potential unmasked synchrotron sources. Foregrounds such as tSZ and CIB introduce a significant bias even if a standard ILC procedure is performed to obtain a minimum variance CMB map. This necessitates projecting out the foregrounds through constrained ILC. It is, however, sufficient to perform foreground deprojection on the low-resolution gradient estimate used in the quadratic estimator. Ensuring that the gradient alone is foreground-free eliminates much of the bias while ensuring that there is only a small loss of signal-to-noise ratio.

In our forecasts for cross-correlations (Sec. 5.3) and

halo lensing (Sec. 5.4), we assume this gradient cleaning when generating noise curves. Specifically, for the TT estimator, the CMB gradient part of the quadratic estimator pair utilizes tSZ- and CIB-deprojected constrained ILC temperature maps for large-scale cross-correlations (Sec. 5.3) and tSZ-deprojected constrained ILC temperature maps for halo lensing (Sec. 5.4), where the foreground cleaning procedure is discussed in more detail in Sec. 2. We include CIB deprojection for the large-scale cross-correlations since a high-redshift LSST sample can have significant overlap with the CIB, which peaks at a redshift of around 2.

For CMB halo lensing, we only include tSZ deprojection since tSZ is expected to be the dominant foreground contaminant in an SZ selected sample of clusters for redshifts $z < 2$. (However, CIB cleaning could also be included straightforwardly.) The non-gradient map of the quadratic estimator pair uses the standard ILC temperature map. All other estimators use corresponding standard ILC maps. This procedure does not remove the bias from kSZ, although that bias can be alleviated by lowering the maximum multipole used in the gradient at the cost of some signal-to-noise in the TT estimator at large scales.

Shear-only estimator: It has been recently shown that we can use the different symmetries of the foregrounds and lensed CMB to obtain unbiased lensing reconstruction (Schaan and Ferraro 2018). In particular, a ‘shear-only’ estimator is approximately immune to foreground contamination. This method simultaneously eliminates biases from all of the extragalactic foregrounds, including those from the tSZ, kSZ, CIB, and radio point sources. In addition, it allows for reconstruction on a larger range of multipoles, therefore increasing the overall statistical power.

Polarization-only estimators: A final approach is to rely only on polarization data. SO will be in a regime where roughly equal signal-to-noise ratio will be available with polarization and with temperature. Using polarization data is beneficial as extragalactic emission is low in polarization. However, when using polarization data, sources of non-Gaussianity that can impact lensing measurements include Galactic dust at high frequencies and Galactic synchrotron at low frequencies (Fantaye et al. 2012). Current data from the *Planck* satellite do not have low enough noise on the small angular scales of interest to definitively determine the impact of the non-Gaussianity of the polarized dust. A study by the CORE team (Challinor et al. 2018) using simulations found a non-negligible bias on lensing from polarization data using part of the sky within the *Planck* analysis mask, though it could be mitigated with a modification of the lensing weights. The situation is similar for small-scale synchrotron. These potential challenges motivated the choice of a wide frequency coverage for the LAT, including frequencies to characterize both synchrotron and dust, to permit the removal of these possible contaminants if they are non-negligible, along with providing powerful null tests.

6. PRIMORDIAL BISPECTRUM

The CMB bispectrum is a powerful observable to constrain possible interactions in the early universe. In inflationary models, vacuum fluctuations in the early universe source both scalar and tensor perturbations, and through weak gravitational interactions one expects small corrections to Gaussianity (Maldacena 2003). Predicted levels in the simplest inflationary scenarios will therefore be hard to observe, even with future CMB and LSS measurements. However, deviations from the simplest models can easily generate large non-Gaussianities, e.g., via non-canonical kinetic terms, the presence of multiple fields, or through particle production (Komatsu et al. 2009).

The CMB has been at the forefront of constraining non-Gaussianities through their effect on the three- and four-point correlation functions. The most stringent bounds on any form of non-Gaussianity has been derived using the *Planck* data (Planck Collaboration 2016f). The most interesting type of non-Gaussianities are the so-called local and equilateral type as they provide a fairly robust physical interpretation (see, e.g., Alvarez et al. 2014). Observable levels of local non-Gaussianity are expected when more than one field is involved in the inflationary dynamics, while equilateral non-Gaussianities are expected if the inflaton is strongly coupled. As mentioned in Sec. 5.3.2, an interesting theoretical target widely shared within the community is $f_{\text{NL}} \sim \mathcal{O}(1)$, both for local and equilateral non-Gaussianities (Alvarez et al. 2014). *Planck* yields $\sigma(f_{\text{NL}}^{\text{local}}) = 5$ (Planck Collaboration 2016f).

Here we present the forecast constraints using SO combined with *Planck*. We combine errors as $\sigma^{-2}(f_{\text{NL}}) = \sigma^{-2}(f_{\text{NL}}^{\text{Planck}}) + \sigma^{-2}(f_{\text{NL}}^{\text{SO}})$, which is non-optimal but approximates an analysis that combines the Fisher information before inverting. For the *Planck* constraints, we use only the fraction of the sky not observed by SO. The current *Planck* constraints are derived from $f_{\text{sky}} \sim 0.75$, so combining with SO at $f_{\text{sky}} = 0.4$, we will use only $f_{\text{sky}} = 0.35$ for $\sigma(f_{\text{NL}}^{\text{Planck}})$. Our results match the current constraints from *Planck* for $f_{\text{sky}} = 0.75$ in the *Planck* only case. On scales below $\ell = 40$ in the SO LAT patch, we use *Planck* noise. We consider local, equilateral, and orthogonal non-Gaussianities. We forecast the scalar bispectra, $\langle\zeta\zeta\zeta\rangle$, using the SO LAT combined with *Planck*, using the LAT ILC noise curves described in Sec. 2 (Deproj-0) and with tSZ and CIB SED deprojected out in temperature for $\langle TTT \rangle$ only (Deproj-3), as recently shown to be important for avoiding biases in Hill (2018). For the tensor-scalar-scalar forecasts, $\langle\gamma\zeta\zeta\rangle$, we include the SO SATs, and constraints derived only use 10% of the sky. Following Sec. 2, we use ILC noise curves at low multipoles ($30 \leq \ell \leq 260$). For the baseline forecasts we use $1/f$ noise parameterized by $\ell_{\text{knee}} = 50$, and $\ell_{\text{knee}} = 25$ for goal. Here we assume that the SATs have uniform coverage over 10% of the sky, which is an approximation to the expected sky survey. We assume that delensed B -modes have $A_{\text{lens}} = 0.75$ (baseline) and 0.5 (goal).

Our forecasts are summarized in Table 6. In the most optimal case, combined forecasts with *Planck* cannot reach the threshold of $f_{\text{NL}}^{\text{local}} = 1$. Instead, constraints improve over *Planck* by $\approx 50\%$, which is anticipated

Table 6

Forecast constraints on non-Gaussianity ($\sigma_{f_{\text{NL}}}$). The scalar bispectra ($\langle\zeta\zeta\zeta\rangle$) use the SO LAT combined with *Planck*. The tensor-scalar-scalar ($\langle\gamma\zeta\zeta\rangle$) forecasts add the SO SATs.

Shape ($\langle\zeta\zeta\zeta\rangle$) $\langle TTT \rangle, \langle TTE \rangle,$ $\langle TEE \rangle, \langle EEE \rangle$	Current (<i>Planck</i>)	SO Baseline	SO Goal
local	5	4	3
equilateral	43	27	24
orthogonal	21	14	13
Shape ($\langle\gamma\zeta\zeta\rangle$) $\langle BTT \rangle, \langle BTE \rangle, \langle BEE \rangle$	(WMAP)		
local	28 ^a	2	1
equilateral	-	13	8
orthogonal	-	6	3

^aConstraint derived from temperature only and shape considered is not exactly $f_{\text{NL}}^{\text{local}}$. There are currently no constraints on equilateral and orthogonal non-Gaussianities $\langle\gamma\zeta\zeta\rangle$.

by mode counting. In Secs. 5 and 7 we show that cross-correlation of LSST data with CMB gravitational lensing and the kSZ effect from SO can further improve constraints on $f_{\text{NL}}^{\text{local}}$. In principle, these three constraints can be combined.

Thus far we have only considered non-Gaussianities sourced by scalar perturbations in the early universe. Recently, a growing body of work (Maldacena and Pimentel 2011; Lee et al. 2016; Bordin et al. 2016; Baumann et al. 2018; Domènech et al. 2017) has explored the possibility of non-Gaussianities sourced by tensors (Meerburg et al. 2016). Interestingly, tensor non-Gaussianities are hard to produce (Bordin et al. 2016) and a detection would almost certainly signal new physics, such as the presence of higher-order massive spin particles (Lee et al. 2016; Baumann et al. 2018), or extra gauge particles (Agrawal et al. 2018). Unlike the scalar non-Gaussianities, observational constraints on tensor non-Gaussianities have only been considered in the CMB through their effect on the temperature bispectrum (Shiraishi et al. 2018).

In the scalar bispectra forecasts we use temperature, T , and E -mode polarization data. With tensors, we can add B -mode polarization, which has a smaller contribution from cosmic variance. Constraints on non-Gaussianities from a bispectrum containing at least one tensor will therefore improve significantly when adding B -mode data from SO (Meerburg et al. 2016). As an example, we show forecasts for a coupling between two scalars and a tensor derived from combining information from $\langle BTT \rangle$, $\langle BTE \rangle$, and $\langle BEE \rangle$ (Shiraishi et al. 2011) using a newly developed full sky framework (Duivenvoorden et al. in prep.). The forecasts assume $r = 0$, i.e., the covariance contains only B -mode noise and no signal. For non-zero values of r , constraints will weaken due to the extra variance (see, e.g., Abazajian et al. 2016). We find

$$\begin{aligned} \sigma(f_{\text{NL}}^{\text{local}}, \langle\gamma\zeta\zeta\rangle) &= 2, & \text{SO Baseline} \\ \sigma(f_{\text{NL}}^{\text{equil}}, \langle\gamma\zeta\zeta\rangle) &= 13, \\ \sigma(f_{\text{NL}}^{\text{orthog}}, \langle\gamma\zeta\zeta\rangle) &= 6, \end{aligned} \quad (22)$$

for $r = 0$. These would improve current constraints by more than an order of magnitude.

7. SUNYAEV–ZEL’DOVICH EFFECTS

As CMB photons propagate through the universe, about 6% of them are Thomson-scattered by free electrons in the intergalactic medium (IGM) and intracluster medium (ICM), leaving a measurable imprint on the CMB temperature fluctuations. These imprints are called secondary anisotropies in the CMB and they contain a wealth of information about how structure grows in the universe and about the thermodynamic history of baryons across cosmic time. Some fraction of the Thomson-scattered photons produce Sunyaev–Zel’dovich effects (Sunyaev and Zel’dovich 1969, 1972), the focus of this section, in particular we will discuss the thermal and kinematic SZ effects. The improvements in sensitivity and frequency coverage provided by SO will greatly contribute to our understanding of the growth of structure and baryonic physics in the late-time universe, through improved measurements of SZ.

In this section we introduce the SZ effects, then forecast cosmological constraints from cluster counts (Sec. 7.1) and from the thermal SZ power spectrum (Sec. 7.2). We show how well feedback efficiency and non-thermal pressure support can be constrained from both SZ effects (Sec. 7.3). We then forecast how the kinematic SZ effect can be used to constrain the growth of structure (Sec. 7.4), primordial non-Gaussianity (Sec. 7.5), and reionization properties (Sec. 7.6).

The tSZ effect is the increase in energy of CMB photons due to scattering off hot electrons. This results in a spectral distortion of the CMB blackbody that corresponds to a decrement in CMB temperature at frequencies below 217 GHz and an increment at frequencies above. At a given frequency, ν , the temperature shift due to the tSZ effect is given (in the non-relativistic limit) by

$$\left(\frac{\Delta T(\nu)}{T_{\text{CMB}}}\right)_{\text{tSZ}} = f_\nu y, \text{ where } f_\nu = x \coth(x/2) - 4. \quad (23)$$

Here, $x = h\nu/(k_B T_{\text{CMB}})$ is dimensionless, where h is the Planck constant, and k_B is the Boltzmann constant. The tSZ amplitude is proportional to the Compton- y parameter which is defined as an integral over the line of sight l of the radial electron pressure P_e

$$y(\theta) = \frac{\sigma_T}{m_e c^2} \int P_e \left(\sqrt{l^2 + d_A^2(z)|\theta|^2} \right) dl. \quad (24)$$

Here $r^2 = l^2 + d_A^2(z)|\theta|^2$, $d_A(z)$ is the angular diameter distance to redshift z , θ is the angular coordinate on the sky, and the constants c , m_e , and σ_T are the speed of light, electron mass, and Thomson cross-section respectively.

The kSZ is the Doppler shift of CMB photons Thomson-scattering off free electrons that have a non-zero peculiar velocity with respect to the CMB rest frame. This produces small shifts in the CMB temperature proportional to the radial velocity of the object, v_r , and to its optical depth, τ , with

$$\left(\frac{\Delta T}{T_{\text{CMB}}}\right)_{\text{kSZ}} = -\tau(\theta) \frac{v_r}{c}. \quad (25)$$

This shift preserves the blackbody spectrum of the CMB to first order, and therefore is independent of frequency in thermodynamic units. The optical depth is defined as

an integral along the line of sight of the electron density n_e ,

$$\tau(\theta) = \sigma_T \int n_e \left(\sqrt{l^2 + d_A^2(z)|\theta|^2} \right) dl. \quad (26)$$

As shown in Eqs. 24–26, both tSZ and kSZ contain information about the thermodynamic properties of the IGM and ICM since their magnitudes are proportional to the integrated electron pressure (tSZ) and momentum (kSZ) along the line of sight. For ensemble statistics of clusters or galaxies the tSZ and kSZ effects contain cosmological information as they depend on the abundance of clusters or the velocity correlation function. In the following subsections we explore some of the information that we can extract from the anticipated SO SZ measurements:

- Cosmological parameters from the abundance of tSZ-detected clusters and statistics of component-separated tSZ maps.
- Thermodynamic properties of galaxies, groups, and clusters from combined tSZ and kSZ cross-correlation measurements.
- Measurements of peculiar velocities, which are powerful cosmological probes on large scales, through the kSZ effect.
- Patchy reionization which imprints the CMB through higher order moments of the kSZ effect.

7.1. Cosmology from tSZ cluster counts

Galaxy clusters can be identified across the electromagnetic spectrum, from microwave to X-ray energies. The tSZ effect is emerging as a powerful tool to find and count galaxy clusters. Among the many ways to find clusters, the tSZ effect is unique because the detection efficiency is nearly independent of redshift as long as the beam size is about arcminute scale. Measuring cluster abundances as a function of redshift allows us to probe the physical parameters that govern the growth of structure, including the sum of neutrino masses and the dark energy equation of state. Tests of dark energy and gravity can be sharpened by distinguishing geometric information (via the distance-redshift relation) from growth of structure. Cluster abundances and power spectrum observables (see Sec. 7.2) contain a combination of both: these can be distinguished via forward modeling, or using techniques to separate information on geometry and growth relative to a fiducial model.

The ability to use cluster abundances to constrain cosmological parameters is limited by uncertainties in the observable-to-mass scaling relation (e.g., Vikhlinin et al. 2009; Vanderlinde et al. 2010; Sehgal et al. 2011; Benson et al. 2013; Hasselfield et al. 2013b; Planck Collaboration 2014c; Mantz et al. 2014; Planck Collaboration 2016j; Mantz et al. 2015; de Haan et al. 2016). An accurate and precise calibration of the observable-to-mass relation is therefore essential for any future cosmological constraint from clusters. SZ-selected cluster samples have well-behaved selection functions that make it straightforward to calibrate observable-to-mass relations and constrain cosmological parameters.

We forecast cluster abundances, and associated cosmological parameters, following previous methods (Louis

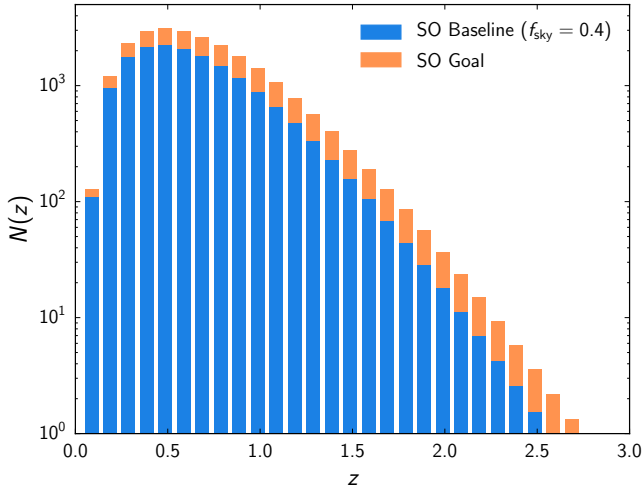


Figure 33. The forecast SZ cluster abundances as a function of redshift for the SO baseline and goal configurations with $f_{\text{sky}} = 0.4$ in bins of redshift with width $\Delta z = 0.1$ and a $S/N > 5$. We forecast approximately 16,000 clusters with baseline noise levels and approximately 24,000 clusters with the goal noise levels.

and Alonso 2017; Madhavacheril et al. 2017). The details of the methods and assumptions we use are described in Madhavacheril et al. (2017), which include a matched filter technique that exploits the unique spectral shape of the tSZ signal (Herranz et al. 2002; Melin et al. 2006) and empirical calibrations of the tSZ signal-to-mass relations via optical weak lensing and CMB halo lensing. We do not use the component-separated noise curves from Sec. 2.5.1, but instead apply our method directly to the per-frequency noise curves described in Sec. 2. We use these to compute the noise levels obtained by the matched filter technique, which provides the cluster selection function.

We include additional noise from the following CMB secondary anisotropies in the matched filter: a Poisson radio point source term, a Poisson and clustered term for the CIB, the kSZ signal, the unresolved tSZ signal, and the tSZ-CIB cross-correlation term. We estimate that half of the total tSZ auto-spectrum power is coming from clusters with masses $\sim 10^{14} M_{\odot}$ (e.g., Komatsu and Seljak 2002; Trac et al. 2011; Battaglia et al. 2012), which are expected to be detected by SO (see Fig. 33). Therefore, when we model the unresolved tSZ contribution, we reduce the amplitude of the auto-spectrum power to account for the contribution from these clusters, for the purposes of additional secondary anisotropy noise. We use the functional forms and parameters for these secondary anisotropies presented in Dunkley et al. (2013). This foreground model is consistent with the model used in Sec. 2.

In Fig. 33 we show the number of clusters expected to be detected as a function of redshift for the SO baseline and goal configurations with the value of $f_{\text{sky}} = 0.4$ in bins of redshift with width $\Delta z = 0.1$ and a $S/N > 5$. With baseline noise levels and $f_{\text{sky}} = 0.4$, we forecast approximately 16,000 clusters; with goal noise levels we forecast approximately 24,000 clusters. This is roughly an order of magnitude more SZ detected clusters than the current samples. We find that more clusters are found with larger f_{sky} for fixed total observing time. In addition to cosmological constraints, this sample of

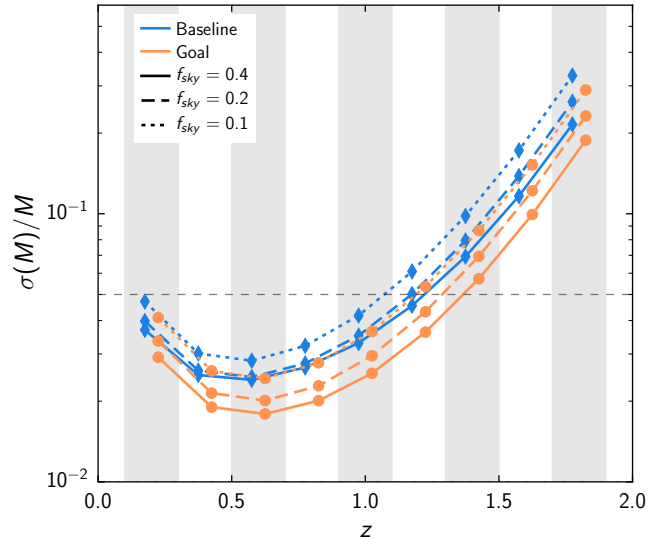


Figure 34. The relative mass calibration uncertainty from CMB halo lensing for each redshift bin ($\Delta z = 0.2$) of the SZ sample for various configurations of SO. Only the uncertainty on the stacked mass in the $1.5 \times 10^{14} < M/M_{\odot} < 2.5 \times 10^{14}$ bin is shown here. Constraints on individual clusters would be larger by a factor of \sqrt{N} for N clusters in a bin.

galaxy clusters obtained by SO will provide the greater astronomical community with a homogeneous and well-defined catalog for follow-up cluster studies out to high redshifts. Such a sample will be critical for studying the impact of over-dense environment on galaxy formation at the peak of the star-formation history in the universe.

For the calibration of the SZ signal using optical weak lensing, we compute the shape noise assuming that a three-year LSST survey will cover the SO survey area, as described in Sec. 2.3. In this forecast we make slightly different assumptions to the gold sample described in Sec. 2.6, by assuming 20 galaxies per square arcminute with the dN_g/dz from Oguri and Hamana (2011),

$$\frac{dN_g}{dz} = \frac{z^2}{2z_0^3} \exp\left(-\frac{z}{z_0}\right), \quad (27)$$

where $z_0 = 1/3$ that corresponds to the mean redshift $z_m = 1$. The constraining power of optical weak-lensing will be limited at cluster redshifts above $z \sim 2$ and conservatively $z \gtrsim 1.5$, due the lack of enough lensed galaxies behind the clusters and the large photometric uncertainties of source galaxies. For higher redshift halos we consider CMB halo lensing calibration and follow the methods outlined in Sec. 5.4. In Fig. 34 we show the relative error on the cluster mass for the $1.5 \times 10^{14} < M/M_{\odot} < 2.5 \times 10^{14}$ mass bin of the SO SZ sample as a function of redshift bin for the baseline and goal configurations with various f_{sky} we considered. We obtain the smallest errors with $f_{\text{sky}} = 0.4$. Additionally, we assume that LSST will confirm and provide redshifts for all the clusters found by SO for $z \lesssim 1.5$ clusters, the remaining clusters will require pointed, near-IR follow-up observations.

For the forecasts of cosmological parameters, our fiducial model includes the same nuisance parameters for the observable-to-mass scaling relation as Madhavacheril et al. (2017), Λ CDM cosmological parameters, and the

specified extensions to this model, like the sum of neutrino masses. We include a prior on τ and *Planck* primary CMB observations as described in Sec. 2, in addition to SO primary lensed two-point CMB *TT/EE/TE*. There are no priors on the 7 observable-to-mass scaling relation parameters and no systematic floors applied to the weak-lensing calibration of observable-to-mass scaling relation parameters. A systematic that we will address in future work is how the uncertainty in the mass function will impact our forecasts (Shimon et al. 2011).

7.1.1. Neutrino mass and dark energy

In addition to Λ CDM parameters, here we vary Σm_ν when constraining neutrino mass, and either w_0 and w_a or w_0 , w_a and Σm_ν when constraining a time-dependent dark energy equation of state $w(a) = w_0 + w_a(1 - a)$ for scale factor a . For the dark energy equation of state parameters w_0 and w_a , we use the Parameterized post-Friedmann dark energy model implemented in CAMB (Hu and Sawicki 2007; Hu 2008; Fang et al. 2008b,a). For $f_{\text{sky}} = 0.4$ and SO Baseline we forecast for neutrino mass

$$\sigma(\Sigma m_\nu) = 27 \text{ meV} \quad \Lambda\text{CDM} + \Sigma m_\nu \quad (28)$$

and for the dark energy equation of state

$$\begin{aligned} \sigma(w_0) &= 0.06, & \Lambda\text{CDM} + w_0 + w_a \\ \sigma(w_a) &= 0.20, \end{aligned} \quad (29)$$

$$\begin{aligned} \sigma(w_0) &= 0.08, & \Lambda\text{CDM} + w_0 + w_a + \Sigma m_\nu \\ \sigma(w_a) &= 0.32, \end{aligned} \quad (30)$$

with $\sigma(\Sigma m_\nu) = 25 \text{ meV}$, $\sigma(w_0) = 0.06$ and $\sigma(w_a) = 0.07$ for Goal noise for the above respective cases. Larger f_{sky} provides better constraints. For example, the $\sigma(\Sigma m_\nu) = 27 \text{ meV}$ baseline constraint for $f_{\text{sky}} = 0.4$ degrades to $\sigma(\Sigma m_\nu) = 35 \text{ meV}$ for $f_{\text{sky}} = 0.1$. Excluding SO primary lensed two-point CMB *TT/EE/TE* information degrades these constraints slightly, we get $\sigma(w_0) = 0.08$ for $f_{\text{sky}} = 0.4$ baseline and $\Lambda\text{CDM} + w_0 + w_a$.

7.1.2. Amplitude of structure: $\sigma_8(z)$

In Fig. 35, we forecast constraints on the growth of structure as a function of redshift, parametrized by the amplitude of matter fluctuations, $\sigma_8(z)$. We consider five tomographic redshift bins ($z = 0-0.5$, $0.5-1$, $1-1.5$, $1.5-2$, $2-3$) and marginalize over ΛCDM cosmological parameters and the same scaling relation nuisance parameters as above. For the mass calibration of SZ clusters, we use CMB halo lensing calibration, which allows us to push to higher redshift than the optical weak lensing calibration. The forecast constraints on $\sigma_8(z)$ for the redshift bins $z=1-2$ and $z=2-3$ are complementary to the constraints shown in Sec. 5.3.1 using the SO lensing signal in combination with galaxy clustering.

7.2. Neutrino mass from tSZ power spectrum

While the number counts of tSZ-detected galaxy clusters contain substantial cosmological information, further constraints can also be extracted from statistical analyses of the tSZ signal in component-separated y -maps (or, in some cases, appropriately filtered single-frequency CMB maps). While many statistics have been explored (Komatsu and Seljak 2002; Rubiño-Martín and

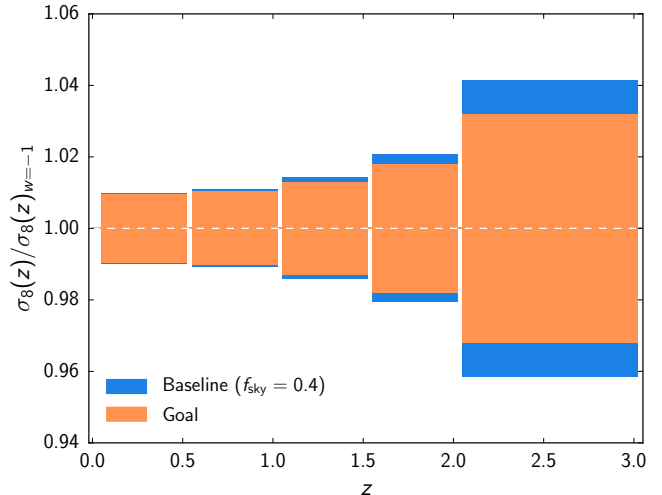


Figure 35. The uncertainty on $\sigma_8(z)$ for various redshift bins obtained from the abundances of SO-detected SZ clusters calibrated using CMB halo lensing.

Sunyaev 2003; Wilson et al. 2012; Bhattacharya et al. 2012; Hill and Sherwin 2013; Crawford et al. 2014; Hill et al. 2014; Hill and Spergel 2014; Planck Collaboration 2014d, 2016h), we focus for simplicity on the tSZ power spectrum here, leaving higher-order statistics to future work.²⁷ The tSZ power spectrum has long been recognized as a sensitive probe of cosmological and astrophysical parameters, particularly σ_8 (Komatsu and Seljak 2002; Hill and Pajer 2013; Planck Collaboration 2014d, 2016h; Horowitz and Seljak 2017; Bolliet et al. 2018).

Extracting the Compton- y map: With sufficient multi-frequency coverage, it is possible to apply component separation methods to extract maps of the Compton- y signal over large sky areas using the known tSZ spectral function, as has been possible recently for the first time with *Planck* (Planck Collaboration 2014d; Hill and Spergel 2014; Planck Collaboration 2016h; Khatri 2016). In Sec. 2.5.2, we used constrained harmonic-space ILC methods to obtain component-separated noise curves for Compton- y reconstruction.

In Fig. 36, we show the post-component-separation tSZ noise for the SO LAT in combination with *Planck* (30–353 GHz), analogous to the CMB temperature and E -mode polarization noise curves shown in Fig. 5. The figure shows the results for both the baseline and goal SO LAT noise levels, as well as various foreground-deprojection options in the constrained harmonic-space ILC used to obtain the noise curves. The standard ILC case agrees precisely with the CMB-deprojection case at low- ℓ , where the CMB is the dominant contaminant, and with the CIB-deprojection case at high- ℓ , where the CIB is the dominant contaminant. The CMB temperature acoustic oscillations can be seen in the tSZ noise for all cases in which the CMB is not explicitly deprojected. Finally, one can also clearly see the transition between the regime in which the *Planck* channels dominate

²⁷ Also note that as the threshold for individual tSZ detections moves to lower masses and higher redshifts, the detected cluster catalog will contain progressively more of the information in higher-order statistics.

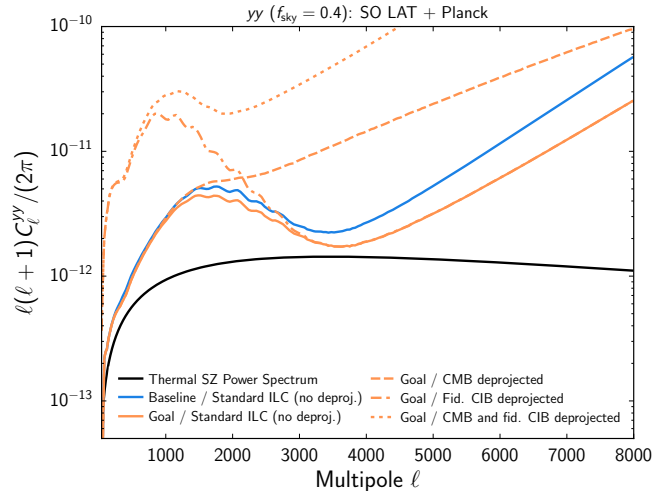


Figure 36. Post-component-separation noise for tSZ reconstruction with SO LAT and *Planck*, for a wide survey with $f_{\text{sky}} = 0.4$. The noise curves are derived via the methodology described in Sec. 2.5.1. The solid black curve shows the expected tSZ power spectrum signal. The solid blue (orange) curve shows the tSZ reconstruction noise for the baseline (goal) SO LAT noise levels. The other orange curves show the tSZ reconstruction noise for various assumptions about additional foreground deprojection in the constrained ILC formalism (see the text for further discussion). The increase in the noise curves at $\ell \approx 1000$ – 1500 is due to the transition from the *Planck*-dominated to SO-dominated regimes (note that atmospheric noise is large for the SO LAT at low- ℓ).

the reconstruction at low- ℓ and that in which the SO channels dominate at high- ℓ (note that low- ℓ modes in SO LAT temperature are noisy due to the atmosphere), with a bump in the effective noise at $\ell \approx 1000$ – 1500 between the two.

Cosmological parameter forecast method: We use these noise curves to forecast cosmological parameter constraints from the tSZ power spectrum, focusing on Σm_ν . Following Sec. 2, we also include primary CMB power spectrum information from *Planck* and SO, as well as information from anticipated DESI BAO measurements. Our fiducial model includes Λ CDM parameters (in addition to Σm_ν) and three parameters describing the gas physics of the intracluster medium: P_0 , which represents the overall normalization of the $P(M, z)$ relation (where P is gas pressure); β_0 , which denotes the normalization of the relation between the outer slope of the pressure profile and the halo mass (and redshift); and α_M , which is the power-law slope of the mass dependence in the $P(M, z)$ relation. The exact form of the $P(M, z)$ relation used here can be found in Battaglia et al. (2012).

We adopt values for the gas physics parameters drawn from cosmological hydrodynamics simulations incorporating AGN feedback, supernova feedback, and other sub-grid processes (Battaglia et al. 2010, 2012). We impose priors on the gas physics parameters to account for information obtained from studies of individually detected objects. These include a 1% prior on P_0 (which is feasible when folding in all expected weak lensing constraints on the detected clusters – see Sec. 7.1), a 10% prior on β_0 , and a 10% prior on α_M . We comment on the influence of these priors below.

In addition to the Gaussian errors due to cosmic variance and the component-separated noise curves

Table 7

Thermal SZ power spectrum (PS) forecasts for the SO LAT, in combination with *Planck*, for a variety of LAT configurations and foreground cleaning assumptions. Expected tSZ PS S/N and constraints on the sum of the neutrino masses are given.

SO LAT configuration	tSZ PS S/N	$\sigma(\Sigma m_\nu)$ [meV]
SO Baseline ($f_{\text{sky}} = 0.1$)	140	40
SO Baseline ($f_{\text{sky}} = 0.2$)	180	38
SO Baseline ($f_{\text{sky}} = 0.4$)	220	36
SO Goal ($f_{\text{sky}} = 0.1$)	160	39
SO Goal ($f_{\text{sky}} = 0.2$)	200	37
SO Goal ($f_{\text{sky}} = 0.4$)	250	35
SO Goal ($f_{\text{sky}} = 0.4$, Deproj-1)	140	36
SO Goal ($f_{\text{sky}} = 0.4$, Deproj-2)	250	35
SO Goal ($f_{\text{sky}} = 0.4$, Deproj-3)	60	43

described earlier, we also include the non-Gaussian error due to the tSZ trispectrum (Komatsu and Seljak 2002; Shaw et al. 2009; Hill and Pajer 2013; Horowitz and Seljak 2017). The non-Gaussian error dominates the error budget at low- to moderate- ℓ . While this contribution can be suppressed by masking nearby, massive clusters, we do not consider such complexities here. In addition, we do not vary the trispectrum when varying parameters in the Fisher analysis below, i.e., we compute it only for the fiducial model.

Forecast S/N of tSZ power spectrum: We forecast that the tSZ power spectrum will be detected at high S/N by the SO LAT survey combined with *Planck*, reaching $S/N \approx 250$ for a wide survey ($f_{\text{sky}} = 0.4$) with goal noise levels. Note that Fig. 36 shows the noise per mode; the high S/N is obtained due to measuring a large number of modes, particularly at high- ℓ . We give the expected S/N values for various survey choices and foreground cleaning methods in Table 7, with the Standard ILC method used unless stated. The alternative cleaning methods were described in Sec. 2, with Deproj-1 projecting out the CMB, Deproj-2 the CIB (assuming a fiducial CIB SED), and Deproj-3 both the CMB and CIB. We also include the tSZ trispectrum contribution to the errors when computing the S/N .

Neutrino mass: Table 7 also shows the marginalized constraints on Σm_ν . The tSZ power spectrum is expected to yield constraints on Σm_ν that are competitive with those from cluster counts, with $\sigma(\Sigma m_\nu) = 35$ meV in the best case. The Σm_ν results are not highly sensitive to the gas physics priors; if $\sigma(P_0)$ is increased to 0.03 (i.e., by a factor of three), then we find $\sigma(\Sigma m_\nu) = 38$ meV in the best case, i.e., a very small increase.

We conclude that the tSZ power spectrum should be a useful source of cosmological information for SO, providing an additional independent route to estimating the neutrino mass and other cosmological parameters. Nevertheless, it is possible that unforeseen difficulties could arise. For example, the small-scale component separation could be more challenging than expected due to decorrelation in the CIB across frequencies at high- ℓ , which is poorly constrained at present. Additional gas physics parameters may also be needed, beyond the three-parameter model used here. However, our analysis is conservative in that we have not attempted to

combine the information in all tSZ probes, nor have we considered higher-order tSZ statistics. Since the populations of objects sourcing these statistics are different (the tSZ power spectrum receives contributions from lower-mass clusters and other structures that are not part of the number count analysis of massive galaxy clusters), combining the statistics will yield improvements in cosmological parameters (e.g., Hill and Sherwin 2013; Bhat-tacharya et al. 2012; Hill et al. 2014; Salvati et al. 2018; Hurier and Lacasa 2017). We leave detailed exploration of these avenues for future work.

7.3. Feedback efficiency and non-thermal pressure support

Star formation in galaxies is known to be inefficient: less than 10% of the available gas is ever turned into stars (e.g., Fukugita and Peebles 2004; Gallazzi et al. 2008, and references therein). This implies that there must be powerful feedback processes that prevent gas from efficiently cooling and forming stars. The conventional theory is that feedback processes that arise from star formation, supernovae, and active galactic nuclei (AGN), inject energy into the IGM and ICM arresting efficient star-formation and changing both the density and temperature of the gas. In particular it is thought such feedback can alter the gas density profile significantly, moving large amounts of it to the outskirts and causing the well-known ‘missing baryon problem’. Forms of non-thermal pressure support are also provided to the IGM and ICM through such processes like bulk motions within the gas and turbulence.

Cross-correlations of the thermal pressure of the gas, through the tSZ effect, with the gas density, through the kSZ effect, can trace the baryons out to the outskirts of galaxies and clusters, constrain the amount of non-thermal pressure support, and measure the amount of energy injected by feedback processes. The tSZ and kSZ measurements are supplemented with halo mass estimates obtained using weak lensing. Here we follow the formalism of Battaglia et al. (2017), based on a semi-analytical model by Ostriker et al. (2005), and show forecasts for the efficiency of energy injection by feedback processes, ϵ , defined in terms of the stellar mass M_* as $E_{\text{feedback}} = \epsilon M_* c^2$, and the fraction of non-thermal pressure, α . The kSZ analysis closely follows the method outlined in Schaan et al. (2016).

We consider the LRG catalog of the upcoming DESI experiment (Font-Ribera et al. 2014) as providing the target galaxies together with spectroscopic redshifts. In practice this analysis is not restricted to an LRG galaxy sample and can also use other extragalactic catalogs, including quasars and emission-line galaxies. Our forecasts are shown in Fig. 37, and we find typical constraints

$$\begin{aligned} \sigma(\epsilon)/\epsilon &= 2\% & \text{SO Baseline,} \\ \sigma(\alpha)/\alpha &= 6\% & \text{SO Baseline,} \end{aligned} \quad (31)$$

from $z = 0.2$ to 0.8 . These properties are currently only constrained at the 50–100% level from existing SZ information.

The large SO signal-to-noise anticipated on these properties will allow us to study the redshift and mass dependence of the signal, yielding important information about galaxy formation and evolution through cosmic

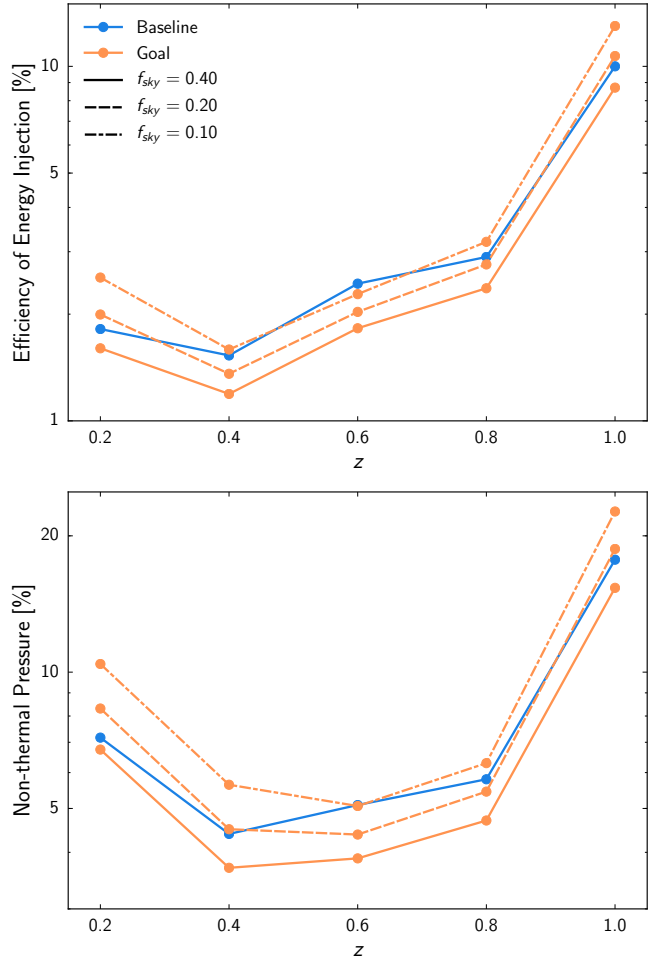


Figure 37. Forecast 1σ uncertainties on the feedback efficiency, ϵ , (top) and the non-thermal pressure support, α , (bottom) using SO combined with DESI Luminous Red Galaxies, through cross correlating the thermal and kinematic Sunyaev–Zel’dovich effects. Different colors distinguish between baseline and goal sensitivities and different line styles show the impact of different sky coverages.

time. Moreover it will help quantify the size of baryon effects in weak lensing, one of the main systematic effects of future lensing surveys (Semboloni et al. 2011; Eifler et al. 2015).

While working with a spectroscopic catalog is desirable, strong constraints on the baryon abundance and distribution can also be obtained in the absence of spectroscopic redshifts. As proposed in Doré et al. (2004) and demonstrated in Hill et al. (2016) and Ferraro et al. (2016), cross-correlating a foreground-reduced, filtered, and squared CMB temperature map with tracer galaxies is an effective probe of the baryons through the kSZ effect. Combining SO with LSST, we expect a statistical $S/N \gtrsim 100$ on the kSZ effect through this estimator (Ferraro et al. 2016). Imperfect foreground removal may ultimately be the limiting factor of this method, which nonetheless can produce tight constraints on the baryons around the galaxies in upcoming photometric catalogs.

7.4. Growth of structure from kSZ

The kSZ effect has been identified by cross-correlating CMB surveys with the positions and redshifts of clusters,

using LRGs as tracers for clusters (Hand et al. 2012; De Bernardis et al. 2017), or by using a photometrically selected cluster catalog such as redMaPPer (Rykoff et al. 2014). In this analysis we anticipate cross-correlating with LRG samples obtained from DESI, in nine redshift bins from 0.1 to 1.0.

Forecast cosmological constraints from kSZ have so far come from calculating the correlation, across a full cluster sample, between the kSZ signatures of pairs of clusters as a function of their redshift and comoving separation, known as the pairwise velocity statistic, V . To extract the pairwise velocity, V , rather than momentum, an independent measurement or estimate of each cluster’s optical depth must be established. There are a number of ways this might happen, for example through calibration with hydrodynamical simulations (Battaglia et al. 2010) or estimation with complementary datasets, such as CMB polarization measurements (Sazonov and Sunyaev 1999; Louis et al. 2017). Uncertainties in the determination of the cluster optical depth are included in the forecasting by marginalizing over a nuisance parameter, independently in each redshift bin, as in Mueller et al. (2015), that scales the amplitude of the pairwise velocity in each redshift bin, $\hat{V}(z) = b_{\tau_c}(z)V(z)$. In this forecast we consider two cases: a conservative one in which no knowledge of the optical depth is assumed, in which we fully marginalize over each $b_{\tau_c}(z)$, and a case in which we assume cluster optical depths can be measured to 10% accuracy in each redshift bin, by imposing a prior on the nuisance parameters.

In the kSZ Fisher matrices, we marginalize over Λ CDM cosmological parameters, and include nuisance parameters, $b_{\tau_c}(z)$, and the logarithmic growth rate, $f_g(z)$, as independent parameters in each of the nine redshift bins. We use the same foreground cleaning as in Sec. 7.3 for the baseline and goal SO configurations. This foreground cleaning yields a resultant noise level of $9.89 \mu\text{K-arcmin}$, with only a small difference for the baseline and goal SO noise levels. We consider two survey areas of 4,000 and 9,000 square degrees and the achieved area will depend on the overlap between the SO and DESI surveys.

We estimate the Fisher matrix for the kSZ signal, and combine it with the Fisher matrix that includes primary CMB constraints and the forecast SO lensing constraints, which provides complementary constraints on the Λ CDM parameters. Figure 38 shows the potential cosmological constraining power from combining pairwise velocity measurements of clusters identified in the SO survey with CMB lensing information. We project

$$\frac{\Delta(\sigma_8 f_g)}{\sigma_8 f_g} = 0.1 \quad \text{SO Baseline} \quad (32)$$

over a broad redshift range between $z = 0.1$ and $z = 1.0$. If we can avoid marginalizing over the optical depth, using for example an external measurement on the optical depth, we would improve this measurement by a factor of about three. Increasing the overlap area with DESI would also be beneficial in this case. Even with marginalization over the optical depth, we forecast improvement over current constraints for $\Delta(\sigma_8 f_g)/\sigma_8 f_g$ (see Fig. 38, green line). With a much better external constraint on the optical depth the $\Delta(\sigma_8 f_g)/\sigma_8 f_g$ constraints becomes complementary to the forecast constraints from DESI.

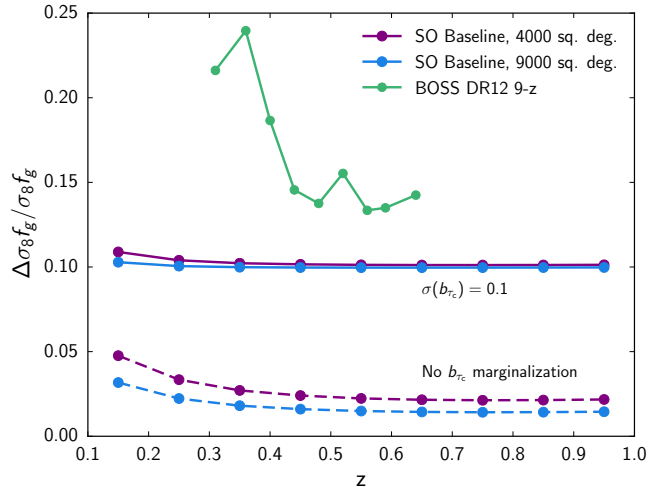


Figure 38. Predictions for SO cluster pairwise kSZ measurements in combination with lensing: fractional 1σ errors on the logarithmic growth rate, $f_g = d \ln \delta / d \ln a$, for large scale structure. We assume two different survey areas, 4,000 square degrees (purple) and 9,000 square degrees (blue, nominal), for SO baseline noise levels and foregrounds, and compared it with current limits from BOSS (green; Alam et al. 2017). Constraints are shown with two different assumptions about our knowledge of the cluster optical depth, either assuming the best-case scenario where τ_c is known perfectly (no τ_c marginalization, dashed lines) or assuming a 10% prior on τ_c in each redshift bin (solid lines), that might come, for example, from combining with additional information such as CMB polarization data.

7.5. Primordial non-Gaussianity from kSZ

As described in Sec. 5.3.2, primordial non-Gaussianity can be constrained through its scale-dependent bias. Using a similar method to the approach described using lensing, we find that kSZ velocity reconstruction can be used as an alternative measurement of the unbiased large-scale density fluctuations. Small-scale kSZ fluctuations induced in the CMB temperature depend both on peculiar velocities of galaxies hosting free electrons as well as on astrophysically uncertain quantities such as the optical depth and electron pressure profile. However, the coherence of these fluctuations traces the large scale cosmic velocity field up to an overall scale-independent amplitude that encapsulates the small-scale astrophysics (Smith et al. 2018). In linear theory, valid on large scales, velocities directly trace the underlying matter density field and the growth rate. While the uncertain normalization of the velocity field makes direct inference of the growth rate or the amplitude of structure formation difficult, scale-dependent effects such as the effect of primordial non-Gaussianity on galaxy bias can be measured.

As was the case with lensing, the addition of kSZ to galaxy clustering improves the f_{NL} constraint when the galaxy clustering measurement is sample variance limited, since the scale-dependent galaxy bias can be directly measured (up to a constant) through cancellation of the sample variance by using a ratio of the measured galaxy and velocity fields (Münchmeyer et al. 2018).

We forecast how well SO temperature maps in combination with the LSST 3-year gold sample can constrain f_{NL} using galaxy clustering in combination with kSZ velocity reconstruction. We estimate the noise in the kSZ velocity reconstruction when either the SO baseline

or goal standard ILC foreground cleaned temperature maps are combined in a quadratic estimator with the LSST galaxy positions (Deutsch et al. 2018; Smith et al. 2018). This allows us to construct a Fisher matrix for the auto-spectra and cross-spectrum of the velocity reconstruction and galaxy density fields in five redshift bins (Münchmeyer et al. 2018). We find that the combination of SO kSZ and LSST clustering allow us to constrain f_{NL} to an uncertainty of $\sigma(f_{\text{NL}}) = 1$, reaching an interesting theoretical threshold for primordial non-Gaussianity.

7.6. Epoch of Reionization from kSZ

The epoch of reionization leaves several imprints on the CMB. The most prominent on small scales is due to the ‘patchy’ kSZ effect from the peculiar motion of ionized electron bubbles around the first stars and galaxies. The kSZ power spectrum has contributions from the epoch of reionization and from the ‘late-time’ kSZ (i.e., from IGM, galaxies, and clusters considered in Sec. 7.4). The amplitude of these two contributions are predicted to be comparable (e.g., Shaw et al. 2012; Mesinger et al. 2012; Battaglia et al. 2013).

If the amplitude of the late-time contribution is known, and foregrounds are effectively removed at small scales using multi-frequency analysis, it is possible to use the power spectrum to extract information about reionization. If C_ℓ^{EE} is used to estimate the CMB power in C_ℓ^{TT} , the remaining emission in the high- ℓ temperature spectrum is dominated by kSZ and can provide strong constraints on reionization (Calabrese et al. 2014).

kSZ amplitude parameter: We run a Fisher forecast for SO using baseline and goal noise levels, assuming that a patchy kSZ component from Battaglia et al. (2013) with $\mathcal{D}_{\ell=3000} = 1.4 \mu\text{K}^2$ (corresponding to a reionization scenario with fiducial duration $\Delta z_{\text{re}} = 1$ and time $z_{\text{re}} = 8$) is added to the lensed primary CMB signal, and perfect knowledge of the power spectrum of noise and residual foregrounds in the ILC-cleaned map. We then forecast the ΛCDM parameters plus a single additional patchy kSZ amplitude parameter. We impose a Gaussian prior on the late-time homogeneous contribution, bound to have $\mathcal{D}_{\ell=3000} = 1.5 \pm 0.2 \mu\text{K}^2$. This term is known at the 10% level, accounting for astrophysical and cosmological uncertainties (Shaw et al. 2012; Park et al. 2018). Additional uncertainty due to marginalization over non-kSZ foregrounds is incorporated with the Deproj-0 noise curves from Sec. 2.

The measurement of the kSZ power and the constraint on the optical depth to reionization from the *Planck* large-scale measurements (Planck Collaboration 2016; incorporated here as a $\sigma(\tau) = 0.01$ measurement) are then converted into a bound on the time and the duration of reionization (following, e.g., Calabrese et al. 2014, 2017). We forecast

$$\begin{aligned} \sigma(\Delta z_{\text{re}}) &= 0.40 && \text{SO Baseline,} \\ \sigma(\Delta z_{\text{re}}) &= 0.35 && \text{SO Goal,} \end{aligned} \quad (33)$$

predicting a significant improvement over current upper limits ($\Delta z_{\text{re}} < 2.8$ at 95% confidence when combining *Planck* and SPT data, Planck Collaboration 2016p). We note that these constraints are somewhat conservative, due to the fact that the forecasts presented throughout

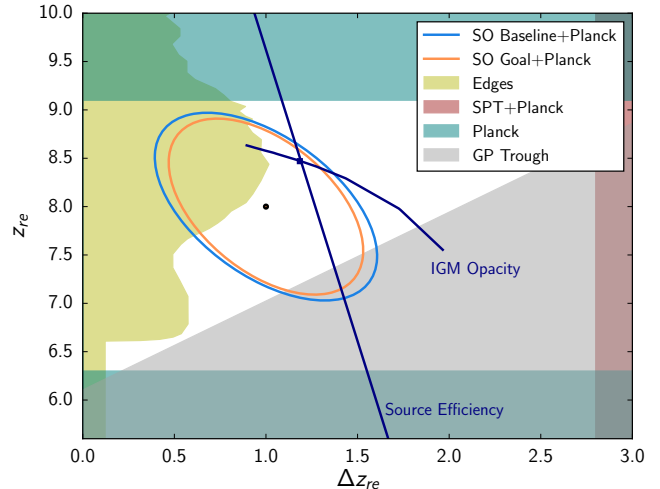


Figure 39. Summary of constraints on the redshift and duration/width of reionization. The SO forecasts are reported with 68% confidence-level contours from baseline/goal configurations in combination with *Planck* large-scale data (blue/orange). The solid navy lines show the redshift and width of reionization at constant values of the IGM opacity and source efficiency. The SO constraints on these parameters are shown in Fig. 40. The SO predictions are compared to current exclusion limits for the time of reionization from *Planck* (green band; Planck Collaboration 2018d), recent measurements of the global 21 cm signal assuming standard thermal properties (i.e., spin temperature much larger than the CMB temperature) of the IGM (yellow band; Monsalve et al. 2017), and Gunn Peterson trough from fully absorbed Lyman alpha in quasar spectra (gray band; Fan et al. 2006), and to current upper limits on the duration of reionization from *Planck* and SPT data (brown band; Planck Collaboration 2016p).

this paper assume that the maximum multipole, ℓ , in SO temperature is $\ell_{\text{max}} = 3000$. We anticipate that information from smaller scales, after foreground removal, could further increase the SO sensitivity to reionization parameters. These forecasts, alongside other current constraints on the reionization time and duration, are summarized in Fig. 39.

Ionization efficiency and mean free path: In addition to fitting for the kSZ amplitude, we can alternatively constrain physically motivated parameters directly: the ionization efficiency (or number of atoms ionized per atom in halos above the minimum mass), ζ , and the mean free path of the ionizing photons, λ_{mfp} . Since not all atoms are in these halos, the ionization efficiency by definition must be greater than unity. The rarer the halos (or equivalently the higher the minimum halo mass), the higher the required efficiency factor. We show the constraints on these parameters in Fig. 40. These constraints were obtained by simulating kSZ maps using the method described in Alvarez (2016) around a fiducial model of $(\log \lambda_{\text{mfp}}, \zeta) = (1.2, 100)$. The spectra are simulated at discrete ‘step sizes’ away from the fiducial point, and finite differencing is used to obtain the derivative of the resulting temperature power spectrum with respect to these parameters. Figure 40 also shows the corresponding errors on the width and duration of reionization, taken as the redshift at which the universe is 50% ionized, and the time between ionization fractions of 25 and 75%, respectively.

Separating kSZ components: To improve the confidence

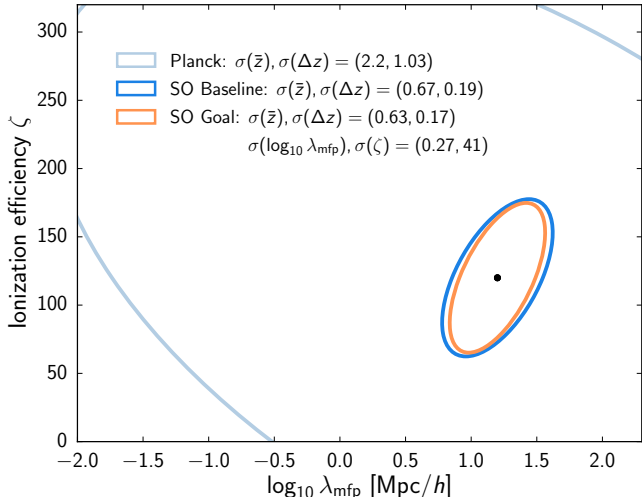


Figure 40. Forecast 1σ constraints on the ionization efficiency and mean free path of reionization for a minimum galaxy halo mass of $M_{\min} = 10^9 M_{\odot}$, and around the fiducial model $(\lambda_{\text{mfp}}, \zeta) = (16 \text{ Mpc}/h, 100)$. We assume both baseline and goal sensitivities and foreground cleaning with an $f_{\text{sky}} = 0.4$. The connection between these parameters and the redshift and duration of reionization is shown in Fig. 39.

in separating the kSZ components, there are promising prospects to use higher point functions of the temperature map to internally separate the reionization and late-time components (Smith and Ferraro 2017; Ferraro and Smith 2018). We anticipate implementing these methods on the SO data.

8. EXTRAGALACTIC SOURCES

In mapping the sky at frequencies between 30 and 280 GHz, SO will observe extragalactic sources, including active galactic nuclei (AGNs, Sec. 8.1) and dusty star-forming galaxies (DSFGs, Sec. 8.2), and transient sources such as Gamma Ray Burst (GRB) afterglows (Sec. 8.3).

8.1. Active Galactic Nuclei

SO will enable statistical studies of AGN populations with its high-sensitivity, large-sky-area maps in temperature and polarization, measured in multiple frequencies simultaneously. Such statistical studies of AGN (e.g., Murphy et al. 2010; Mocanu et al. 2013; Marsden et al. 2014; Planck Collaboration 2016; Gralla et al. in prep.) reveal their abundance, spectral energy distributions, and global polarization properties (e.g., Huffenberger et al. 2015; Bonavera et al. 2017; Datta et al. 2018). AGN samples that are selected at SO’s frequencies will be dominated by blazars with flat or falling spectra, with an increasing fraction of steep spectrum AGN at lower frequencies. Depending on modeling assumptions, and based on Tucci et al. (2011) source counts, we expect to detect 10,000–15,000 sources at flux-densities exceeding 7 mJy. This is the 5σ detection limit for the baseline SO sensitivity at 93 GHz, which is SO’s most sensitive band for sources with an AGN-like SED. A multi-frequency matched filter will find more sources. The radio source counts found by Mocanu et al. (2013) and Gralla et al. (in prep.) somewhat exceed the Tucci et al. (2011) C2Ex model used here, which may raise the actual counts above

Table 8

Number of polarized sources, N_{src} , expected above a 5σ detection limit, $S_{5\sigma}$, for the LAT with $f_{\text{sky}} = 0.4$.

ν [GHz]	$S_{5\sigma}$ [mJy]	N_{src}
27	20	80
39	10	150
93	7	270
148	10	70

our predicted level.

The SO frequency coverage will complement low-frequency radio continuum surveys (e.g., VLA/VLASS, ASKAP/EMU, MeerKAT/MIGHTEE). In addition to finding bright objects, the SO can constrain the spectral energy distributions of AGN selected at lower frequencies due to the large area of overlap with those surveys (e.g., ?). The blazars can also be variable over timescales of days to years (e.g., Chen et al. 2013; Richards et al. 2014). Because of its rapid cadence, SO will provide one of the best continuous monitors of AGN variability at any wavelength, following many thousands of AGN continuously in the mm-cm band. Studies of AGN variability can potentially constrain the evolution of ejecta using the lag in the peak emission across wavelengths.

In polarization we expect to detect as many as ~ 270 polarized radio sources at 93 GHz in a wide survey over 40% of the sky. Anticipated counts for other frequencies are shown in Table 8, based on the baseline survey properties and the methodology of Puglisi et al. (2017) that uses number counts and a log-normal model distribution of the polarization fraction.

Such a large number of blazars will enrich polarized source datasets over a wide range of frequencies, where catalogs are still poor and incomplete, and will allow high-resolution follow-up with other instruments (Partridge et al. 2017). Polarization of sources detected in the mm/sub-mm wavelengths will shed light on details of the magnetic field in unresolved regions closer to the active nucleus and to the jet.

As discussed in Sec. 4, the characterization of AGN sources’ polarized spectral and spatial distribution properties is also critical for utilizing CMB polarization measurements at small angular scales, for example in the E -mode damping tail.

8.2. Dusty star-forming galaxies

The DSFGs seen by SO will include both local galaxies ($z < 0.1$) and high redshift galaxies (roughly $2 < z < 4$), with a population of strongly lensed sources extending to well beyond this range. The strongly lensed galaxies are useful for studying properties of star formation near the nominal peak of the cosmic star formation history of the universe. They even let us access the first billion years of cosmic history (i.e., $z > 6$, Marrone et al. 2018). The spatial distribution of the matter in the lenses themselves can also be studied in extraordinary detail, enabling the detection of structures of dark matter down to small ($10^9 M_{\odot}$) scales (e.g., Hezaveh et al. 2016). These observations can provide crucial, direct information on the clumping of dark matter on scales at which cold dark matter cosmological simulations predict far more halos than are currently observed using faint galaxies as tracers. In addition to the lensed source population, some of the SO DSFG sample is expected to be

groupings of multiple galaxies that could represent the precursors to present-day galaxy clusters. On the faint end of the source population, SO is likely to observe un-lensed, intrinsically bright high-redshift dusty galaxies. Follow-up observations can differentiate these different sub-populations of DSFGs and will be crucial to realizing their scientific potential.

To predict the number of DSFGs that SO will observe, we compute confusion and detection limits analytically from source count models and power spectra, considering two Poisson point source populations (AGN, DSFGs) and other extragalactic signals (CMB, tSZ, kSZ). We also include the baseline model for atmospheric noise and instrument sensitivity. The DSFG forecasts are based on models from Béthermin et al. (2012), which include a strongly-lensed population component. Depending on modeling assumptions, in a single band SO is projected to find $\sim 8,500$ DSFGs. Given the expected DSFG SED, the optimal SO band for finding DSFGs will be the 280 GHz band, at which the 5σ sensitivity limit is expected to be ~ 26 mJy. Multi-frequency filtering will let us push to fainter source flux densities.

8.3. Transient sources

SO provides a unique opportunity to continuously survey a very wide area of the sky (40%), with a fast re-observation cadence of hours and long observing timescales of several years. The major expected source classes for SO are flares of AGN, discussed in Sec. 8.1, and the afterglows of gamma-ray bursts (GRBs), which are expected to peak at frequencies of several hundred GHz (Granot and Sari 2002) and to which SO will have particularly competitive sensitivity. Both of these source classes have expected fluctuation timescales of days to weeks, for which SO will survey an effective sky area of approximately 2 million square degrees.

The major science goal for transient sources with SO would be the identification of a GRB afterglow without the detection of accompanying gamma emission (a so-called orphan afterglow). These are a generic prediction of all GRB models, but none have yet been identified and their rate is so far unknown and subject to large uncertainties. An unexpectedly high, or low, rate of these type of objects would suggest that our ideas of the total energy budget of these objects is incorrect and impact both theories of gamma-ray bursts and models that rely on their aggregate contribution to the high-energy universe, in particular the origins of high-energy cosmic rays and the diffuse neutrino background. In standard models of GRB fireballs (Ghirlanda et al. 2014), SO will have an expected number of detections larger than one, something not yet achieved in any band.

Even more exotic transient objects include Population III star GRBs (Toma et al. 2011; Macpherson and Coward 2015), which have not yet been observed. These would be extremely high-redshift luminous objects ($z \sim 20$) and are interesting in the contexts of structure formation, star formation, and reionization. Aside from these possibilities, the transient sky in the millimeter band is nearly unexplored, with only one survey (Whitehorn et al. 2016) conducted to date covering less than 1% of the sky for one year, and there is significant discovery space available to SO as a result.

9. FORECAST SUMMARY AND CONCLUSIONS

In this final section we draw together the forecasts from the set of SO probes, summarizing our key science goals, anticipated catalogs, and additional science. These forecasts include the impact of realistic atmospheric noise, foreground contamination, and other astrophysical uncertainties. Where more than one technique is available for measuring a parameter, we show these explicitly as independent measurements, rather than combining them.

9.1. Key science targets

Our key science targets are summarized in Table 9, where we specify the 1σ forecast uncertainties on each parameter for the baseline and goal noise levels. For the baseline case, we show the forecast uncertainty as derived in the earlier sections, and also, for each case, we inflate the uncertainty by 25% (rounding up to 1 significant figure) as a proxy for additional systematic errors, to be refined in future studies. This reflects the impact of effects including, for example, beam uncertainty as described in Sec. 4.1, or bandpass uncertainty (Ward et al. 2018). As described in Sec. 3.5 for example, our imperfect knowledge of the instrument, and of additional external sources of noise, should be propagated through to our projected errors, and is the subject of our next study. For each science target we also give the current uncertainty, and specify which method is used. A key describing the methods is given in Table 10. In the following we describe each science target, focusing on the nominal baseline noise levels.

1. Primordial perturbations.

(a) Tensor-to-scalar ratio: SO aims to measure the tensor-to-scalar ratio, r , with $\sigma(r) = 0.003$ for an $r = 0$ model. This will enable at least a 3σ measurement of primordial gravitational waves if $r \geq 0.01$. If SO sees no signal, this would exclude models with $r \geq 0.01$ at more than 99% confidence. Lowering the current limit by an order of magnitude will also better constrain non-inflation models. This constraint on r will come from the large-scale B -modes measured by the SO SATs. The forecast constraints on r and the spectral index of primordial perturbations, n_s , is shown in Fig. 41.

(b) Scalar perturbations: Beyond improving the measurement of the spectral index of primordial perturbations, SO aims to estimate the primordial scalar amplitude at the half-percent level at scales ($k = 0.2/\text{Mpc}$) smaller than those accessible to the *Planck* satellite. This will test the almost-scale-invariant prediction of inflation over a wider range of scales than yet probed to this precision, and identify possible deviations from a power law that are characteristic of some alternative models for the early universe. This constraint will come from the small-scale primary CMB temperature and E -mode polarization power spectra measured by the SO LAT.

(c) Non-Gaussian perturbations: SO targets a measurement of the non-Gaussianity of the primordial perturbations at the $\sigma(f_{\text{NL}}^{\text{local}})=2$ level, halving current constraints. This constraint will be derived via two methods: (i) by correlating the CMB kinematic Sunyaev–Zel’dovich effect (derived from the temperature maps measured by the SO LAT) with the galaxy distri-

Table 9
Summary of SO key science goals^a

	Parameter	SO-Baseline ^b (no syst)	SO-Baseline ^c	SO-Goal ^d	Current ^e	Method	Sec.
Primordial perturbations	r	0.0024	0.003	0.002	0.03	BB + ext delens	3.4
	$e^{-2\tau}\mathcal{P}(k = 0.2/\text{Mpc})$	0.4%	0.5%	0.4%	3%	$TT/TE/EE$	4.2
	$f_{\text{NL}}^{\text{local}}$	1.8	3	1	5	$\kappa\kappa \times \text{LSST-LSS} + 3\text{-pt}$	5.3
		1	2	1		kSZ + LSST-LSS	7.5
Relativistic species	N_{eff}	0.055	0.07	0.05	0.2	$TT/TE/EE + \kappa\kappa$	4.1
Neutrino mass	Σm_ν	0.033	0.04	0.03	0.1	$\kappa\kappa + \text{DESI-BAO}$	5.2
		0.035	0.04	0.03		tSZ-N \times LSST-WL	7.1
		0.036	0.05	0.04		tSZ-Y + DESI-BAO	7.2
Deviations from Λ	$\sigma_8(z = 1 - 2)$	1.2%	2%	1%	7%	$\kappa\kappa + \text{LSST-LSS}$	5.3
		1.2%	2%	1%		tSZ-N \times LSST-WL	7.1
	H_0 (ΛCDM)	0.3	0.4	0.3	0.5	$TT/TE/EE + \kappa\kappa$	4.3
Galaxy evolution	η_{feedback}	2%	3%	2%	50-100%	kSZ + tSZ + DESI	7.3
	p_{nt}	6%	8%	5%	50-100%	kSZ + tSZ + DESI	7.3
Reionization	Δz	0.4	0.6	0.3	1.4	TT (kSZ)	7.6

^a All of our SO forecasts assume that SO is combined with *Planck* data.

^b This column reports forecasts from earlier sections (in some cases using 2 s.f.) and applies no additional systematic error.

^c This is the nominal forecast, increases the column (a) uncertainties by 25% as a proxy for instrument systematics, and rounds up to 1 s.f.

^d This is the goal forecast, has negligible additional systematic uncertainties, and rounds to 1 s.f.

^e Primarily from [BICEP2/Keck and Planck Collaborations 2015](#) and [Planck Collaboration 2018d](#).

Table 10
Methods used for SO forecasts

Method	Description	Section
$TT/TE/EE$	Temperature and E -mode polarization power spectra	4
BB	B -mode polarization power spectrum	3,5
$\kappa\kappa$	CMB lensing convergence power spectrum	5
3-pt	Bispectrum	6
tSZ-N	Cluster catalog	7
tSZ-N \times κ	Cluster masses calibrated using CMB lensing	5,7
tSZ-Y	tSZ Y-distortion map	7
TT (kSZ)	kSZ effect measured via the temperature power spectrum	4
ext delens	Delensing field estimated from large-scale structure surveys	3,5
tSZ-N \times LSST-WL	Cluster masses calibrated using LSST weak lensing data	7
$\kappa\kappa \times \text{LSST-LSS}$	CMB lensing correlated with galaxy density in tomographic slices from 3 years of LSST	2,5
DESI-BAO	BAO measurements from the full DESI survey	2
DESI	Galaxy positions from the full DESI survey	7

bution in tomographic redshift bins from LSST; and (ii) by correlating the CMB lensing field (derived from the temperature and polarization maps measured by the SO LAT) with the LSST galaxy distribution. An additional cross-check will come from the bispectrum estimated from the SO LAT temperature and polarization maps.

2. Effective number of relativistic species.

A universe with three neutrino species – and no additional light species – provides 3.046 effective relativistic species. SO aims to measure $\sigma(N_{\text{eff}}) = 0.07$, using the

primary CMB temperature and polarization power spectrum measured from the SO LAT, more than halving the current limit from the *Planck* satellite. $\Delta N_{\text{eff}} \geq 0.047$ is predicted for models containing additional light non-scalar particles that were in thermal equilibrium with the particles of the Standard Model at any point back to the time of reheating. SO’s target would exclude at more than 95% confidence any models with three or more such additional particles. The forecast limits are shown in Fig. 15.

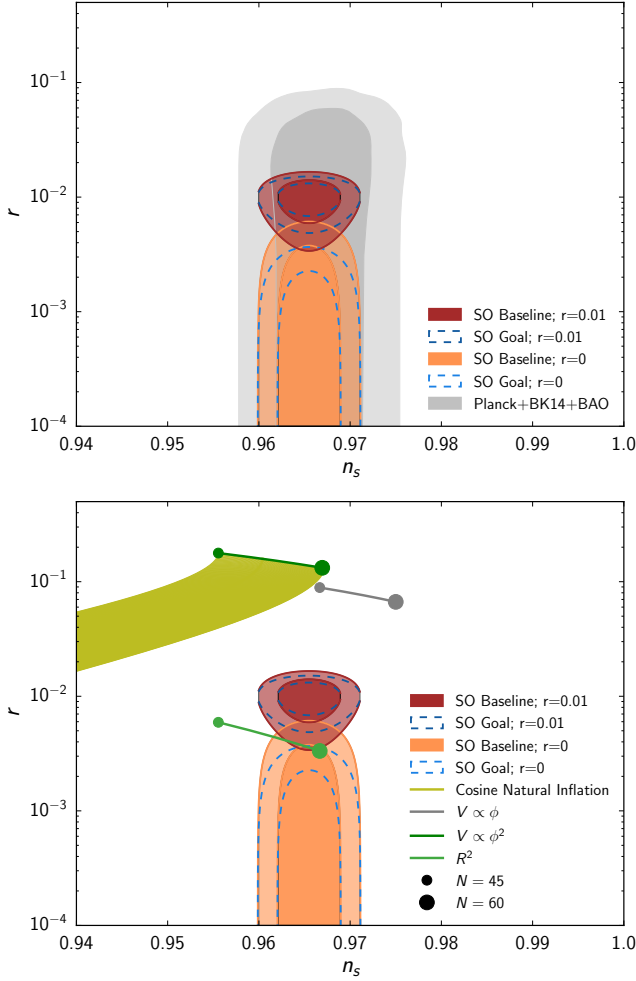


Figure 41. *Top:* Summary of SO forecasts for the primordial power spectrum parameters n_s and r for two example cases: vanishingly small primordial tensor modes and primordial perturbations with $r = 0.01$. The contours correspond to 68% and 95% confidence levels. For each model the SO baseline (goal) forecasts are shown as filled (dashed) contours. In gray we show the current most stringent constraint in this parameter space (*Planck* TT,EE,EE+lowE+lensing + BICEP2/Keck + BAO; [Planck Collaboration 2018d](#)) *Bottom:* SO forecasts (same as above) with predictions for n_s and r from some inflationary models for N e -fold in the range [45–60] (Cosine Natural inflation ([Freese et al. 1990](#)), Starobinsky (R^2) inflation ([Starobinsky 1980](#); [Starobinskij 1992](#)), and ϕ^n inflation ([Linde 1983](#); [McAllister et al. 2010](#))). For the two values of r considered, SO could exclude, or detect, classes of models that are still in agreement with current data with $r < 0.07$ (BICEP2/Keck and *Planck* Collaborations 2015; *Planck* Collaboration 2018f).

3. Neutrino mass.

The goal of SO is to measure the total mass in the three neutrino species with $\sigma(\Sigma m_\nu) = 0.04$ eV. If $\Sigma m_\nu \geq 0.1$ eV, such a measurement could give a clear indication of a non-zero mass sum. SO plans to achieve this measurement through three different methods: (i) CMB lensing from SO combined with new BAO measurements from DESI; (ii) SZ cluster counts from SO calibrated with weak lensing measurements from LSST; and (iii) thermal SZ distortion maps from SO combined with BAO measurements from DESI. The forecast constraints are shown in Fig. 42, together with current limits and anticipated limits from laboratory measurements of neutrino β decay ([KATRIN Collaboration 2005](#)). The

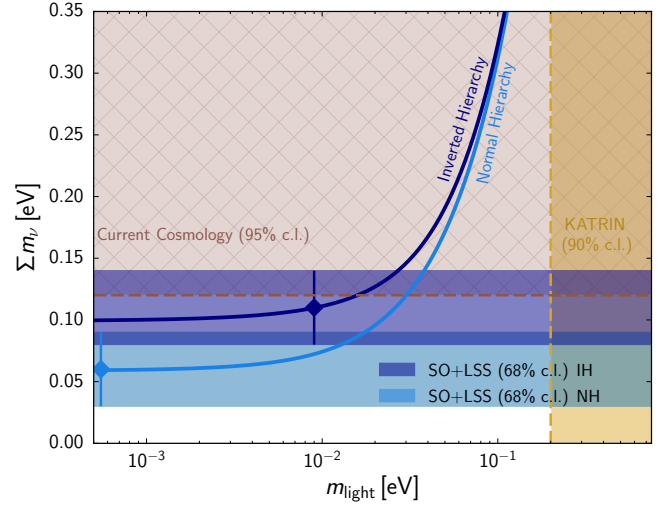


Figure 42. Summary of current limits on the neutrino mass scale, Σm_ν , and forecast sensitivity, from cosmological probes and laboratory searches. The mass sum is shown as a function of the mass of the lightest neutrino eigenstate, m_{light} , for the normal and inverted hierarchy. Current cosmological bounds (TT,TE,EE+lowE+lensing+BAO, [Planck Collaboration 2018d](#)) exclude at 95% confidence the region above the horizontal brown dashed line. The 1σ sensitivity for SO (baseline with no systematic error or goal) combined with large scale structure measurements (LSS, as described in Table 9) is shown for two example cases, enabling a 3σ measurement of Σm_ν for the minimal mass scenario for the inverted ordering. The expected sensitivity from the β -decay experiment KATRIN ([KATRIN Collaboration 2005](#)) is indicated with a vertical yellow band on the right – the projection here is done for NH, IH yields similar results with differences not visible on these scales.

legacy SO dataset could be used in combination with a future cosmic variance-limited measurement of the optical depth to reionization (from E -mode polarization, measured for example by a CMB satellite or balloon experiment), which would enable a 6σ detection of the minimal allowed mass sum within the inverted hierarchy, and a 3σ detection of the minimal mass sum within the normal hierarchy (which has $\Sigma m_\nu \geq 0.06$ eV).

4. Deviations from Λ .

(a) Amplitude of matter perturbations at $z > 1$: Upcoming optical data promise to constrain deviations from a cosmological constant at redshifts $z < 1$. SO aims to provide complementary constraints by measuring the amplitude of matter perturbations, σ_8 , out to $z = 4$ with a 2% constraint between $z = 1$ –2 (shown in Figs. 29 and 35). The matter perturbation amplitude can be obtained in three ways: (i) SZ galaxy clusters in the LAT temperature maps, calibrated with LSST weak lensing measurements; (ii) SZ galaxy clusters calibrated with SO CMB lensing measurements estimated from the LAT maps; and (iii) CMB lensing maps from the SO LAT cross-correlated with the LSST galaxy number density in tomographic redshift bins.

(b) Derived Hubble constant: SO aims to reduce the current uncertainty on the Hubble constant derived from the primary CMB within the Λ CDM model, reaching a half-percent measurement on H_0 from the LAT temperature and polarization power spectra, shown in Fig. 22. This will enhance the significance of any discrepancy in H_0 values inferred from the CMB

from Hubble diagram measurements at low redshift; a persistent discrepancy might indicate a departure from a cosmological constant, or other new physics.

5. Galaxy evolution: feedback efficiency and non-thermal pressure in massive halos.

By measuring the thermal and kinematic Sunyaev–Zel’dovich effects in massive halos, SO aims to inform and refine models of galaxy evolution. It will do so by constraining the feedback efficiency in massive galaxies, groups, and clusters, η_{feedback} to 3% uncertainty, and the degree of non-thermal pressure support, p_{nt} , to 8% uncertainty (shown in Fig. 37). No strong limits on these important aspects of galaxy formation currently exist. These constraints will be derived from the LAT temperature maps, combined with galaxy positions measured by the DESI spectroscopic survey.

6. Reionization: measurement of duration.

The reionization process is still poorly characterized. If the duration of reionization $\Delta z > 1$, SO aims to measure the average duration of reionization with a significance between 2σ and 3σ , and thus constrain models for the ionizing process. Such a measurement would be among the first to probe the properties of the first galaxies, quasars, and the intergalactic medium in the reionization epoch. This measurement is derived from the power spectra of the temperature and polarization LAT maps, since patchy reionization adds excess variance to the temperature anisotropies through the kinematic SZ effect. The forecast constraints are shown in Fig. 39.

In addition to these key science goals, SO has a set of secondary science goals that have been summarized in the earlier sections of this paper. The forecasts are collected – and rounded to one significant digit – in Table 11 for reference. These include measuring additional non-Gaussian parameters describing the primordial perturbations, probing Big Bang Nucleosynthesis by measuring the primordial helium fraction, constraining interactions between dark matter particles and baryons, constraining the mass of ultra-light-axion dark matter, measuring the dark energy equation of state to cross-check constraints from optical surveys, calibrating the shear bias for LSST, and constraining the ionization efficiency in models of reionization. The SO data will also improve limits on other speculative extensions of the standard cosmology, including primordial isocurvature perturbations, modified gravity, cosmic strings, primordial magnetic fields, and cosmic birefringence.

9.2. Legacy catalogs

In addition to the science goals, SO’s broader aim is to produce several high-level data products for use by the general astronomical community. This will include maps of the sky in temperature and polarization at 27, 39, 93, 145, 225, and 280 GHz, covering around 40% of the sky at arcminute resolution, and around 10% of the sky at degree-scale resolution and higher sensitivity. Combining these maps with data from the *Planck* satellite at large angular scales and higher frequencies, we will produce component-separated maps, including the blackbody CMB temperature and polarization, the Cosmic Infrared Background, the Compton- y parameter

from the SZ effect, and Galactic synchrotron and dust. We will also produce maps of the CMB lensing convergence and potential.

In addition, we anticipate a legacy galaxy cluster catalog of 16,000 clusters detected via the SZ effect, and a point source catalog of 15,000 AGN and 8,500 dusty star-forming galaxies. These are summarized in Table 11.

9.3. Conclusions

The Simons Observatory is due to start observations from the Atacama Desert in Chile in the early 2020s. Here we have summarized its broad science goals, and forecast its performance from a five-year survey. SO will improve measurements of the primary CMB polarization signal, and give unprecedented measurements of the secondary CMB signals including gravitational lensing and the thermal and kinematic Sunyaev–Zel’dovich effects. We will obtain new insight into a wide range of cosmological physics, from primordial tensor perturbations to feedback efficiency in galaxy formation. We have determined that the optimal configuration for SO to achieve its goals is the combination of a large 6-m telescope surveying $\approx 40\%$ of the sky that overlaps with optical surveys, and a set of small 0.5-m telescopes optimally designed to measure the largest angular scales attainable from Chile, surveying $\approx 10\%$ of the sky.

SO will attain unprecedented levels of statistical uncertainty in its measurements. This statistical power can be fully exploited only if systematic errors are controlled sufficiently. Many known systematics in the current generation of experiments must be improved to attain the ambitious scientific goals presented here, and this requirement drives all aspects of the SO design. In the science projections presented here, systematic effects are modeled in a crude way by modestly inflating the baseline statistical error bars. The goal specifications assume that all systematics in total will be subdominant to statistical errors. The SO collaboration is undertaking an instrument modeling effort aimed at understanding the science impact of a range of possible systematic errors, and setting systematic error tolerances needed to achieve the ambitious science goals outlined here. Results, which we hope will be broadly useful for all future microwave background experiments, will be described in future papers.

This work was supported in part by a grant from the Simons Foundation (Award #457687, B.K.). DA acknowledges support from the Becroft trust and from STFC through an Ernest Rutherford Fellowship, grant reference ST/P004474/1. CB, NK, FP, DP acknowledge support from the COSMOS Network (cosmosnet.it) from the Italian Space Agency (ASI), from the RADIOFOREGROUNDS project, funded by the European Commissions H2020 Research Infrastructures under the Grant Agreement 687312, and from the INDARK initiative from the Italian Institute for Nuclear Physics (INFN). DB thanks support from grant ALMA-CONICYT 31140004. EC is supported by a STFC Ernest Rutherford Fellowship ST/M004856/2. AC acknowledges support from the UK Science and Technology Facilities Council (grant

Table 11
Catalogs and additional science from SO

	Parameter	SO-Baseline	Method	Section
Legacy catalogs	SZ clusters	20,000	tSZ	7
	AGN	10,000	Sources	8
	Polarized AGN	300	Sources	8
	Dusty star-forming galaxies	10,000	Sources	8
Primordial perturbations	f_{NL} (equilateral)	30	T/E	6
	f_{NL} (orthogonal)	10		6
	n_s	0.002	$TT/TE/EE + \kappa\kappa$	2
Big bang nucleosynthesis	Y_P (varying N_{eff})	0.007	$TT/TE/EE + \kappa\kappa$	4
	$\Omega_b h^2$ (Λ CDM)	0.00005	$TT/TE/EE + \kappa\kappa$	2
Dark matter	DM–baryon interaction (σ_p , MeV)	5×10^{-27}	$TT/TE/EE + \kappa\kappa$	4
	UL axion fraction (Ω_a/Ω_d , $m_a = 10^{-26}$ eV)	0.005	$TT/TE/EE + \kappa\kappa$	4
Dark energy or modified gravity	w_0	0.06	tSZ + LSST	7
	w_a	0.2	tSZ + LSST	7
	Growth rate ($\Delta(\sigma_8 f_g)/\sigma_8 f_g$)	0.1	kSZ + DESI	7
Shear bias calibration	$m_{z=1}$	0.007	$\kappa\kappa$ +LSST	5
Reionization	$\log_{10}(\lambda_{\text{mfp}})$	0.3	$TT/TE/EE$ (kSZ)	7
	Ionization efficiency (ζ)	40	$TT/TE/EE$ (kSZ)	7

Note. — This table includes science forecast for SO thus far, described in earlier sections of this paper.

number ST/N000927/1). JC is supported by the Royal Society as a Royal Society University Research Fellow at the University of Manchester, UK. DC acknowledges the financial assistance of the South African SKA Project (SKA SA). Canadian co-authors acknowledge support from the Natural Sciences and Engineering Research Council of Canada. JE and RSt acknowledge support from French National Research Agency (ANR) through project BxB no. ANR-17-CE31-0022. GF acknowledges the support of the CNES postdoctoral fellowship. AD, KF, MG, JEG, and SV acknowledge support by the Vetenskapsradet (Swedish Research Council) through contract No. 638-2013-8993 and the Oskar Klein Centre for Cosmoparticle Physics at Stockholm University. Further we acknowledge support from DoE grant DE-SC007859 and the LCTP at the University of Michigan. VG gratefully acknowledges the support of the Eric Schmidt Fellowship at the Institute for Advanced Study. JCH is supported by the Friends of the Institute for Advanced Study. MHi acknowledges support from the NRF and SKA-SA. The Dunlap Institute is funded through an endowment established by the David Dunlap family and the University of Toronto. The authors at the University of Toronto acknowledge that the land on which the University of Toronto is built is the traditional territory of the Haudenosaunee, and most recently, the territory of the Mississaugas of the New Credit First Nation. They are grateful to have the opportunity to work in the community, on this territory. KH acknowledges support from NASA grant ATP-NNX17AF87G. We acknowledge support from the JSPS KAKENHI Grant Number JP16K21744, JP17H06134, and JP17K14272. AK and KK acknowledges the support by JSPS Leading Initiative for Excellent Young Researchers (LEADER). CL, RP and RD thanks CONICYT for grants Anillo

ACT-1417 and QUIMAL-160009. NK acknowledges that this work was supported by MEXT KAKENHI Grant Numbers JP17H01125, JSPS Core-to-Core Program and World Premier International Research Center Initiative (WPI), MEXT, Japan. AL, JC, JP and MM acknowledge support from the European Research Council under the European Union’s Seventh Framework Programme (FP/2007-2013) / ERC Grant Agreement No. [616170]. FM acknowledges the support of the JSPS fellowship (Grant number JP17F17025). LM thanks support from CONICYT, FONDECYT 3170846. PDM acknowledges support from the Senior Kavli Institute Fellowships at the University of Cambridge and from the Netherlands organization for scientific research (NWO) VIDI grant (dossier 639.042.730). MDN acknowledges support from NSF grants AST-1454881 and AST-1517049. FB and CR acknowledge support from the Australian Research Council through FT150100074 and the University of Melbourne. MR was supported by the ERC Consolidator Grant CMBSPEC (No. 725456). MS acknowledges support from the Jeff Bezos Fellowship at the Institute for Advanced Study. NS acknowledges support from NSF grant number 1513618. BDS acknowledges support from an Isaac Newton Trust Early Career Grant and an STFC Ernest Rutherford Fellowship. ST acknowledges the support of the JSPS fellowship (Grant number JP18J02133). In Japan, this work was supported by JSPS KAKENHI Grant Number JP17H06134. BT acknowledges the support of an STFC studentship. AvE was supported by the Beatrice and Vincent Tremaine Fellowship at CITA. Some of the results in this paper have been derived using the HEALPix (Górski et al. 2005) package. We thank members of the CMB-S4 collaboration for useful discussions and interactions that have helped inform the SO design.

REFERENCES

- Abazajian K. N. et al., *Astropart. Phys.* **63**, 66 (2015), [arXiv:1309.5383](#).
- Abazajian K. N. et al. (CMB-S4) (2016), [arXiv:1610.02743](#).
- Abbott L. F. and Sikivie P., *PLB* **120**, 133 (1983), [ADS](#).
- Addison G. E., Dunkley J., and Spergel D. N., *MNRAS* **427**, 1741 (2012), [arXiv:1204.5927](#).
- Addison G. E., Huang Y., Watts D. J., Bennett C. L., Halpern M., Hinshaw G., and Weiland J. L., *ApJ* **818**, 132 (2016), [arXiv:1511.00055](#).
- Addison G. E., Watts D. J., Bennett C. L., Halpern M., Hinshaw G., and Weiland J. L., *ApJ* **853**, 119 (2018), [arXiv:1707.06547](#).
- Adelberger E. G. et al., *Rev. Mod. Phys.* **83**, 195 (2011), [arXiv:1004.2318](#).
- Adhikari S., Sakstein J., Jain B., Dalal N., and Li B., *JCAP* **1811**, 033 (2018), [arXiv:1806.04302](#).
- Agrawal A., Fujita T., and Komatsu E., *PRD* **97**, 103526 (2018), [arXiv:1707.03023](#).
- Aich M., Hazra D. K., Sriramkumar L., and Souradeep T., *PRD* **87**, 083526 (2013), [arXiv:1106.2798](#).
- Alam S., Ata M., Bailey S., Beutler F., Bizyaev D., Blazek J. A., Bolton A. S., Brownstein J. R., Burden A., Chuang C.-H., et al., *MNRAS* **470**, 2617 (2017), [arXiv:1607.03155](#).
- Allison R., Caucal P., Calabrese E., Dunkley J., and Louis T., *PRD* **92**, 123535 (2015), [arXiv:1509.07471](#).
- Alonso D., Dunkley J., Thorne B., and Naess S., *PRD* **95**, 043504 (2017), [arXiv:1608.00551](#).
- Alvarez M. et al. (2014), [arXiv:1412.4671](#).
- Alvarez M. A., *ApJ* **824**, 118 (2016), [arXiv:1511.02846](#).
- Amendola L. and Barbieri R., *Physics Letters B* **642**, 192 (2006), [arXiv:hep-ph/0509257](#).
- Appel J. W., Xu Z., Padilla I. L., Harrington K., Pradanas Marquez B., Ali A., Bennett C. L., Brewer M. K., Bustos R., Chan M., et al., *arXiv e-prints arXiv:1811.08287* (2018), [arXiv:1811.08287](#).
- Armengaud E., Palanque-Delabrouille N., Yèche C., Marsh D. J. E., and Baur J., *MNRAS* **471**, 4606 (2017), [arXiv:1703.09126](#).
- Arvanitaki A., Dimopoulos S., Dubovsky S., Kaloper N., and March-Russell J., *PRD* **81**, 123530 (2010), [arXiv:0905.4720](#).
- Aubourg É., Bailey S., Bautista J. E., Beutler F., Bhardwaj V., Bizyaev D., Blanton M., Blomqvist M., Bolton A. S., Bovy J., et al., *Phys. Rev. D* **92**, 123516 (2015), [arXiv:1411.1074](#).
- Aver E., Olive K. A., and Skillman E. D., *JCAP* **1507**, 011 (2015), [arXiv:1503.08146](#).
- Bashinsky S. and Seljak U., *PRD* **69**, 083002 (2004), [arXiv:astro-ph/0310198](#).
- Battaglia N., Bond J. R., Pfrommer C., and Sievers J. L., *ApJ* **758**, 75 (2012), [arXiv:1109.3711](#).
- Battaglia N., Bond J. R., Pfrommer C., Sievers J. L., and Sijacki D., *ApJ* **725**, 91 (2010), [arXiv:1003.4256](#).
- Battaglia N., Ferraro S., Schaap E., and Spergel D., *JCAP* **1711**, 040 (2017), [arXiv:1705.05881](#).
- Battaglia N., Natarajan A., Trac H., Cen R., and Loeb A., *ApJ* **776**, 83 (2013), [arXiv:1211.2832](#).
- Battye R. A., Browne I. W. A., Peel M. W., Jackson N. J., and Dickinson C., *MNRAS* **413** (2010), [*Mon. Not. Roy. Astron. Soc.* **413**, 132 (2011)], [arXiv:1003.5846](#).
- Baumann D., Goon G., Lee H., and Pimentel G. L., *JHEP* **04**, 140 (2018), [arXiv:1712.06624](#).
- Baumann D., Green D., Meyers J., and Wallisch B., *JCAP* **1601**, 007 (2016a), [arXiv:1508.06342](#).
- Baumann D., Green D., and Wallisch B., *PRL* **117**, 171301 (2016b), [arXiv:1604.08614](#).
- Baxter E., Chang C., Jain B., Adhikari S., Dalal N., Kravtsov A., More S., Rozo E., Rykoff E., and Sheth R. K., *ApJ* **841**, 18 (2017), [arXiv:1702.01722](#).
- Baxter E. et al., *MNRAS* **461**, 4099 (2016), [arXiv:1602.07384](#).
- Baxter E. J. et al., *ApJ* **806**, 247 (2015), [arXiv:1412.7521](#).
- Baxter E. J. et al. (DES, SPT), *MNRAS* **476**, 2674 (2018), [arXiv:1708.01360](#).
- Bennett C. L. et al. (WMAP), *ApJS* **148**, 1 (2003), [arXiv:astro-ph/0302207](#).
- Benoit-Lévy A., Smith K. M., and Hu W., *Phys. Rev. D* **86**, 123008 (2012), [arXiv:1205.0474](#).
- Benson B. A. et al., *ApJ* **763**, 147 (2013), [arXiv:1112.5435](#).
- Berezhiani L., Famaey B., and Khoury J., *JCAP* **1809**, 021 (2018), [arXiv:1711.05748](#).
- Béthermin M. et al., *ApJ* **757**, L23 (2012), [arXiv:1208.6512](#).
- Bezrukov F. L. and Shaposhnikov M., *PLB* **659**, 703 (2008), [arXiv:0710.3755](#).
- Bhattacharya S., Nagai D., Shaw L., Crawford T., and Holder G. P., *ApJ* **760**, 5 (2012), [arXiv:1203.6368](#).
- BICEP2 and Keck Array Collaborations, *PRL* **116**, 031302 (2016), [arXiv:1510.09217](#).
- BICEP2 Collaboration, Keck Array Collaboration, Ade P. A. R., Ahmed Z., Aikin R. W., Alexander K. D., Barkats D., Benton S. J., Bischoff C. A., Bock J. J., et al., *Phys. Rev. D* **96**, 102003 (2017), [arXiv:1705.02523](#).
- BICEP2/Keck and Planck Collaborations, *PRL* **114**, 101301 (2015), [arXiv:1502.00612](#).
- Bleem L. E. et al. (SPT), *ApJS* **216**, 27 (2015), [arXiv:1409.0850](#).
- Boddy K. K. and Gluscevic V., *PRD* **98**, 083510 (2018), [arXiv:1801.08609](#).
- Bolliet B., Comis B., Komatsu E., and Macas-Prez J. F., *MNRAS* **477**, 4957 (2018), [arXiv:1712.00788](#).
- Bonavera L., González-Nuevo J., Argüeso F., and Toffolatti L., *MNRAS* **469**, 2401 (2017), [arXiv:1703.09952](#).
- Bordin L., Creminelli P., Mirbabayi M., and Noreña J., *JCAP* **1609**, 041 (2016), [arXiv:1605.08424](#).
- Borsanyi S. et al., *Nature* **539**, 69 (2016), [arXiv:1606.07494](#).
- Bridle S. L., Lewis A. M., Weller J., and Efstathiou G., *MNRAS* **342**, L72 (2003), [arXiv:astro-ph/0302306](#).
- Brust C., Kaplan D. E., and Walters M. T., *JHEP* **12**, 058 (2013), [arXiv:1303.5379](#).
- Bryan S. et al., *Proc. SPIE Int. Soc. Opt. Eng.* **10708**, 1070805 (2018a), [arXiv:1807.05215](#).
- Bryan S. et al. (BFORE), *J. Low. Temp. Phys.* **193**, 1033 (2018b), [arXiv:1707.01488](#).
- Calabrese E., Alonso D., and Dunkley J., *PRD* **95**, 063504 (2017), [arXiv:1611.10269](#).
- Calabrese E. et al., *JCAP* **1408**, 010 (2014), [arXiv:1406.4794](#).
- Capozzi F., Di Valentino E., Lisi E., Marrone A., Melchiorri A., and Palazzo A., *PRD* **95**, 096014 (2017), [arXiv:1703.04471](#).
- Cardoso J. F., Jeune M. L., Delabrouille J., Betoule M., and Patanchon G., *IEEE Journal of Selected Topics in Signal Processing* **2**, 735 (2008), ISSN 1932-4553.
- Carron J., Lewis A., and Challinor A., *JCAP* **1705**, 035 (2017), [arXiv:1701.01712](#).
- Cawthon R. et al. (DES), *MNRAS* **481**, 2427 (2018), [arXiv:1712.07298](#).
- Chacko Z., Cui Y., Hong S., and Okui T., *PRD* **92**, 055033 (2015), [arXiv:1505.04192](#).
- Challinor A. et al. (CORE), *JCAP* **1804**, 018 (2018), [arXiv:1707.02259](#).
- Chang C., Jarvis M., Jain B., Kahn S. M., Kirkby D., Connolly A., Krughoff S., Peng E., and Peterson J. R., *MNRAS* **434**, 2121 (2013), [arXiv:1305.0793](#).
- Chen X., Rachen J. P., Lopez-Caniego M., Dickinson C., Pearson T. J., Fuhrmann L., Krichbaum T. P., and Partridge B., *A&A* **553**, A107 (2013), [arXiv:1302.2114](#).
- Chen X.-l., Hannestad S., and Scherrer R. J., *PRD* **65**, 123515 (2002), [arXiv:astro-ph/0202496](#).
- Chluba J., Hill J. C., and Abitbol M. H., *MNRAS* **472**, 1195 (2017), [arXiv:1701.00274](#).
- Choi S. K. and Page L. A., *JCAP* **1512**, 020 (2015), [arXiv:1509.05934](#).
- Contaldi C. R., *International Journal of Modern Physics D* **25**, 1640014 (2016), [ADS](#).
- Cooke R. J., Pettini M., and Steidel C. C., *ApJ* **855**, 102 (2018), [arXiv:1710.11129](#).
- Crawford T. M. et al., *ApJ* **784**, 143 (2014), [arXiv:1303.3535](#).
- Creminelli P. and Zaldarriaga M., *JCAP* **0410**, 006 (2004), [arXiv:astro-ph/0407059](#).
- Crichton D. et al., *MNRAS* **458**, 1478 (2016), [arXiv:1510.05656](#).
- Cushman P. et al. (2013), [arXiv:1310.8327](#).
- Cybart R. H., Fields B. D., Olive K. A., and Yeh T.-H., *Rev. Mod. Phys.* **88**, 015004 (2016), [arXiv:1505.01076](#).
- Dalal N., Doré O., Huterer D., and Shirokov A., *PRD* **77**, 123514 (2008), [arXiv:0710.4560](#).

- Das S., Errard J., and Spergel D. (2013), [arXiv:1311.2338](#).
- Das S. and Spergel D. N., PRD **79**, 043509 (2009), [arXiv:0810.3931](#).
- Das S. et al., PRL **107**, 021301 (2011), [arXiv:1103.2124](#).
- Datta R., Aiola S., Choi S. K., Devlin M., Dunkley J., Dünner R., Gallardo P. A., Gralla M., Halpern M., Hasselfield M., et al., MNRAS (2018), [arXiv:1811.01854](#).
- De Bernardis F., Stevens J. R., Hasselfield M., Alonso D., Bond J. R., Calabrese E., Choi S. K., Crowley K. T., Devlin M., Dunkley J., et al., in *Observatory Operations: Strategies, Processes, and Systems VI* (2016), vol. 9910 of *Proc. SPIE*, p. 991014, [arXiv:1607.02120](#).
- De Bernardis F. et al., JCAP **1703**, 008 (2017), [arXiv:1607.02139](#).
- de Haan T. et al. (SPT), ApJ **832**, 95 (2016), [arXiv:1603.06522](#).
- de Putter R., Linder E. V., and Mishra A., PRD **89**, 103502 (2014), [arXiv:1401.7022](#).
- de Salas P. F., Forero D. V., Ternes C. A., Tórtola M., and Valle J. W. F., Physics Letters B **782**, 633 (2018), ADS.
- de Salas P. F. and Pastor S., JCAP **1607**, 051 (2016), [arXiv:1606.06986](#).
- Delabrouille J., Cardoso J. F., Jeune M. L., Betoule M., Fay G., and Guilloux F., A&A **493**, 835 (2009), [arXiv:0807.0773](#).
- DES Collaboration (DES), MNRAS **480**, 3879 (2018), [arXiv:1711.00403](#).
- Deutsch A.-S., Dimastrogiovanni E., Johnson M. C., Mchmeyer M., and Terrana A., PRD **98**, 123501 (2018), [arXiv:1707.08129](#).
- Dolgov A. D., Hansen S. H., and Semikoz D. V., Nucl. Phys. **B503**, 426 (1997), [arXiv:hep-ph/9703315](#).
- Dolgov A. D., Hansen S. H., and Semikoz D. V., Nucl. Phys. **B543**, 269 (1999), [arXiv:hep-ph/9805467](#).
- Domènech G., Hiramatsu T., Lin C., Sasaki M., Shiraiishi M., and Wang Y., JCAP **1705**, 034 (2017), [arXiv:1701.05554](#).
- Doré O., Hennawi J. F., and Spergel D. N., ApJ **606**, 46 (2004), [arXiv:astro-ph/0309337](#).
- Duivendoorden A., Meerburg P. D., and Freese K. (in prep.).
- Dunkley J. et al., ApJ **739**, 52 (2011), [arXiv:1009.0866](#).
- Dunkley J. et al., JCAP **1307**, 025 (2013), [arXiv:1301.0776](#).
- Dunlop J. S. (2012), [arXiv:1205.1543](#).
- Dvorkin C., Blum K., and Kamionkowski M., PRD **89**, 023519 (2014), [arXiv:1311.2937](#).
- Eifler T., Krause E., Dodelson S., Zentner A., Hearin A., and Gnedin N., MNRAS **454**, 2451 (2015), [arXiv:1405.7423](#).
- Emken T. and Kouvaris C., Phys. Rev. **D97**, 115047 (2018), [arXiv:1802.04764](#).
- Eriksen H. K., Banday A. J., Gorski K. M., and Lilje P. B., ApJ **612**, 633 (2004), [arXiv:astro-ph/0403098](#).
- Essinger-Hileman T. et al., Proc. SPIE Int. Soc. Opt. Eng. **9153**, 91531I (2014), [arXiv:1408.4788](#).
- Esteban I., Gonzalez-Garcia M. C., Maltoni M., Martinez-Soler I., and Schwetz T., JHEP **01**, 087 (2017), [arXiv:1611.01514](#).
- Fairbairn M., Marsh D. J. E., Quevillon J., and Rozier S., PRD **97**, 083502 (2018), [arXiv:1707.03310](#).
- Fan X.-H., Strauss M. A., Becker R. H., White R. L., Gunn J. E., Knapp G. R., Richards G. T., Schneider D. P., Brinkmann J., and Fukugita M., Astron. J. **132**, 117 (2006), [arXiv:astro-ph/0512082](#).
- Fang W., Hu W., and Lewis A., Phys. Rev. D **78**, 087303 (2008a), [arXiv:0808.3125](#).
- Fang W., Wang S., Hu W., Haiman Z., Hui L., and May M., Phys. Rev. D **78**, 103509 (2008b), [arXiv:0808.2208](#).
- Fantaye Y., Baccigalupi C., Leach S., and Yadav A. P. S., JCAP **1212**, 017 (2012), [arXiv:1207.0508](#).
- Fenech Conti I., Herbonnet R., Hoekstra H., Merten J., Miller L., and Viola M., MNRAS **467**, 1627 (2017), [arXiv:1606.05337](#).
- Ferraro S. and Hill J. C., PRD **97**, 023512 (2018), [arXiv:1705.06751](#).
- Ferraro S., Hill J. C., Battaglia N., Liu J., and Spergel D. N., Phys. Rev. **D94**, 123526 (2016), [arXiv:1605.02722](#).
- Ferraro S. and Smith K. M., PRD **98**, 123519 (2018), [arXiv:1803.07036](#).
- Finkbeiner D. P., Davis M., and Schlegel D. J., ApJ **524**, 867 (1999), [arXiv:astro-ph/9905128](#).
- Fischler W. and Meyers J., PRD **83**, 063520 (2011), [arXiv:1011.3501](#).
- Font-Ribera A., McDonald P., Mostek N., Reid B. A., Seo H.-J., et al., JCAP **1405**, 023 (2014), [arXiv:1308.4164](#).
- Freese K., Frieman J. A., and Olinto A. V., PRL **65**, 3233 (1990), ADS.
- Fukugita M. and Peebles P. J. E., ApJ **616**, 643 (2004), [arXiv:astro-ph/0406095](#).
- Gallazzi A., Brinchmann J., Charlot S., and White S. D. M., MNRAS **383**, 1439 (2008), [arXiv:0708.0533](#).
- Galli S., Benabed K., Bouchet F., Cardoso J.-F., Elsner F., Hivon E., Mangilli A., Prunet S., and Wandelt B., PRD **90**, 063504 (2014), [arXiv:1403.5271](#).
- Geach J. E. and Peacock J. A., Nat. Astron. **1**, 795 (2017), [arXiv:1707.09369](#).
- George E. M. et al., ApJ **799**, 177 (2015), [arXiv:1408.3161](#).
- Ghirlanda G. et al., Publ. Astron. Soc. Austral. **31**, 22 (2014), [arXiv:1402.6338](#).
- Gluscevic V. and Boddy K. K., Phys. Rev. Lett. **121**, 081301 (2018), URL <https://link.aps.org/doi/10.1103/PhysRevLett.121.081301>.
- Gorecki A., Abate A., Ansari R., Barrau A., Baumont S., Moniez M., and Ricol J.-S., A&A **561**, A128 (2014), [arXiv:1301.3010](#).
- Górski K. M., Hivon E., Banday A. J., Wandelt B. D., Hansen F. K., Reinecke M., and Bartelmann M., ApJ **622**, 759 (2005), [arXiv:astro-ph/0409513](#).
- Grain J., Tristram M., and Stompor R., PRD **79**, 123515 (2009), [arXiv:0903.2350](#).
- Gralla M., Marriage T. M., Asboth V., Battaglia N., Bock J., Bond J. R., Devlin M. J., Dünner R., Hajian A., Halpern M., et al. (in prep.).
- Gralla M. B. et al., MNRAS **445**, 460 (2014), [arXiv:1310.8281](#).
- Granot J. and Sari R., ApJ **568**, 820 (2002), [arXiv:astro-ph/0108027](#).
- Green D., Meerburg P. D., and Meyers J. (2018), [arXiv:1804.01055](#).
- Green D., Meyers J., and van Engelen A., JCAP **1712**, 005 (2017), [arXiv:1609.08143](#).
- Guo Z.-K., Schwarz D. J., and Zhang Y.-Z., JCAP **1108**, 031 (2011), [arXiv:1105.5916](#).
- Gustavino C., J. Phys. Conf. Ser. **665**, 012004 (2016).
- Hammeche S. and Lewis A., PRD **77**, 103013 (2008), [arXiv:0801.0554](#).
- Hand N. et al., PRL **109**, 041101 (2012), [arXiv:1203.4219](#).
- Hanson D. et al. (SPTpol), PRL **111**, 141301 (2013), [arXiv:1307.5830](#).
- Harikane Y. et al. (2017), [arXiv:1704.06535](#).
- Hasselfield M. et al., ApJS **209**, 17 (2013a), [arXiv:1303.4714](#).
- Hasselfield M. et al., JCAP **1307**, 008 (2013b), [arXiv:1301.0816](#).
- Hazra D. K., Shafieloo A., Smoot G. F., and Starobinsky A. A., JCAP **1609**, 009 (2016), [arXiv:1605.02106](#).
- Hazumi M. et al., Proc. SPIE Int. Soc. Opt. Eng. **8442**, 844219 (2012).
- Henderson S. W. et al., J. Low. Temp. Phys. **184**, 772 (2016), [arXiv:1510.02809](#).
- Henning J. W. et al. (SPT), ApJ **852**, 97 (2018), [arXiv:1707.09353](#).
- Herranz D., Sanz J. L., Hobson M. P., Barreiro R. B., Diego J. M., Martínez-González E., and Lasenby A. N., MNRAS **336**, 1057 (2002), [arXiv:astro-ph/0203486](#).
- Hervías-Caimapo C., Bonaldi A., and Brown M. L., MNRAS **462**, 2063 (2016), [arXiv:1602.01313](#).
- Hezaveh Y. D. et al., ApJ **823**, 37 (2016), [arXiv:1601.01388](#).
- Hill C. A., Bruno S. M. M., Simon S. M., Ali A., Arnold K. S., Ashton P. C., Barron D., Bryan S., Chinone Y., Coppi G., et al. (2018), vol. 10708 of *Society of Photo-Optical Instrumentation Engineers (SPIE) Conference Series*, p. 1070842, [arXiv:1806.04316](#).
- Hill J. C., PRD **98**, 083542 (2018), [arXiv:1807.07324](#).
- Hill J. C. (in prep.).
- Hill J. C., Ferraro S., Battaglia N., Liu J., and Spergel D. N., PRL **117**, 051301 (2016), [arXiv:1603.01608](#).
- Hill J. C. and Pajer E., Phys. Rev. **D88**, 063526 (2013), [arXiv:1303.4726](#).
- Hill J. C. and Sherwin B. D., PRD **87**, 023527 (2013), [arXiv:1205.5794](#).
- Hill J. C. and Spergel D. N., JCAP **1402**, 030 (2014), [arXiv:1312.4525](#).
- Hill J. C. et al. (ACT) (2014), [arXiv:1411.8004](#).
- Hilton M. et al. (ACT), ApJS **235**, 20 (2018), [arXiv:1709.05600](#).

- Hložek R., Grin D., Marsh D. J. E., and Ferreira P. G., PRD **91**, 103512 (2015), [arXiv:1410.2896](#).
- Hložek R. et al., ApJ **749**, 90 (2012), [arXiv:1105.4887](#).
- Holder G. P. and Kosowsky A., ApJ **616**, 8 (2004), [arXiv:astro-ph/0401519](#).
- Horowitz B. and Seljak U., MNRAS **469**, 394 (2017), [arXiv:1609.01850](#).
- Hou Z., Keisler R., Knox L., Millea M., and Reichardt C., PRD **87**, 083008 (2013), [arXiv:1104.2333](#).
- Hu W., Phys. Rev. D **77**, 103524 (2008), [arXiv:0801.2433](#).
- Hu W., DeDeo S., and Vale C., New J. Phys. **9**, 441 (2007a), [arXiv:astro-ph/0701276](#).
- Hu W., Holz D. E., and Vale C., PRD **76**, 127301 (2007b), [arXiv:0708.4391](#).
- Hu W. and Okamoto T., ApJ **574**, 566 (2002), [arXiv:astro-ph/0111606](#).
- Hu W. and Sawicki I., Phys. Rev. D **76**, 104043 (2007), [arXiv:0708.1190](#).
- Huffenberger K. M. et al. (QUIET), ApJ **806**, 112 (2015), [arXiv:1412.1111](#).
- Hui H. et al. (BICEP3), Proc. SPIE Int. Soc. Opt. Eng. **9914**, 99140T (2016), [arXiv:1607.06861](#).
- Hui L., Ostriker J. P., Tremaine S., and Witten E., Phys. Rev. D **95**, 043541 (2017), [arXiv:1610.08297](#).
- Hunt P. and Sarkar S., JCAP **1401**, 025 (2014), [arXiv:1308.2317](#).
- Hurier G. and Lacasa F., A&A **604**, A71 (2017), [arXiv:1701.09067](#).
- Huterer D., Takada M., Bernstein G., and Jain B., MNRAS **366**, 101 (2006), [arXiv:astro-ph/0506030](#).
- Hwang J.-c. and Noh H., PLB **680**, 1 (2009), [arXiv:0902.4738](#).
- Ijjas A. and Steinhardt P. J., Classical and Quantum Gravity **35**, 135004 (2018), [arXiv:1803.01961](#).
- Ipsier J. and Sikivie P., PRL **50**, 925 (1983), [ADS](#).
- Jain B. and Taylor A., PRL **91**, 141302 (2003), [arXiv:astro-ph/0306046](#).
- Jones M. E. et al. (C-BASS), MNRAS **480**, 3224 (2018), [arXiv:1805.04490](#).
- Kamionkowski M., Kosowsky A., and Stebbins A., Phys. Rev. Lett. **78**, 2058 (1997), [arXiv:astro-ph/9609132](#).
- KATRIN Collaboration (2005), URL <https://www.katrin.kit.edu/publikationen/DesignReport2004-12Jan2005.pdf>.
- Khatri R., A&A **592**, A48 (2016), [arXiv:1505.00778](#).
- Kim J. E. and Carosi G., Rev. Mod. Phys. **82**, 557 (2010), [arXiv:0807.3125](#).
- Knox L., Phys. Rev. **D52**, 4307 (1995), [arXiv:astro-ph/9504054](#).
- Knox L. and Song Y.-S., PRL **89**, 011303 (2002), [arXiv:astro-ph/0202286](#).
- Kolb E. W. and Turner M. S., Front.Phys. **69**, 1 (1990).
- Komatsu E. and Seljak U., MNRAS **336**, 1256 (2002), [arXiv:astro-ph/0205468](#).
- Komatsu E. et al. (2009), [arXiv:0902.4759](#).
- Krachmalnicoff N., Baccigalupi C., Aumont J., Bersanelli M., and Mennella A., A&A **588**, A65 (2016), [arXiv:1511.00532](#).
- Krachmalnicoff N. et al., A&A **618**, A166 (2018), [arXiv:1802.01145](#).
- Kusaka A. et al., JCAP **1809**, 005 (2018), [arXiv:1801.01218](#).
- Larsen P., Challinor A., Sherwin B. D., and Mak D., PRL **117**, 151102 (2016), [arXiv:1607.05733](#).
- Lee H., Baumann D., and Pimentel G. L., JHEP **12**, 040 (2016), [arXiv:1607.03735](#).
- Lemos P., Lee E., Efstathiou G., and Gratton S. (2018), [arXiv:1806.06781](#).
- Lesgourgues J., Mangano G., Miele G., and Pastor S., *Neutrino Cosmology* (Cambridge University Press, 2013).
- Levi M. et al. (DESI) (2013), [arXiv:1308.0847](#).
- Levy A. M., Ijjas A., and Steinhardt P. J., PRD **92**, 063524 (2015), [arXiv:1506.01011](#).
- Lewis A., Phys. Rev. D **68**, 083509 (2003), [arXiv:astro-ph/0305545](#).
- Linde A. D., PLB **129**, 177 (1983), [ADS](#).
- Liu A., Pritchard J. R., Allison R., Parsons A. R., Seljak U., and Sherwin B. D., PRD **93**, 043013 (2016a), [arXiv:1509.08463](#).
- Liu J., Ortiz-Vazquez A., and Hill J. C., PRD **93**, 103508 (2016b), [arXiv:1601.05720](#).
- Lochner M., Scolnic D. M., Awan H., Regnault N., Gris P., Mandelbaum R., Gawiser E., Almoubayyed H., Setzer C. N., Huber S., et al., arXiv e-prints arXiv:1812.00515 (2018), [arXiv:1812.00515](#).
- Louis T. and Alonso D., PRD **95**, 043517 (2017), [arXiv:1609.03997](#).
- Louis T., Bunn E. F., Wandelt B., and Silk J., Phys. Rev. D **96**, 123509 (2017), [arXiv:1707.04102](#).
- Louis T. et al. (ACTPol), JCAP **1706**, 031 (2017), [arXiv:1610.02360](#).
- LSST Science Collaboration (2009), [arXiv:0912.0201](#).
- Macpherson D. and Coward D., MNRAS **453**, 2144 (2015), [arXiv:1506.03891](#).
- Madhavacheril M. et al. (ACT), PRL **114**, 151302 (2015), [Addendum: PRL 114,no.18,189901(2015)], [arXiv:1411.7999](#).
- Madhavacheril M. S., Battaglia N., and Miyatake H., PRD **96**, 103525 (2017), [arXiv:1708.07502](#).
- Madhavacheril M. S. and Hill J. C., PRD **98**, 023534 (2018), [arXiv:1802.08230](#).
- Madhavacheril M. S., Sehgal N., and Slatyer T. R., PRD **89**, 103508 (2014), [arXiv:1310.3815](#).
- Mak D. S. Y., Challinor A., Efstathiou G., Lagache G., and Lagache G., MNRAS **466**, 286 (2017), [arXiv:1609.08942](#).
- Maldacena J. M., JHEP **05**, 013 (2003), [arXiv:astro-ph/0210603](#).
- Maldacena J. M. and Pimentel G. L., JHEP **09**, 045 (2011), [arXiv:1104.2846](#).
- Mandelbaum R. et al. (2017), [arXiv:1705.06745](#).
- Mangano G., Miele G., Pastor S., and Peloso M., PLB **534**, 8 (2002), [arXiv:astro-ph/0111408](#).
- Mantz A. B., Allen S. W., Morris R. G., Rapetti D. A., Applegate D. E., Kelly P. L., von der Linden A., and Schmidt R. W., MNRAS **440**, 2077 (2014), [arXiv:1402.6212](#).
- Mantz A. B. et al., MNRAS **446**, 2205 (2015), [arXiv:1407.4516](#).
- Manzotti A. et al. (Herschel, SPT), ApJ **846**, 45 (2017), [arXiv:1701.04396](#).
- Marrone D. P., Spilker J. S., Hayward C. C., Vieira J. D., Aravena M., Ashby M. L. N., Bayliss M. B., Béthermin M., Brodwin M., Bothwell M. S., et al., Nature **553**, 51 (2018), [arXiv:1712.03020](#).
- Marsden D. W. et al., MNRAS **439**, 1556 (2014), [arXiv:1306.2288](#).
- Marsh D. J. E., Phys. Rept. **643**, 1 (2016), [arXiv:1510.07633](#).
- Marsh D. J. E. and Ferreira P. G., PRD **82**, 103528 (2010), [arXiv:1009.3501](#).
- Martin J., Ringeval C., Trotta R., and Vennin V., JCAP **1403**, 039 (2014a), [arXiv:1312.3529](#).
- Martin J., Ringeval C., and Vennin V., Phys. Dark Univ. **5-6**, 75 (2014b), [arXiv:1303.3787](#).
- Matsumura T. et al. (2013), [J. Low. Temp. Phys.176,733(2014)], [arXiv:1311.2847](#).
- McAllister L., Silverstein E., and Westphal A., PRD. **82**, 046003 (2010), [arXiv:0808.0706](#).
- Meerburg P. D., Meyers J., Smith K. M., and van Engelen A., PRD **95**, 123538 (2017), [arXiv:1701.06992](#).
- Meerburg P. D., Meyers J., van Engelen A., and Ali-Haïmoud Y., PRD **93**, 123511 (2016), [arXiv:1603.02243](#).
- Melin J.-B., Bartlett J. G., and Delabrouille J., A&A **459**, 341 (2006), [arXiv:astro-ph/0602424](#).
- Menanteau F. et al., ApJ **748**, 7 (2012), [arXiv:1109.0953](#).
- Mesinger A., McQuinn M., and Spergel D. N., MNRAS **422**, 1403 (2012), [arXiv:1112.1820](#).
- Meyers J., Meerburg P. D., van Engelen A., and Battaglia N., PRD **97**, 103505 (2018), [arXiv:1710.01708](#).
- Millea M., Knox L., and Fields B., PRD **92**, 023010 (2015), [arXiv:1501.04097](#).
- Miranda V., Hu W., He C., and Motohashi H., PRD **93**, 023504 (2016), [arXiv:1510.07580](#).
- Miyatake H., Madhavacheril M. S., Sehgal N., Slosar A., Spergel D. N., Sherwin B., and van Engelen A., PRL **118**, 161301 (2017), [arXiv:1605.05337](#).
- Mocanu L. M. et al., ApJ **779**, 61 (2013), [arXiv:1306.3470](#).
- Monsalve R. A., Rogers A. E. E., Bowman J. D., and Mozden T. J., ApJ **847**, 64 (2017), [arXiv:1708.05817](#).
- Moody J. and Wilczek F., PRD **30**, 130 (1984).
- More S. et al., ApJ **825**, 39 (2016), [arXiv:1601.06063](#).
- Mueller E.-M., de Bernardis F., Bean R., and Niemack M. D., ApJ **808**, 47 (2015), [arXiv:1408.6248](#).

- Münchmeyer M., Madhavacheril M. S., Ferraro S., Johnson M. C., and Smith K. M., arXiv e-prints arXiv:1810.13424 (2018), [arXiv:1810.13424](#).
- Murphy T., Sadler E. M., Ekers R. D., Massardi M., Hancock P. J., Mahony E., Ricci R., Burke-Spolaor S., Calabretta M., Chhetri R., et al., MNRAS **402**, 2403 (2010), [arXiv:0911.0002](#).
- Namba R., Peloso M., Shiraishi M., Sorbo L., and Unal C., JCAP **1601**, 041 (2016), [arXiv:1509.07521](#).
- Namikawa T., Hanson D., and Takahashi R., MNRAS **431**, 609 (2013), [arXiv:1209.0091](#).
- Niemack M. D., Appl. Opt. **55**, 1688 (2016), [arXiv:1511.04506](#).
- Noh H., Park C.-G., and Hwang J.-c., PLB **726**, 559 (2013), [arXiv:1309.5692](#).
- Obied G., Dvorkin C., Heinrich C., Hu W., and Miranda V., PRD **96**, 083526 (2017), [arXiv:1706.09412](#).
- Oguri M. and Hamana T., MNRAS **414**, 1851 (2011), [arXiv:1101.0650](#).
- Olsen K., Di Criscienzo M., Jones R. L., Schwamb M. E., "Edward" Lin H. W., Awan H., Marshall P., Gawiser E., Bolton A., and Eisenstein D., arXiv e-prints arXiv:1812.02204 (2018), [arXiv:1812.02204](#).
- Ono Y. et al., Publ. Astron. Soc. Jap. **70**, S10 (2018), [arXiv:1704.06004](#).
- Osborne S. J., Hanson D., and Doré O., JCAP **1403**, 024 (2014), [arXiv:1310.7547](#).
- Ostriker J. P., Bode P., and Babul A., ApJ **634**, 964 (2005), [arXiv:astro-ph/0504334](#).
- Padmanabhan N. and Finkbeiner D. P., PRD **72**, 023508 (2005), [arXiv:astro-ph/0503486](#).
- Paine S., Zenodo:1193646 (2018).
- Pardo J. R., Cernicharo J., and Serabyn E., IEEE Transactions on Antennas and Propagation **49**, 1683 (2001), ISSN 0018-926X.
- Park H., Alvarez M. A., and Bond J. R., ApJ **853**, 121 (2018), [arXiv:1710.02792](#).
- Parshley S. C., Niemack M. D., Hills R., Dicker S. R., Dünner R., Erler J., Gallardo P. A., Gudmundsson J. E., Herter T., Koopman B. J., et al., ArXiv e-prints (2018), [arXiv:1807.06678](#).
- Partridge B., Bonavera L., López-Cañiego M., Datta R., Gonzalez-Nuevo J., Gralla M., Herranz D., Lähteenmäki A., Mocuán L., Prince H., et al., Galaxies **5**, 47 (2017), ADS.
- Patrignani C. et al. (Particle Data Group), Chin. Phys. **C40**, 100001 (2016).
- Peccei R. and Quinn H. R., PRL **38**, 1440 (1977).
- Peloton J., Schmittfull M., Lewis A., Carron J., and Zahn O., PRD **95**, 043508 (2017), [arXiv:1611.01446](#).
- Pisanti O., Cirillo A., Esposito S., Iocco F., Mangano G., Miele G., and Serpico P. D., Comput. Phys. Commun. **178**, 956 (2008), [arXiv:0705.0290](#).
- Pitrou C., Coc A., Uzan J.-P., and Vangioni E., Phys. Rept. **04**, 005 (2018), [arXiv:1801.08023](#).
- Planck Collaboration , A&A **571**, A15 (2014a), [arXiv:1303.5075](#).
- Planck Collaboration , A&A **571**, A16 (2014b), [arXiv:1303.5076](#).
- Planck Collaboration , A&A **571**, A20 (2014c), [arXiv:1303.5080](#).
- Planck Collaboration , A&A **571**, A21 (2014d), [arXiv:1303.5081](#).
- Planck Collaboration , A&A **571**, A30 (2014e), [arXiv:1309.0382](#).
- Planck Collaboration , A&A **594**, A6 (2016a), [arXiv:1502.01585](#).
- Planck Collaboration , A&A **594**, A8 (2016b), [arXiv:1502.01587](#).
- Planck Collaboration , A&A **594**, A10 (2016c), [arXiv:1502.01588](#).
- Planck Collaboration , A&A **594**, A11 (2016d), [arXiv:1507.02704](#).
- Planck Collaboration , A&A **594**, A13 (2016e), [arXiv:1502.01589](#).
- Planck Collaboration , A&A **594**, A17 (2016f), [arXiv:1502.01592](#).
- Planck Collaboration , A&A **594**, A20 (2016g), [arXiv:1502.02114](#).
- Planck Collaboration , A&A **594**, A22 (2016h), [arXiv:1502.01596](#).
- Planck Collaboration , A&A **594**, A23 (2016i), [arXiv:1509.06555](#).
- Planck Collaboration , A&A **594**, A24 (2016j), [arXiv:1502.01597](#).
- Planck Collaboration , A&A **594**, A25 (2016k), [arXiv:1506.06660](#).
- Planck Collaboration , A&A **594**, A26 (2016l), [arXiv:1507.02058](#).
- Planck Collaboration , A&A **594**, A27 (2016m), [arXiv:1502.01598](#).
- Planck Collaboration , A&A **596**, A110 (2016n), [arXiv:1605.08633](#).
- Planck Collaboration , A&A **596**, A107 (2016o), [arXiv:1605.02985](#).
- Planck Collaboration , A&A **596**, A108 (2016p), [arXiv:1605.03507](#).
- Planck Collaboration , A&A **586**, A133 (2016q), [arXiv:1409.5738](#).
- Planck Collaboration , A&A **607**, A95 (2017), [arXiv:1608.02487](#).
- Planck Collaboration (2018a), [arXiv:1807.06205](#).
- Planck Collaboration (2018b), [arXiv:1807.06206](#).
- Planck Collaboration (2018c), [arXiv:1807.06207](#).
- Planck Collaboration (2018d), [arXiv:1807.06209](#).
- Planck Collaboration (2018e), [arXiv:1807.06210](#).
- Planck Collaboration (2018f), [arXiv:1807.06211](#).
- Poidevin F. et al. (QUIJOTE) (2018), [arXiv:1802.04594](#).
- POLARBEAR Collaboration , ApJ **794**, 171 (2014a), [arXiv:1403.2369](#).
- POLARBEAR Collaboration , PRL **112**, 131302 (2014b), [arXiv:1312.6645](#).
- POLARBEAR Collaboration , PRL **113**, 021301 (2014c), [arXiv:1312.6646](#).
- POLARBEAR Collaboration , PRD **92**, 123509 (2015), [arXiv:1509.02461](#).
- POLARBEAR Collaboration , ApJ **848**, 121 (2017), [arXiv:1705.02907](#).
- Posada C. M., Ade P. A. R., Anderson A. J., Avva J., Ahmed Z., Arnold K. S., Ausermann J., Bender A. N., Benson B. A., Bleem L., et al., **9914**, 991417 (2016), ADS.
- Poulin V., Smith T. L., Grin D., Karwal T., and Kamionkowski M., PRD **98**, 083525 (2018), [arXiv:1806.10608](#).
- Puglisi G., Galluzzi V., Bonavera L., Gonzalez-Nuevo J., Lapi A., Massardi M., Perrotta F., Baccigalupi C., Celotti A., and Danese L. (2017), [arXiv:1712.09639](#).
- QUIET Collaboration , ApJ **741**, 111 (2011), [arXiv:1012.3191](#).
- QUIET Collaboration , ApJ **760**, 145 (2012), [arXiv:1207.5034](#).
- Reichardt C. L. et al., ApJ **755**, 70 (2012), [arXiv:1111.0932](#).
- Remazeilles M., Delabrouille J., and Cardoso J.-F., MNRAS **410**, 2481 (2011), [arXiv:1006.5599](#).
- Richards J. L., Hovatta T., Max-Moerbeck W., Pavlidou V., Pearson T. J., and Readhead A. C. S., MNRAS **438**, 3058 (2014), [arXiv:1312.3634](#).
- Riess A. G. et al., ApJ **861**, 126 (2018), [arXiv:1804.10655](#).
- Rozo E. et al. (DES), MNRAS **461**, 1431 (2016), [arXiv:1507.05460](#).
- Rubiño-Martín J. A. and Sunyaev R. A., MNRAS **344**, 1155 (2003), [arXiv:astro-ph/0211430](#).
- Rykoff E. et al. (SDSS), Astrophys.J. **785**, 104 (2014), [arXiv:1303.3562](#).
- Salvati L., Douspis M., and Aghanim N., A&A **614**, A13 (2018), [arXiv:1708.00697](#).
- Sazonov S. Y. and Sunyaev R. A., MNRAS **310**, 765 (1999), [arXiv:astro-ph/9903287](#).
- Schaan E. and Ferraro S. (2018), [arXiv:1804.06403](#).
- Schaan E., Krause E., Eifler T., Doré O., Miyatake H., Rhodes J., and Spergel D. N., PRD **95**, 123512 (2017), [arXiv:1607.01761](#).
- Schaan E. et al. (ACTPol), PRD **93**, 082002 (2016), [arXiv:1510.06442](#).
- Schive H.-Y., Chiueh T., Broadhurst T., and Huang K.-W., ApJ **818**, 89 (2016), [arXiv:1508.04621](#).
- Schmittfull M. and Seljak U., PRD **97**, 123540 (2018), [arXiv:1710.09465](#).
- Sehgal N., Bode P., Das S., Hernandez-Monteagudo C., Huffenberger K., Lin Y.-T., Ostriker J. P., and Trac H., ApJ **709**, 920 (2010), [arXiv:0908.0540](#).
- Sehgal N. et al., ApJ **732**, 44 (2011), [arXiv:1010.1025](#).
- Sekimoto Y. et al., Proc. SPIE Int. Soc. Opt. Eng. **10698**, 106981Y (2018).
- Seljak U., PRL **102**, 021302 (2009), [arXiv:0807.1770](#).
- Seljak U. and Hirata C. M., PRD **69**, 043005 (2004), [arXiv:astro-ph/0310163](#).
- Seljak U. and Zaldarriaga M., ApJ **538**, 57 (2000), [arXiv:astro-ph/9907254](#).
- Semboloni E., Hoekstra H., Schaye J., van Daalen M. P., and McCarthy I. J., MNRAS **417**, 2020 (2011), [arXiv:1105.1075](#).
- Shaw L. D., Rudd D. H., and Nagai D., ApJ **756**, 15 (2012), [arXiv:1109.0553](#).
- Shaw L. D., Zahn O., Holder G. P., and Doré O., ApJ **702**, 368 (2009), [arXiv:0903.5322](#).
- Sheldon E. S. and Huff E. M., ApJ **841**, 24 (2017), [arXiv:1702.02601](#).
- Sherwin B. D. and Schmittfull M., PRD **92**, 043005 (2015), [arXiv:1502.05356](#).
- Sherwin B. D. et al., PRD **95**, 123529 (2017), [arXiv:1611.09753](#).
- Shimon M., Sadeh S., and Rephaeli Y., MNRAS **412**, 1895 (2011), [arXiv:1009.4110](#).

- Shiraishi M., Liguori M., and Fergusson J. R., JCAP **1801**, 016 (2018), [arXiv:1710.06778](#).
- Shiraishi M., Nitta D., Yokoyama S., Ichiki K., and Takahashi K., Prog. Theor. Phys. **125**, 795 (2011), [arXiv:1012.1079](#).
- Sievers J. L. et al. (ACT), JCAP **1310**, 060 (2013), [arXiv:1301.0824](#).
- Sigurdson K., Doran M., Kurylov A., Caldwell R. R., and Kamionkowski M., Phys. Rev. **D70**, 083501 (2004), [Erratum: Phys. Rev. **D73**, 089903 (2006)], [arXiv:astro-ph/0406355](#).
- Simons Observatory Collaboration (in prep.).
- Singh S., Mandelbaum R., and Brownstein J. R., MNRAS **464**, 2120 (2017), [arXiv:1606.08841](#).
- Slatyer T. R. and Wu C.-L., PRD **98**, 023013 (2018), [arXiv:1803.09734](#).
- Smith K. M., PRD **74**, 083002 (2006), [arXiv:astro-ph/0511629](#).
- Smith K. M. and Ferraro S., PRL **119**, 021301 (2017), [arXiv:1607.01769](#).
- Smith K. M., Hanson D., LoVerde M., Hirata C. M., and Zahn O., JCAP **1206**, 014 (2012), [arXiv:1010.0048](#).
- Smith K. M., Madhavacheril M. S., Münchmeyer M., Ferraro S., Giri U., and Johnson M. C., arXiv e-prints arXiv:1810.13423 (2018), [arXiv:1810.13423](#).
- Starobinskij A. A., Soviet Journal of Experimental and Theoretical Physics Letters **55**, 489 (1992), [ADS](#).
- Starobinskij A. A., Soviet Journal of Experimental and Theoretical Physics Letters **30**, 682 (1979), [ADS](#).
- Starobinsky A. A., PLB **91**, 99 (1980), [ADS](#).
- Stevens J. R. et al., Proc. SPIE Int. Soc. Opt. Eng. **10708**, 1070841 (2018), [arXiv:1808.05131](#).
- Stompór R., Errard J., and Poletti D., PRD **94**, 083526 (2016), [arXiv:1609.03807](#).
- Story K. T. et al. (SPT), ApJ **810**, 50 (2015), [arXiv:1412.4760](#).
- Sunyaev R. A. and Zel'dovich Y. B., Nature **223**, 721 (1969), [ADS](#).
- Sunyaev R. A. and Zel'dovich Y. B., Comments on Astrophysics and Space Physics **4**, 173 (1972), [ADS](#).
- Suzuki A. et al. (POLARBEAR), J. Low. Temp. Phys. **184**, 805 (2016), [arXiv:1512.07299](#).
- Takakura S. et al., JCAP **1705**, 008 (2017), [arXiv:1702.07111](#).
- Tegmark M. and de Oliveira-Costa A., Phys. Rev. D **64**, 063001 (2001), [arXiv:astro-ph/0012120](#).
- Thorne B., Dunkley J., Alonso D., and Naess S., MNRAS **469**, 2821 (2017), [arXiv:1608.02841](#).
- Toma K., Sakamoto T., and Mészáros P., ApJ **731**, 127 (2011), [arXiv:1008.1269](#).
- Trac H., Bode P., and Ostriker J. P., ApJ **727**, 94 (2011), [arXiv:1006.2828](#).
- Tucci M., Martínez-González E., Toffolatti L., Gonzalez-Nuevo J., and De Zotti G., MNRAS **349**, 1267 (2004), [arXiv:astro-ph/0307073](#).
- Tucci M. and Toffolatti L., Adv. Astron. **2012**, 624987 (2012), [arXiv:1204.0427](#).
- Tucci M., Toffolatti L., De Zotti G., and Martínez-González E., A&A **533**, A57 (2011), [arXiv:1103.5707](#).
- Vallinotto A., ApJ **759**, 32 (2012), [arXiv:1110.5339](#).
- Vallinotto A., ApJ **778**, 108 (2013), [arXiv:1304.3474](#).
- van Engelen A., Bhattacharya S., Sehgal N., Holder G. P., Zahn O., and Nagai D., ApJ **786**, 13 (2014), [arXiv:1310.7023](#).
- van Engelen A. et al., ApJ **756**, 142 (2012), [arXiv:1202.0546](#).
- Vanderlinde K. et al., ApJ **722**, 1180 (2010), [arXiv:1003.0003](#).
- Vieira J. D., Crawford T. M., Switzer E. R., Ade P. A. R., Aird K. A., Ashby M. L. N., Benson B. A., Bleem L. E., Brodwin M., Carlstrom J. E., et al., ApJ **719**, 763 (2010), [arXiv:0912.2338](#).
- Vikhlinin A. et al., ApJ **692**, 1060 (2009), [arXiv:0812.2720](#).
- Ward J. T., Alonso D., Errard J., Devlin M. J., and Hasselfield M., ApJ **861**, 82 (2018), [arXiv:1803.07630](#).
- Watts D. J. et al., ApJ **863**, 121 (2018), [arXiv:1801.01481](#).
- Weinberg S., PRL **40**, 223 (1978), [ADS](#).
- Whitehorn N. et al. (SPT), ApJ **830**, 143 (2016), [arXiv:1604.03507](#).
- Wilczek F., PRL **40**, 279 (1978).
- Wilson M. J. et al., PRD **86**, 122005 (2012), [arXiv:1203.6633](#).
- Xu W. L., Dvorkin C., and Chael A., PRD **97**, 103530 (2018), [arXiv:1802.06788](#).
- Yu B., Hill J. C., and Sherwin B. D., PRD **96**, 123511 (2017), [arXiv:1705.02332](#).
- Zaldarriaga M. and Seljak U., Phys. Rev. D **55**, 1830 (1997), [arXiv:astro-ph/9609170](#).
- Zuntz J. et al. (DES), Submitted to: Mon. Not. Roy. Astron. Soc. (2017), [arXiv:1708.01533](#).